ABSTRACT

Title of dissertation: LEGGED LOCOMOTION IN SUB-GRAM ROBOTS

Ryan St. Pierre
Doctor of Philosophy

Dissertation directed by: Professor Sarah Bergbreiter
Department of Mechanical Engineering

This dissertation presents work towards understanding the role of legs in locomotion for robots with a body mass of 1 g to 1 mg. Locomotion models such as the inverted pendulum model and the spring loaded inverted pendulum model provide insight into the design parameters and control of legged robots. However, as body mass scales down, below 1 g, the inertial forces required in these models to either propel the next steps or compress a spring begin to vanish, requiring an understanding of how legged locomotion differs between scales. To this end, an experimental methodology is presented using physical models focusing solely on the mechanical aspects of locomotion at this scale to understand and develop relevant locomotion models.

At the gram-scale, a new experimental methodology is developed utilizing 3D printed robots and permanent magnets for actuators. This technique enables studies on the role of gait and the viscoelastic properties of the robot's legs. By choosing a well tuned leg, with favorable compliance and damping, and a leg-dominated gait,

gram-scale legged running robots were demonstrated running at speeds up to 11.7 body lengths per second. The leg compliance and damping design space is explored in a torque-driven spring loaded inverted pendulum model to better understand the trade-offs between robot speed, stability, and efficiency.

The physical platform is scalable with the availability of magnetic material and printing. In this work, robots are scaled down to 1 mg in body mass, allowing locomotion to be studied at body masses 1,000 times smaller than before. This work demonstrates a robot running at speeds up to 15 body lengths per second and further modifications demonstrated speeds over 35 body lengths per second. Using this platform, the mechanics and ground reaction forces of a milligram-scale runner were measured, showing a locomotion profile similar to a grounded torque-driven spring loaded inverted pendulum model. Using observations from the experimental work, this model was numerically simulated, giving insight into how leg compliance is used for a grounded running model. For example, the simulation shows that leg compression increases speed, but does not necessarily propel the next steps as with a traditional spring loaded inverted pendulum model. Bringing together the experimental insights with the numerical model provides a road map for exploiting passive dynamics in robots at sub-gram scales.

LEGGED LOCOMOTION IN SUB-GRAM ROBOTS

by

Ryan St. Pierre

Dissertation submitted to the Faculty of the Graduate School of the
University of Maryland, College Park in partial fulfillment
of the requirements for the degree of
Doctor of Philosophy
2018

Advisory Committee:
Professor Sarah Bergbreiter, Advisor
Professor Jin-Oh Hahn
Professor Elisabeth Smela
Professor Ryan Sochol
Professor Jeffrey Shultz

© Copyright by
Ryan St. Pierre
2018

Acknowledgments

There are several people to thank for their support during the completion of this work. First and foremost, I would like to thank my advisor, Professor Sarah Bergbreiter. Her guidance, support, and mentorship throughout the years made this work possible. It has been an honor to work with her.

I would also like to thank Wei Gao and Professor Jonathan Clark from Florida State University. Their simulation environment for the torque-driven spring loaded inverted pendulum model and discussions on legged locomotion furthered the ideas presented in this work. The complementary simulation work furthered and clarified insights on legged locomotion.

I would like to thank my labmates at the Micro Robotics Lab, both past and present for all their helpful feedback, discussion of ideas, collaborations, and general conversation. In particular, I would like to thank Dr. Babak Eslami for his help with AFM and Dr. Dana Vogtmann whose own work on and discussion of legged microrobots was of great help to me.

I would also like to thank my committee members for their expertise and input on this work, including Professor Jin-Oh Hahn, Professor Ryan Sochol, and Professor Jeffrey Shultz. In particular, I would like to thank Professor Elisabeth Smela not only for her input on this work but also for the use of her lab space and equipment used in measuring the viscoelastic properties of polymer legs.

Finally, I would like to thank my friends and family for their support. In particular, my sister and her family who I could not imagine being without.

Table of Contents

List of Tables v

List of Figures vi

1 Introduction 1
- 1.1 Insect locomotion . . . 2
- 1.2 Legged locomotion modeling . . . 3
- 1.3 Insect-inspired robots . . . 5
- 1.4 Outline of Dissertation . . . 10

2 Magnetic actuation for studying legged locomotion 12
- 2.1 Magnetic actuation . . . 13
  - 2.1.1 Frequency of operation . . . 15
- 2.2 Robot design . . . 17
  - 2.2.1 Fabrication . . . 19
  - 2.2.2 Gait Configuration . . . 19
    - 2.2.2.1 Bounding subset . . . 20
- 2.3 Experimental setup . . . 22
- 2.4 Results . . . 26
  - 2.4.1 Gait Characteristics . . . 26
  - 2.4.2 Bounding subset . . . 28
  - 2.4.3 Frequency Testing . . . 30
  - 2.4.4 Rough Terrain . . . 32
- 2.5 Conclusions . . . 34

3 Compliance and damping in legged, small-scale robots 39
- 3.1 Leg properties . . . 41
  - 3.1.1 Experimental setup . . . 41
- 3.2 Results . . . 42
  - 3.2.1 Mechanical impedance and phase shift . . . 42
  - 3.2.2 Spring and damping constants . . . 46
- 3.3 Robot fabrication . . . 50
- 3.4 Experimental setup . . . 50
- 3.5 Experimental results . . . 52
  - 3.5.1 Velocity . . . 52
  - 3.5.2 Energy phasing . . . 56
  - 3.5.3 Dynamic repeatability . . . 60
    - 3.5.3.1 Metrics . . . 60
    - 3.5.3.2 Experimental results . . . 61
- 3.6 Simulation insights . . . 65
  - 3.6.1 Overview of simulation . . . 65
  - 3.6.2 Simulation results . . . 68
- 3.7 Discussion . . . 75

3.8 Conclusions . . . 80

4 μQuad: a 2.5 mm, 1 mg legged microrobot 82
4.1 Fabrication . . . 85
4.2 Experimental setup . . . 87
4.3 Characterization of 3D printed rotational bearings . . . 88
4.3.1 Startup torque . . . 90
4.3.2 Actuation response . . . 91
4.3.3 Wear . . . 93
4.4 Locomotion results . . . 93
4.4.1 Velocity . . . 93
4.4.2 Energy phasing . . . 97
4.5 Conclusions . . . 99

5 Mechanics of milligram-scale running 103
5.1 Robot design and modifications . . . 105
5.2 Ground reaction force sensing . . . 106
5.2.1 Design and fabrication . . . 107
5.2.2 Calibration . . . 111
5.3 Experimental setup . . . 112
5.4 Locomotion results . . . 114
5.4.1 Velocity . . . 114
5.4.2 Motion and energetics of the center of mass . . . 114
5.4.3 Congruity and recovery . . . 120
5.4.4 Ground reaction force . . . 126
5.5 Torque-driven grounded SLIP model . . . 129
5.5.1 Simulation motion and energetics of the center of mass . . . 129
5.5.2 Simulation ground reaction force . . . 132
5.5.3 Model-based insights . . . 134
5.6 Conclusions . . . 141

6 Conclusions 143
6.1 Future work . . . 144

A MATLAB code to generate rough terrain 146
A.1 Rough terrain generation . . . 146

B MATLAB code for torque-driven grounded running 151
B.1 Forward Euler simulation for the torque-driven grounded SLIP model 151

Bibliography 156

List of Tables

2.1 Percent of rough terrain traversed by quadruped using the different gaits. 2X and 3X refer to the upper bound of the normal distribution used to make the terrain. 34

List of Figures

1.1 Speed vs. body mass of select legged robots [29, 23, 27, 44, 38, 45, 46, 24] and insects [47, 48, 49, 50, 51, 52, 14]. The shaded right half of the plot indicate the area where the SLIP model [6] generally applies. 9

2.1 The calculated torque and force between the actuator and quadruped robot magnets. The stars indicate the force and torque chosen for the quadrupedal gait study. At 70 mm separation, the field intensity from the actuator magnet is 6.22 mT, resulting in applied force on each robot magnet of 3.46 mN and a maximum applied torque of 80.6 mN · mm. 16
2.2 A 1.6 g, 2 cm long quadrupedal robot with infrared tracking markers standing next to a US penny. 18
2.3 Magnet dipole orientations for the gait configurations. Clockwise from top-left: pronking, bounding, pacing, and trotting. 21
2.4 A schematic showing the phase offsets used for the set of back legs. The offsets were achieved by both rotating the magnet when assembling the quadruped as well as printing an offset in the leg itself. . . . 22
2.5 Experimental setup showing infrared (IR) cameras and the magnet and motor mounted to the linear stage. The right side shows both a photo and schematic view of how the magnet dipoles interact to create a torque on the robot legs. 23
2.6 Solid model of the 3X rough terrain created from a normal distribution with an upper bound equal to 3 times the hip height of the quadruped (16.9 mm) and a lower bound of 0 mm. The 2X terrain looks similar, with blocks of lower height. 24
2.7 Motion data from the four gaits on flat terrain, from left to right: pronking, bounding, trotting, pacing, and from top to bottom: longitudinal, lateral, and vertical positions, and robot roll, pitch, and yaw. 27
2.8 Average speed and standard deviation over seven trials of different back leg offset angles from 0° to 337.5° in 22.5° increments. The driving speed is constant at 4 Hz. 29
2.9 Average speed and standard deviation over seven trials for one robot for each of the different gait configurations of the quadruped. Trials were conducted from 2.0 Hz to 12.4 Hz. 31
2.10 Video stills of robot pronking, actuated at 10 Hz. 32
2.11 The percentage of robots accomplishing traversing a rough terrain. The vertical dotted line corresponds to the RMS roughness value of a step height at hip height. 35
2.12 A quadrupedal robot failing to cross rough terrain due to high step height. The step height from the block that the robots leg rests on to the block impeding the robots path is 4.7 mm. 36

3.1 A schematic of the experimental setup. Robot legs were compressed sinusoidally with the servomotor, which reads back the position and force exerted by the leg on the servo motor arm. 43
3.2 Mechanical impedance of different leg types (MRTV, PDMS, Soma Foama, and TangoBlack+) oscillated sinusoidally from 0.1 Hz to 50 Hz and displaced 0.5 mm. The fixed and free coxa trendlines are from [71] with cockroach legs displaced and oscillated similarly. . 45
3.3 Phase shift of different leg types (MRTV, PDMS, Soma Foama, and TangoBlack+) oscillated sinusoidally from 0.1 Hz to 50 Hz and displaced 0.5 mm. The fixed and free coxa trendlines are from [71] with cockroach legs displaced and oscillated similarly. 47
3.4 Least squares fit of the spring constant of different leg types (MRTV, PDMS, Soma Foama, and TangoBlack+) oscillated sinusoidally from 0.1 Hz to 50 Hz and displaced 0.5 mm. The fixed and free coxa trendlines are from [71] with cockroach legs displaced and oscillated similarly. 48
3.5 Least squares fit of the damping constant of different leg types (MRTV, PDMS, Soma Foama, and TangoBlack+) oscillated sinusoidally from 0.1 Hz to 50 Hz and displaced 0.5 mm. The fixed and free coxa trendlines are from [71] with cockroach legs displaced and oscillated similarly. 49
3.6 Exploded view of the modular quadruped solid model assembly. The compliant legs can be made in processes other than 3D printing and then attached to the hip 51
3.7 Average forward velocity of the different robot leg and gait configurations. The circle markers represent the average over 3 trials, while the shaded area represented the standard deviation. 55
3.8 The calculated phase shift for each gait type and leg type. The solid lines represent the average phase shift, averaged over more than 10 stride cycles of each of the three trials for a single robot, while the shaded area represents the standard deviation. 59
3.9 Calculated average maximum eigenvalue (solid line) and standard deviation (shaded area) for each gait and leg type. The eigenvalue is calculated over ten strides and averaged over three trials for a single robot for each leg type. 64
3.10 Schematic of the torque-driven SLIP model with a damper in parallel to the spring within the leg. 66
3.11 Experimental (left) and simulated (right) data points of legged locomotion plotted with the axes of non-dimensional speed (Froude number) and cost of transport. Each pair of plots is repeated with varying color maps, representing the energy recovery ratio (ERR), driving frequency, and energy phasing. 78

3.12 Experimental and simulated data points of legged locomotion plotted with the axes of relative stiffness and damping ratio. Each plot is repeated with varying color maps, representing cost of transport, Froude number, energy recovery ratio, eigenvalue, stride frequency, and energy phase shift. 79

4.1 Fabrication process for direct laser writing and embedded permanent magnets for actuation. 84
4.2 Fabricated 1 mg, 2.5 mm x 1.6 mm x 0.7 mm quadrupedal microrobot pictured with a dessicated bullet ant head (Paraponera clavata). . . . 86
4.3 The microrobot is actuated in a rotating magnetic field (B), resulting in a torque applied to each of the embedded magnets in the hip joints. The vertical and horizontal components of the magnetic field are generated from each coil pair. 89
4.4 (Left) CAD illustration showing the embedded legs within the (transparent) body to create a monolithic bearing. (Right) Photograph of printed component. 90
4.5 The average rotational frequency of a leg of the microrobot not in contact with the ground vs rotating magnetic field frequency. Solid line represents the average and the shaded area represents the standard deviation over >5 rotations. The dashed line visualizes when the rotational frequency of the leg is equal to the driving frequency. . 92
4.6 The average rotational frequency (solid line) and standard deviation (shaded area) over ten rotations of the leg actuated at 100 Hz (dashed red line) captured at 30 minute intervals (180,000 cycle intervals). . . 94
4.7 Robot speed vs rotating magnetic field frequency. Solid line represents the average over three trials and the shaded area represents the standard deviation for one robot. 96
4.8 Overlaid frames captured from video of the microrobot walking at approximately 9.5 body length per sec 96
4.9 Relative phasing of the kinetic energy to the gravitational energy of the robot pronking as a function of driving frequency. 98
4.10 In-phase energy profiles of gravitational and kinetic energy of the robot pronking at 20 Hz. 100
4.11 Energy profiles of the robot pronking at 35 Hz. In this trial, kinetic energy leads gravitational by 50°. 101

5.1 A solid model of the genetic algorithm designed force sensor. The input force and center of elasticity are connected through a rigid link. The deflection of the force sensor is observed at the center of elasticity. 110
5.2 Experimental setup for measuring the ground reaction force. The first camera focuses on the robot from a top-down view, while the second camera images the force sensor. 113

5.3 The average forward velocity (solid lines) and standard deviation (shaded area) over three trials of a robot actuated from 10 Hz to 70 Hz. 115
5.4 The position (top), velocity (middle), and acceleration (bottom) of the horizontal (left) and vertical (right) components of the center of mass of the robot actuated at 15 Hz. 117
5.5 The position (top), velocity (middle), and acceleration (bottom) of the horizontal (left) and vertical (right) components of the center of mass of the robot actuated at 15 Hz. 119
5.6 The average horizontal kinetic energy (blue) and gravitational potential energy (red) over a gait cycle of the robot actuated at 15 Hz. . . 121
5.7 The average horizontal kinetic energy (blue) and gravitational potential energy (red) over a gait cycle of the robot actuated at 35 Hz. . . 122
5.8 Calculated percentage congruity of the robot actuated from 10 Hz to 70 Hz. The marker represents the average value, with the shaded area representing one standard deviation over three trials with one robot . 123
5.9 Calculated percentage recovery of the robot actuated from 10 Hz to 70 Hz. The marker represents the average value, with the shaded area representing one standard deviation over three trials with one robot. . 125
5.10 Calculated ground reaction force on one leg of one robot actuated at 15 Hz averaged over three trials. 127
5.11 Calculated ground reaction force on one leg of one robot actuated at 35 Hz averaged over three trials. 128
5.12 Simulated horizontal (blue) and vertical (red) position, velocity, and acceleration of the center of mass of a torque-driven grounded SLIP model driven at 15 Hz. 131
5.13 Simulated horizontal kinetic energy (blue) and gravitational potential energy (red) of the center of mass of a torque-driven grounded SLIP model driven at 15 Hz. 133
5.14 Simulated horizontal (blue) and vertical (red) ground reaction forces of a single leg a torque-driven grounded SLIP model driven at 15 Hz. 135
5.15 A schematic of the torque-driven grounded SLIP model showing the point of momentum transfer between stance phases. 137
5.16 Simulated trajectories of the center of mass for $k_{rel} = 100$ (blue), $k_{rel} = 10$ (red), and $k_{rel} = 3$ (green) of a torque-driven grounded SLIP model plotted in polar coordinates. 139
5.17 Simulated non-dimensional speed ($\frac{v^2}{gl}$) against varying relative stiffnesses $k_{rel} = \frac{kl}{mg}$. 140

Chapter 1

Introduction

Insects access the world in ways robotics are just beginning to explore, and in part, are enabled by their morphology and highly dynamic mobility. This dissertation focuses on one of the main challenges related to small robots, namely how to effectively locomote at size scales less than 1 g in body mass. Creating highly dynamic small-scale, insect-inspired robots requires more than simple imitation of morphology. An understanding of the complex interactions between mechanism, environment, and control found in biological systems is required for effective translation into robotic systems. The work presented here provides an experimental platform and synthetic physical models to gain insight into the underlying dynamics of locomotion. By understanding the underlying principles and locomotion models associated with low-mass locomotion, robot designers can explore the trade-offs associated with design parameters, e.g. leg stiffness and damping, ultimately creating robots capable of locomoting at high-speeds ($>$ 10 body lengths per second) efficiently and stably.

Insect-scale robots mimicking the abilities of insects would be more than just impressive feats of engineering. Ultimately, these insect-scale robots would have a host of uses. For example, networks of small mobile sensors could be used for exploration or for collaborative building as seen in termite colonies. Realizing autonomous robots at this scale requires advances in many research disciplines including energy

storage, actuation, communication, and sensors together with mechanical design and control. While this work does not explicitly address these issues, this work explores engineered physical models to understand the underlying principles of locomotion at the insect-scale, informing future design and controls. With this in mind, the following sections explore insect locomotion, mathematical locomotion models, and insect-inspired robots to provide an overview of current research in these areas, highlighting the research opportunities to study locomotion at sub-gram scales.

1.1 Insect locomotion

Legged locomotion in small-scale robots has been inspired by the extraordinary performance of insects, such as cockroaches and ants. Understanding the mechanics of insect locomotion builds templates for design and control of both similarly sized and larger robots. Cockroach locomotion has been extensively studied to understand the mechanics [1, 2, 3, 4] and performance over rough terrain (terrain with obstacles taller than the hip height) [5]. The motion of the center of mass of the cockroach reveals a running, or bouncing, gait, characterized by the center of mass lowering at mid-stance and subsequent aerial phase. The cockroach adopts a running gait even at the lowest of stride frequencies. The fluctuations of the energy of the center of mass are similar to that of larger animals also running. Measuring the ground reaction force of the cockroaches further reveals similarities in force production relative to larger animals [1]. Ultimately, this similarity is unified in [6], showing a common locomotion mode of animals, from cockroaches to horses.

While legged locomotion exists down to body masses of 10-100 μg [7], scaling models, based primarily on vertebrates [8, 9, 10], may not apply to predict behaviors in very small animals, below 1 g in body mass. Ants, as part of the family *Formicidae*, range in body mass from <1 mg [11] to 480 mg [12] and are capable of locomoting at speeds greater than 10 body lengths per second. The mechanics and ground reaction forces observed in [13, 14, 15] reveal some similarities to cockroach locomotion. However, ants run using a gait without a distinct aerial phase. This lack of aerial phase suggests that locomotion at this scale, in at least some organisms, could be described as grounded running, taking advantage of their ground contact to locomote effectively. Given the complexity of contact models between feet and ground, unifying mathematical models at this scale do not yet exist to predict performance. Instead, insight into these models can be found from physical models, both biological models such as ants as well as robotic models at this scale.

1.2 Legged locomotion modeling

Two of the primary locomotion models describing locomotion in the sagittal plane are the inverted pendulum (IP) and spring loaded inverted pendulum (SLIP). Figure 1.2 shows a schematic of the two models. The IP model predominately describes walking, however, it is hypothesized that gram-scale running can adopt this profile during high speed running [16]. Figure 1.2 (left) shows a schematic of the model, represented by a point mass on top of a massless, rigid leg as an inverted pendulum [17]. In the model, the mass is vaulting, reaching an apex at mid-stance, and

propelling the forward kinetic motion from the gravitational energy. This model describes locomotion through the exchange of gravitational energy for kinetic energy. For small-scale locomotion, surface forces dominate inertial forces. Inertial forces that scale with volume become relatively less important when compared to surface forces, such as friction, that scale with area as mass scales down. Therefore, there is a scaling limit at which this type of energy exchange for locomotion is practical.

The most common model used for running is the spring loaded inverted pendulum (SLIP) [6]. In this model, an inverted pendulum is constructed with a point mass and massless spring as a leg (Figure 1.2, right). This model captures the trajectory of the center of mass for animals of different sizes and different numbers of legs. During the locomotion of SLIP, the center of mass falls to its lowest position at the mid-stance of the gait cycle, compressing a spring. The center of mass rebounds in the second half of the gait cycle, releasing stored energy. This model captures the running dynamics of animals over several magnitudes of body mass because the virtual leg spring, defined as $k_{rel} = F/mg \Big/ \Delta l/l$, is similar across different animals from a cockroach to a horse [6]. While elastic energy storage with a similar k_{rel} is possible for insects at any scale due to the presence of chitin and lower modulus materials like resilin, an elastic protein [18], it is unlikely that legs can be compressed entirely passively at small scales due to small inertial forces and high surface forces. Since models like SLIP largely rely on passive inertial forces, it is difficult to distinguish where and if there is a transition from these models relative to size from biological data alone, which can exhibit a large number of active degrees of freedom, as opposed to the minimal passive degrees of freedom shown in the models.

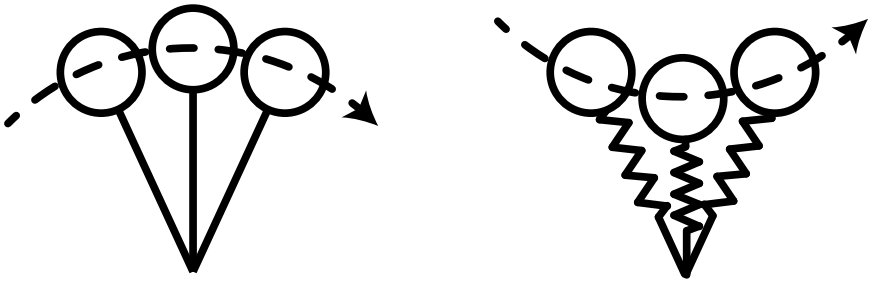

Inverted pendulum (IP)

Spring loaded inverted pendulum (SLIP)

Of course legged locomotion is a more complex interaction, including friction, drag, and other surface forces that vary in magnitude depending on size. However, these locomotion models serve as templates for control schemes [19, 20], biomechanics study [21, 22], and design [23], making the utility of a locomotion models clear. To achieve similarly capable insect-scale robots we must understand corresponding locomotion models relevant to the sub-gram scale. To develop mathematical models describing sub-gram locomotion, physical models are needed to help identify key parameters. Physical models can be biological. However, the focus of this work is on creating synthetic, engineered physical models, where the designer has control over complexity and can implement parameter ranges, such as leg stiffness, beyond biologically relevant ranges.

1.3 Insect-inspired robots

Robots at all scales have been inspired by the locomotive feats of insects. Figure 1.1 compares the forward velocity of some of these legged robots to insects. RHex (7 kg) provides a particularly versatile platform to study the biomechanics of locomotion [24]. Speeds up to 1 body length per second were demonstrated with an

alternating tripod gait, and the compliant C-shaped legs enable RHex to traverse terrain with with height variations exceeding hip height [24]. Implementing a wave gait, where pairs of legs act sequentially down the length of the body, increased running speed to 4.5 body lengths per second and enabled climbing at 45° inclines [25] and up stairs [26]. iSprawl (0.3 kg) is approximately 150 times more massive than the 2 g cockroaches [5] that inspired it. iSprawl's push/pull mechanism in the legs, combined with a passive rotational compliance at the hip enable the robot to achieve top speeds of 15 body lengths per second. DASH is a 16.2 g hexapedal robot. The lightweight and compliant design achieved relative stiffnesses,$k_{rel} = F/mg \Big/ \Delta l/l$, a ratio of inertial forces to virtual spring forces, similar to biological data ($k_{rel} \approx 10$). By tuning the design for similar force production and elasticity to biological organisms, DASH is capable of achieving top speeds of 15 body lengths per second. Due to the size of these robots, they can be reliably described using the SLIP model, informing design and control of these robots. Each of these large robots (>10 g) robots exploited the underlying passive dynamics of locomotion for design and control, demonstrating robots capable of high speed running.

Robots designed at gram scales are typically limited in their utility to study locomotion. Previous work in gram-scale insect-inspired legged robots include RoACH [27], a centipede-inspired millirobot [28], and HAMR [29]. RoACH is an autonomous 2.4 g hexapedal robot. The design kinematically links two sets of three legs together, creating an alternating tripod gait and locomoting at 1 body length per second. RoACH's minimal actuation, achieved through two SMA wires, controlled six legs, producing an alternating tripod gait, demonstrating the versatility of un-

deractuated robots to produce an insect-like gait [27]. A centipede-inspired, 20-leg, 2.2 g millirobot achieved speeds of 0.7 body lengths per second, and provided insight to some of the mechanisms in myriapoda, a subphylum of arthropods containing millipedes and centipedes, locomotion demonstrating that passive undulations, as compared to a robot without body compliance, increased performance [28]. HAMR is one of the more successful gram-scale platforms, demonstrating high speed locomotion, up to 10.1 body lengths per second [29]. The lightweight design combined with two actuated degrees of freedom per leg allows control authority over the robot legs running at high speeds [30] and of the trajectory of the robot itself [31]. The utility of the HAMR robot is not only limited to robotics research, but serves as a platform for investigating locomotion at the gram-scale [16], showing characteristics of both the SLIP and IP models during the locomotion. Autonomous versions of HAMR have even been demonstrated at 1.7 g [32], 2.1 g [33], and 2.8 g [34] but were limited to speeds below 4 body lengths per second.

Robots at the micro-scale are impressive feats of engineering. However, their performance has paled in comparison with ants of similar sizes. Ebefor's 80 mg silicon robot was driven by the thermal actuation of polyimide hinges to raise and lower legs, achieving speeds of 0.4 body lengths per second. The robots in [35, 36], 128 mg and 480 mg, were designed with many (> 6) legs, propelling them forward with an overall ciliary motion. Yasuda et al. created a robot structure (≈ 5 μg[1]) driven by mechanical vibrations. The entire structure is excited at the resonant

[1]The body weight was not explicitly reported in [37], but is estimated from designed dimensions and density of silicon (2.33 g/cm^3)

frequency of the spring-mass systems, and the robot moves forward at 2.8 body lengths per second [37]. Hollar et al. demonstrated a 10 mg legged robot using polysilicon hinges to rotate the legs [38]. While the robot did not walk forward, this demonstrated a robot moving autonomously. Contreras et al. demonstrate an 18 mg walking robot powered by electrostatic actuators [39], showing the capability of MEMS actuators to power milligram-scale walking. Tanaka et. al designed a quadrupedal microrobot ($\approx$ 200 mg[2]) with two four-bar linkages as legs, creating a circular footpath [40]. Though the speed was not reported for this robot, earlier versions have achieved forward velocities of 0.6 body lengths per second [41]. More recently, Qu et al. demonstrated lead zirconate titanate (PZT) actuated legged microrobots to study the ground contact at scales as low as 2.1 mg [42], continuing the ground contact and locomotion studies from [43], which showed a quadrupedal robot at 160 mg. This work set up an experimental platform to understand ground contact and forward propulsion in small-scale systems. One of the fastest microrobots was presented by Vogtmann et al. and incorporated elastic structures with magnetic actuation to demonstrate high velocity (over 5 body lengths per second) running at 25 mg. While all of these robots work towards creating autonomous microrobots, creating microrobots that rival ant speed performance requires understanding and taking advantage of the dynamics of locomotion at relevant size scale.

[2]The body weight was not explicitly reported in [40], but is estimated from designed dimensions and density of silicon (2.33 g/cm^3)

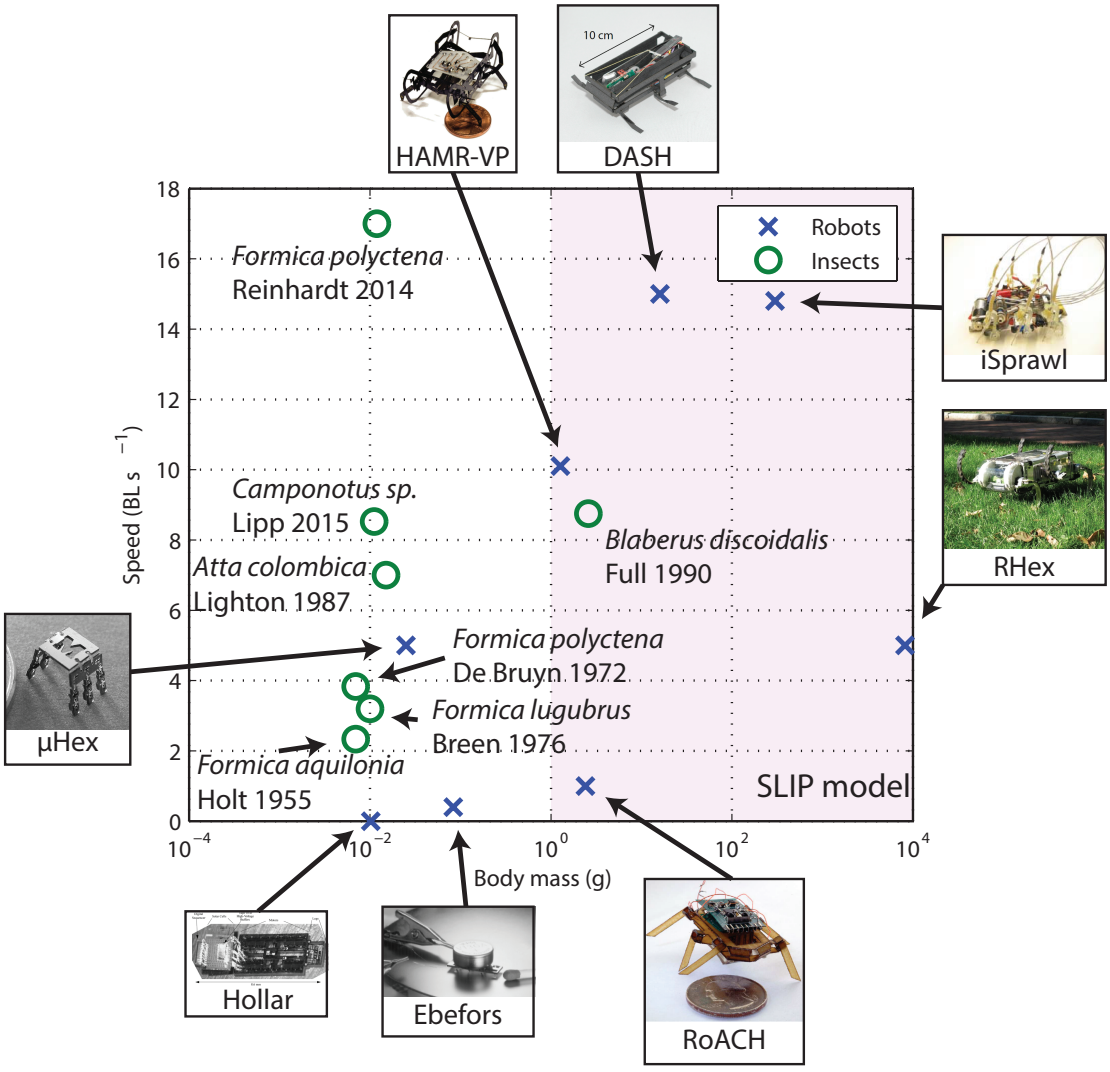

Figure 1.1: Speed vs. body mass of select legged robots [29, 23, 27, 44, 38, 45, 46, 24] and insects [47, 48, 49, 50, 51, 52, 14]. The shaded right half of the plot indicate the area where the SLIP model [6] generally applies.

1.4 Outline of Dissertation

The document is divided into four chapters: the gram-scale experimental platform, incorporating passive compliance and damping in legs for dynamic stable locomotion, an experimental platform for the milligram-scale, and the mechanics of milligram locomotion. Broadly, the dissertation is divided into two main categories: experimental platforms and resulting locomotion studies. Overall, this work guides design principles for future small-scale (<1 g) legged robots, exploring aspects of mechanical design and embedded morphological control through passive dynamics.

Chapter 2 sets up the experimental platform used for both making gram-scale robots as well as testing their locomotive capabilities, and is largely based on the work published in [53]. This chapter discusses the design of both the robot and the experimental platform, including the equations used in magnetic actuation, allowing for the calculation of the applied torque to the robots to inform future robot designs. Chapter 3 explores the use of viscoelastic leg materials as a means of mechanical control. This chapter experimentally evaluates the locomotion performance of different configurations of gait and leg type on a gram-scale robot. The experimental work is connected to simulations of a torque-driven SLIP model to explore the leg design space of the robot, through compliance and damping in the leg, and ultimately providing insight designing gram-scale robots for speed and stability.

Chapter 4 scales down the robot design presented in previous chapters from 1 g to 1 mg and evaluates the performance of small-scale, monolithically printed rotary joints, providing an upper-bound to required actuation torque and achiev-

able rotational speeds. This chapter also considers the locomotion performance of the robot, evaluating the speed and energy phasing of the robot. Finally, chapter 5 uses the milligram-scale robot to explore the mechanics of legged locomotion. Kinematic data about the robot center of motion is presented in conjunction with ground reaction force data from a custom force sensor. These data sets provide an understanding of milligram-scale locomotion and give insight to relevant models for the milligram-scale. Bringing together locomotion data with modeling efforts provides insights into ant locomotion as well as a framework for design and control of future milligram-scale legged robots.

Chapter 2

Magnetic actuation for studying legged locomotion

The majority of the material in this section is taken from "Gait exploration of sub-2 g robots using magnetic actuation" [53]

The work presented in this chapter outlines a method by which permanent magnets can be used to study locomotion in sub-2 g legged robots simply and rapidly. Specifically, this chapter provides a case study, exploring different gaits on both flat and rough terrain. These gaits were motivated by different gait strategies shown in both biology [2, 5] and robotics [25, 26].

Section 2.1 provides calculations for forces and torques between a permanent magnet used to generate an external field and the magnets embedded in the robot and describes the limitations expected in this method. Section 2.2 discusses the design and fabrication of the respective robots. Section 2.3 describes the experimental setup used for testing the robots at a consistent speed over a distance of more than 20 body lengths. Section 2.4 provides results from testing different gaits and splay angles at a variety of speeds and over multiple terrains. Finally, Section 2.5 discusses conclusions drawn from the experiments.

2.1 Magnetic actuation

Magnetics are an advantageous actuation method for small-scale robots since it is both wireless and easily integrated with small-scale robotic components. By using magnetic actuation, additional complexities associated with integrating power sources, control, and actuators are bypassed. Magnetically actuated microrobots have been demonstrated in several contexts including micromanipulation [54], modular robotics [55], magnetically actuated endoscopic robots [56], and micro surgical robots [57]. Magnetics have also been demonstrated in a variety of locomotion modes such as tumbling [58, 59, 60], stick-slip [61], and legged locomotion [62].

The robots in this dissertation are actuated by the interaction between permanent magnets embedded in the robot legs (robot magnets) and the magnetic field generated by an external permanent magnet (actuator magnet). It should be noted that this setup enables only one input control signal from the actuator magnet but controls the four magnets embedded within the quadrupedal robot simultaneously, creating an underactuated system. Any relative shifts in the control timing between the magnets in the legs must be done mechanically and cannot be controlled on the fly.

A point-dipole model can be used to calculate the expected torque and force between two permanent magnets [63]. The field produced from a magnet, $\mathbf{h}$, is given by

$$\begin{aligned} \mathbf{h} &= \frac{1}{4\pi \left|\left|\mathbf{p}\right|\right|^3} H \mathbf{m_a} \\ H &= 3\hat{\mathbf{p}}\hat{\mathbf{p}}^\top - I \end{aligned} \tag{2.1}$$

where $\mathbf{p}$ is the vector describing the distance from the center of the actuator magnet to a point of interest and $\hat{\mathbf{p}}$ is the unit vector of $\mathbf{p}$, $\mathbf{m_a}$ is the three-dimensional vector of the magnetic dipole moment of the actuator magnet, and I is the 3-by-3 identity matrix [63].

The robot magnets will attempt to align with the external field generated by the actuator magnet resulting in a torque on the robot magnets. The maximum available torque, τ, is given by

$$||\tau||_{max} = \mu_0 \, ||\mathbf{h}|| \, ||\mathbf{m_r}|| \tag{2.2}$$

where μ_0 is the magnetic permeability, $\mu_0 = 4\pi \times 10^{-7}$ H/m (in vacuum), $\mathbf{h}$ is the field calculated from Equation 2.1 and $\mathbf{m_r}$ is the magnetic dipole moment of the robot magnet [63].

The gradient in the magnetic field, from the actuator magnet, will also generate a force on the robot magnets. The vector describing the force on the robot magnet from the actuator magnet is given by

$$\begin{aligned} \mathbf{f} &= \frac{3\mu_0}{4\pi \, ||\mathbf{p}||^4}(\hat{\mathbf{p}}\mathbf{m_r}^\top + \mathbf{m_r}\hat{\mathbf{p}}^\top + (\mathbf{m_r}^\top \hat{\mathbf{p}})Z)\mathbf{m_a} \\ Z &= I - 5\hat{\mathbf{p}}\hat{\mathbf{p}}^\top \end{aligned} \tag{2.3}$$

where $\mathbf{p}$ is the vector describing the distance from the center of the actuator magnet to the center of the robot magnet, in Cartesian space, and $\hat{\mathbf{p}}$ is the unit vector of $\mathbf{p}$ [63].

Using the methodology in [64], the dipoles of both the actuator magnet, $\mathbf{m_a}$, and robot magnet, $\mathbf{m_r}$, were found by measuring the projection of the magnets' magnetic field using three Hall sensors (Analog Devices AD22151) oriented orthog-

onally. The magnitude of the magnetic dipoles of the actuator and robot magnets used in these studies are 10.7 $A \cdot m^2$and 13 $mA \cdot m^2$.

Using Equations 2.1-2.3, the expected torques and forces on the robot magnets due to the actuator magnet at varying separations can be calculated. Figure 2.1 shows the torque and force between a 1 in^3 actuator magnet and the robot magnets. In this application, magnetic force acts like an additional load or mass on the robot. Therefore, to reduce the applied force to approximately the robot mass, a larger distance is used, which also reduces the maximum available torque on the robot legs. The stars in Figure 2.1 indicate the force and torque chosen for the studies. For the quadrupedal gait study, at 70 mm separation, the field intensity from the actuator magnet is 6.22 mT, resulting in applied force on each robot magnet of 3.46 mN and a maximum applied torque of 80.6 $mN \cdot mm$. Figure 2.1 also provides a sense of how sensitive force and torque are to deviations from this nominal separation distance, and ultimately a sensitivity of using magnets as the actuation principle. If the quadruped robot moves away from its ideal position directly above the actuator magnet, force and torque will decrease. Increasing the distance between the magnets by 7 mm (corresponding to a 7 mm change in position vertically or 32 mm lateral change in position) results in a 25% decrease in torque.

2.1.1 Frequency of operation

There are limitations to the use of permanent magnets as an actuation method, as discussed in [63]. There is an upper bound, the step-out frequency, where the

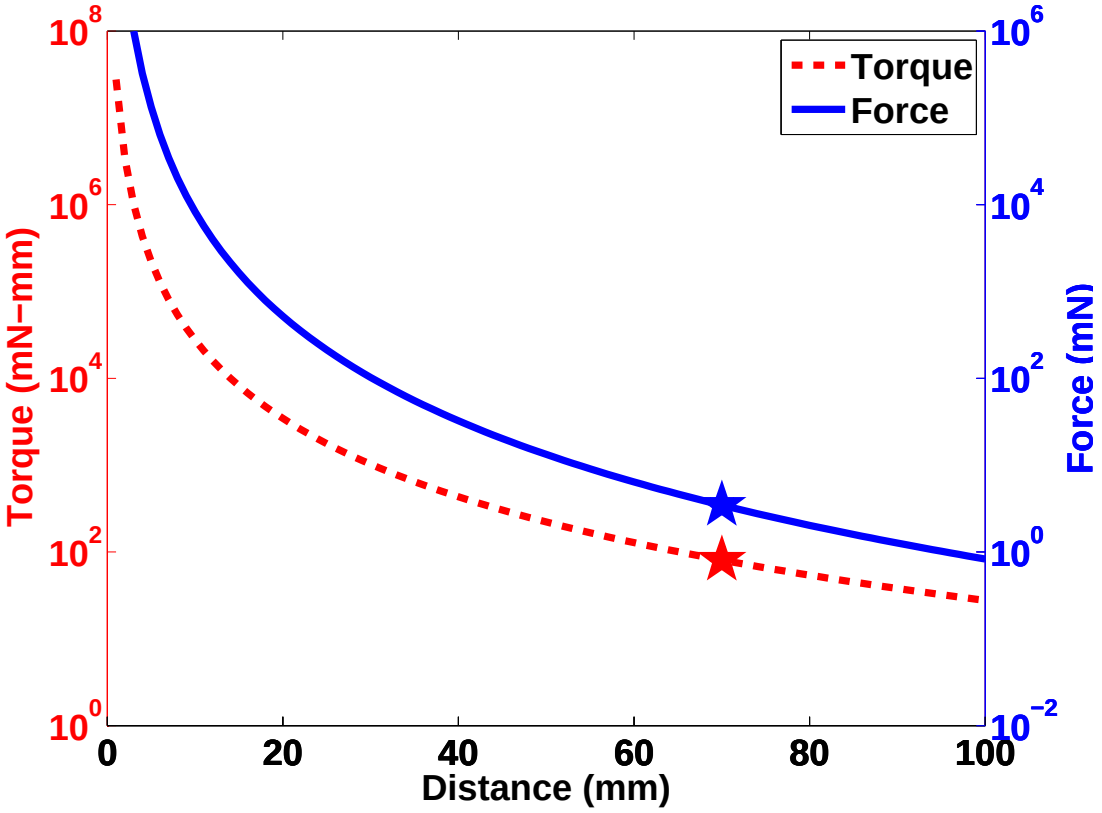

Figure 2.1: The calculated torque and force between the actuator and quadruped robot magnets. The stars indicate the force and torque chosen for the quadrupedal gait study. At 70 mm separation, the field intensity from the actuator magnet is 6.22 mT, resulting in applied force on each robot magnet of 3.46 mN and a maximum applied torque of 80.6 mN $\cdot$ mm.

magnets embedded in the robot are no longer in sync with the actuator magnet. The step out frequency is calculated in Equation 2.4 [63].

$$||\omega_{\mathbf{so}}|| = \frac{||\tau||_{max}}{c} \tag{2.4}$$

$\omega_{\mathbf{so}}$ is the step-out frequency and c is a rotational damping term. The 3D printed quadrupedal robots have a rotational damping term caused by friction in the 3D printed joints. This frequency can be increased by moving the magnets closer together, increasing the maximum torque. The chosen 70 mm separation results in a step-out frequency of 12.8 Hz, assuming a rotational damping term $c = 1 \times 10^{-6}$ N $\cdot$ m $\cdot$ s (inferred from experimental data). No attempt in this study was made to minimize actuator power or locomotion efficiency. However, understanding the power costs of locomotion can help inform future autonomous robot designs by providing an upper bound to the needed torque, which can be matched to a suitable actuator.

The power required for the robot to locomote can be calculated from the torque applied to the robot magnets (Equation 2.2) and the actuation frequency ($P = \tau\,\omega\,n_{legs}$). At the highest frequencies tested for the different robots, 12.4 Hz, the calculated power required to move the robot was 25.2 mW.

2.2 Robot design

The robot design (Figure 2.2) was inspired by RHex due to its ability to traverse rough terrain [24]. However, instead of the 6 legs used in RHex and insects, the

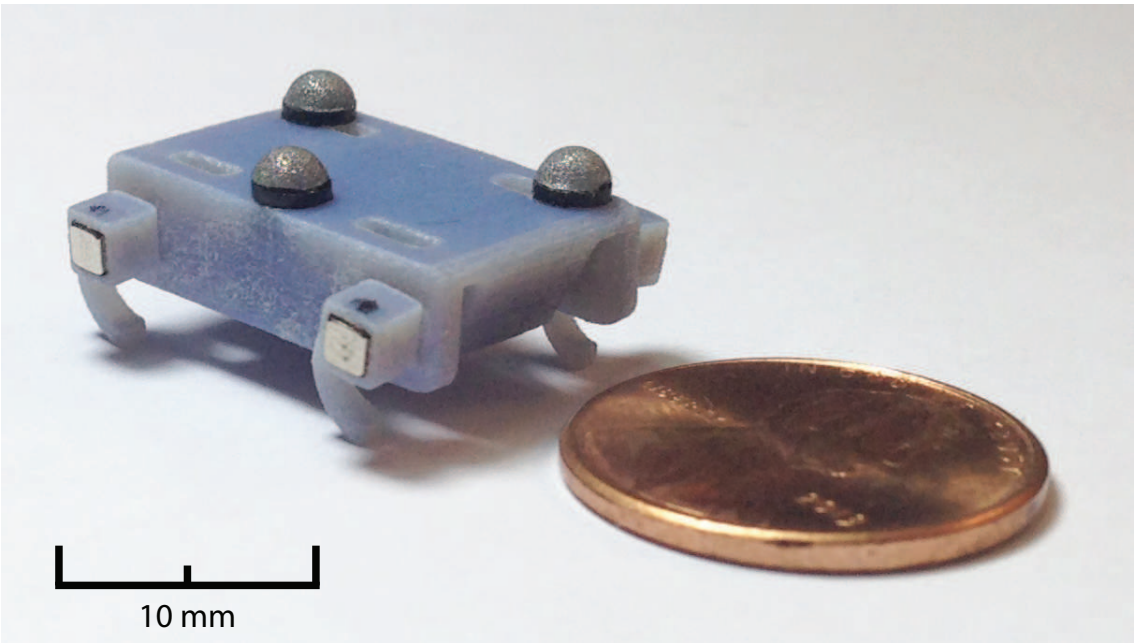

Figure 2.2: A 1.6 g, 2 cm long quadrupedal robot with infrared tracking markers standing next to a US penny.

robots used in this study have only four legs to prevent the legs from colliding and locking during locomotion as well as providing enough space between the magnets in the front and rear legs to minimize any interactions between them. Each leg is shaped like a "C", similar to RHex, although due to materials and fabrication, the legs are not compliant. Each hip joint rotates fully due to the torque on a permanent magnet embedded at each hip.

2.2.1 Fabrication

The quadrupeds were monolithically 3D-printed on an Objet 30 Pro 3D printer using a rigid opaque photopolymer (VeroBlue RGD840). After printing, the support material was removed mechanically using a dental pick, freeing the joints to rotate. Small magnets, N50 neodymium cube magnets with a 2 mm side length (SuperMagnetMan C0020) were placed in the hip joint sleeves. They were held in place by the surrounding material in a friction fit. It should be noted that the only assembly required is placing magnets in the hip joints, making design iterations simple and fast, limited largely by the design and printing time. An assembled quadruped is shown in Figure 2.2. Each quadruped is 20.0 mm long, with a hip height of 5.64 mm and a mass of 1.61 g.

2.2.2 Gait Configuration

Orienting the embedded magnets mechanically programs different gaits by adjusting the relative timing between legs. Figure 2.3 shows the orientation of the magnets to

achieve the different gait configurations: pronking, bounding, trotting, and pacing. Pronking has all of the magnets in the legs oriented in the same direction. Bounding has the magnets in the anterior set of legs in the same direction, while the magnets in the posterior set of legs are offset 180° from the anterior set. Trotting has the magnets in the right anterior leg and left posterior leg in the same direction while the left anterior leg and right posterior leg have the magnets offset 180° with respect to the first pair. The pacing gait has the left set of legs having the same magnet orientations and the right set of legs having the opposite orientation with respect to the first pair. It should be noted that the gait cannot be changed during locomotion as the magnets are placed manually. The goal of this work is to better understand the performance of these gaits for improved gait control of autonomous robots at these size scales in the future.

2.2.2.1 Bounding subset

Changing the timing between sets of legs has been shown to enhance locomotion capabilities in platforms such as RHex [26]. Since the methodology presented in this dissertation is for underactuated systems with only one input signal, the phase offsets of the legs must be implemented mechanically. This is done in two ways: rotating the magnet implanted in the hip joint during assembly and rotating the sleeve for the magnet printed on the body. Four different builds were constructed so that there was a mechanical offset in increments of 22.5° in the back legs with respect to the front legs. Rotating the magnets and using the different builds allowed

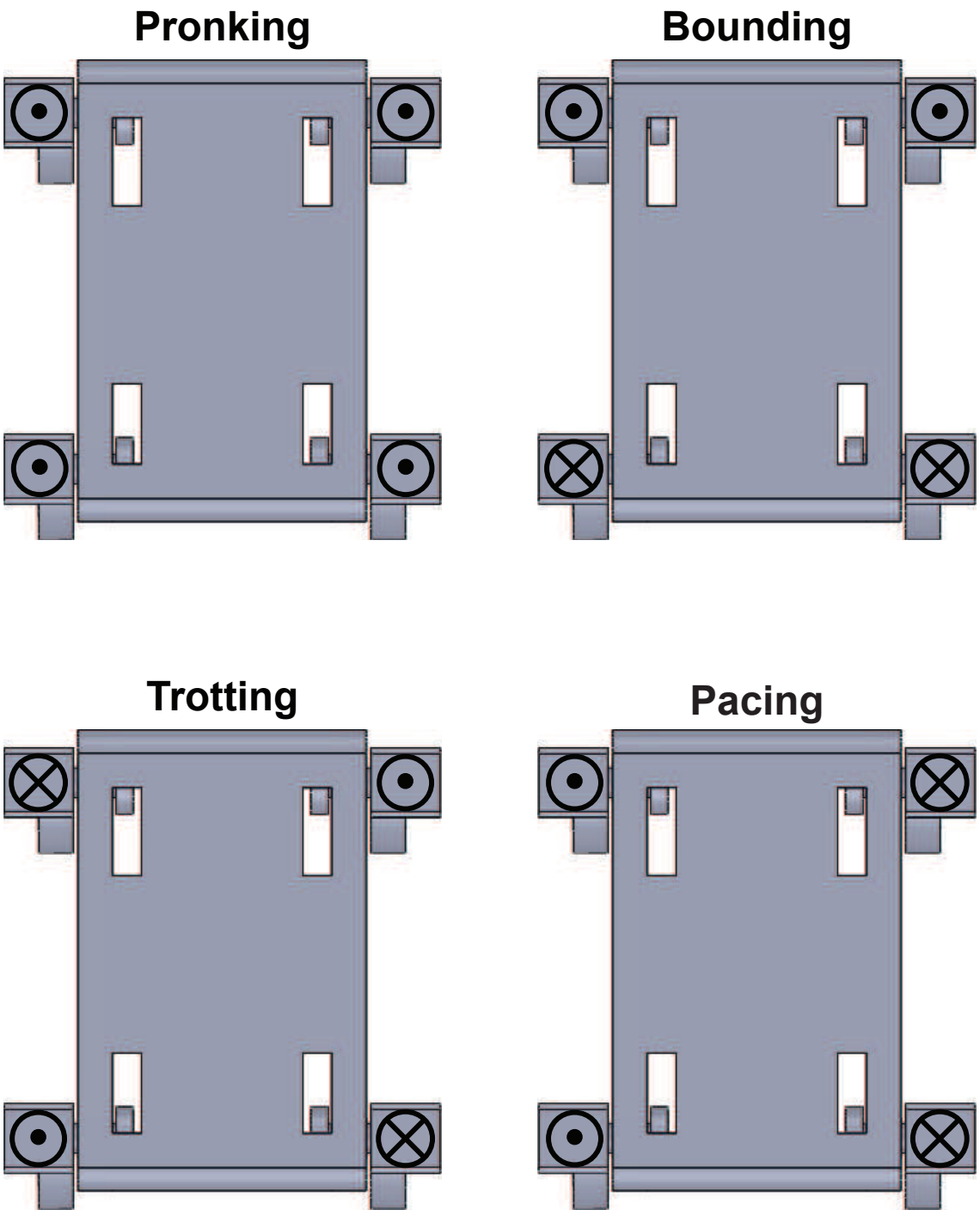

Figure 2.3: Magnet dipole orientations for the gait configurations. Clockwise from top-left: pronking, bounding, pacing, and trotting.

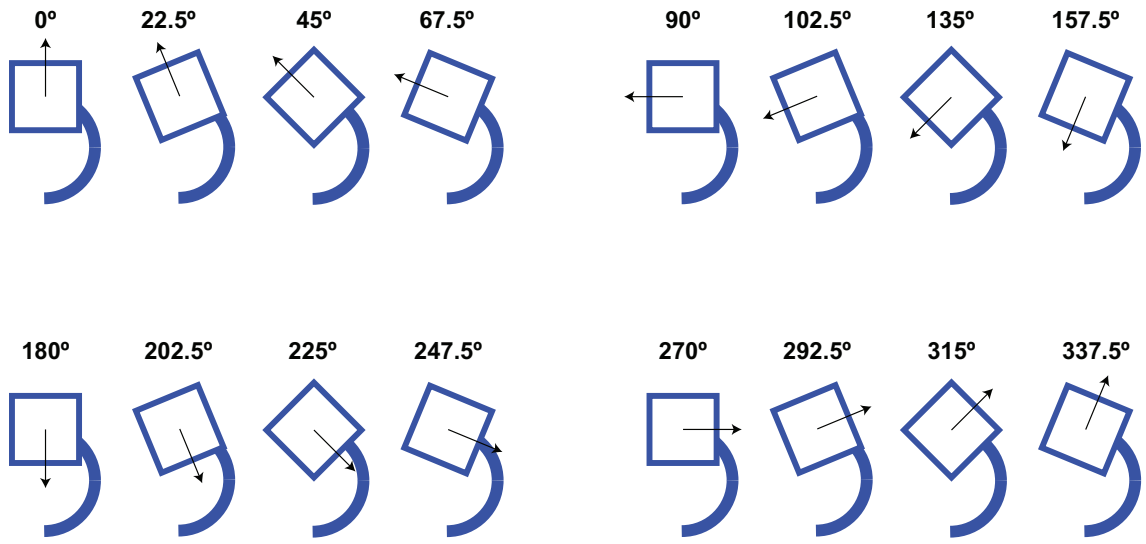

Figure 2.4: A schematic showing the phase offsets used for the set of back legs. The offsets were achieved by both rotating the magnet when assembling the quadruped as well as printing an offset in the leg itself.

for phase offsets in the back legs from 0° to 337.5° in 22.5° increments. It should be noted that 0° configuration corresponds to a pronking gait and 180° corresponds to bounding. The achievable configurations of the back legs of the different builds are shown in Figure 2.4.

2.3 Experimental setup

Each quadruped was actuated by an external rotating magnetic field provided by mounting a 1 in^3 N55 neodymium magnet to a 25 mm diameter DC motor. The actuator magnet and motor were placed in brackets and attached to a linear stage (Zaber A-LSQ450D-E01). The mounted magnet setup is shown in Figure 2.5.

A thin sheet of acrylic was supported above the magnet. To maintain the

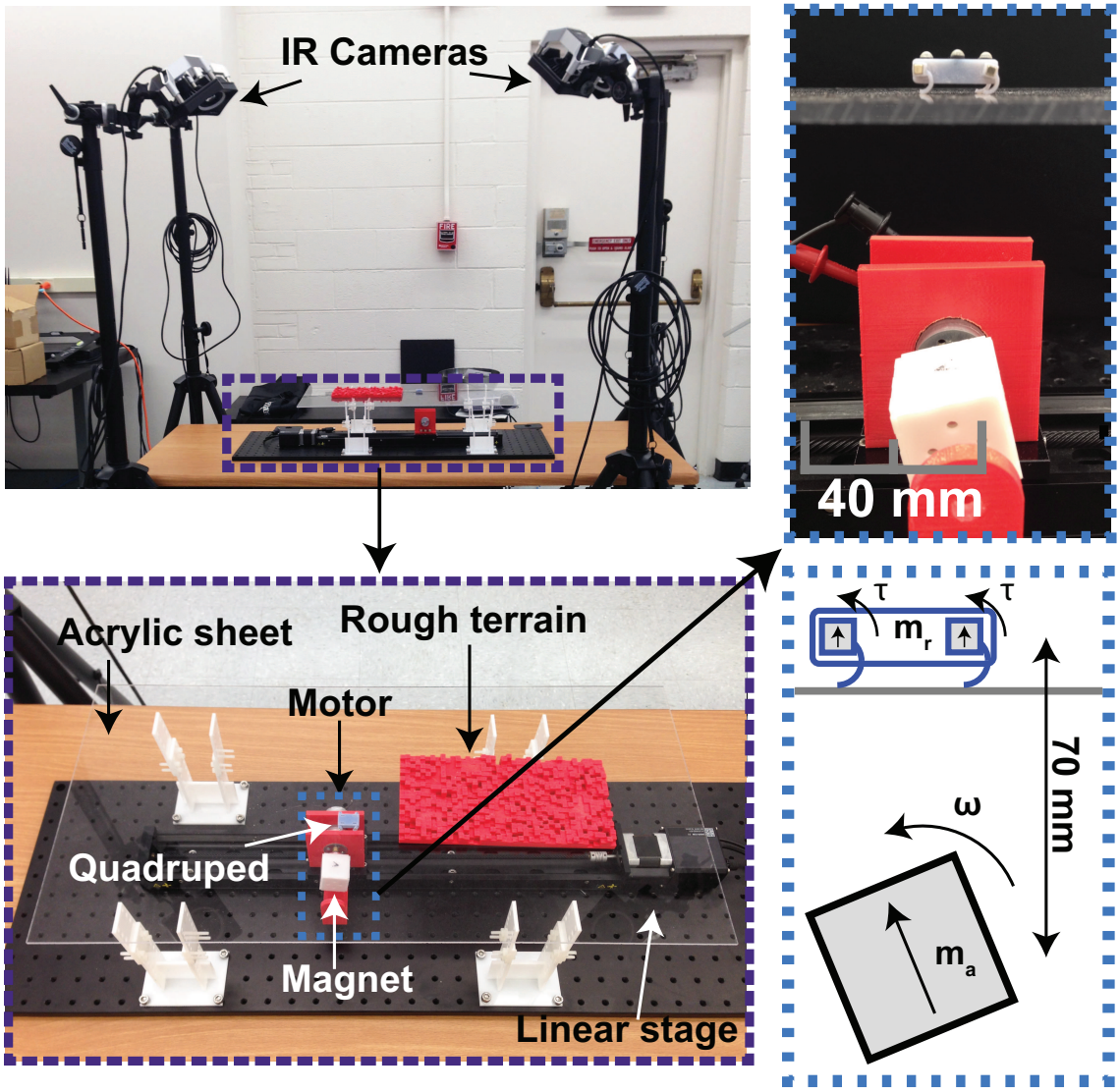

Figure 2.5: Experimental setup showing infrared (IR) cameras and the magnet and motor mounted to the linear stage. The right side shows both a photo and schematic view of how the magnet dipoles interact to create a torque on the robot legs.

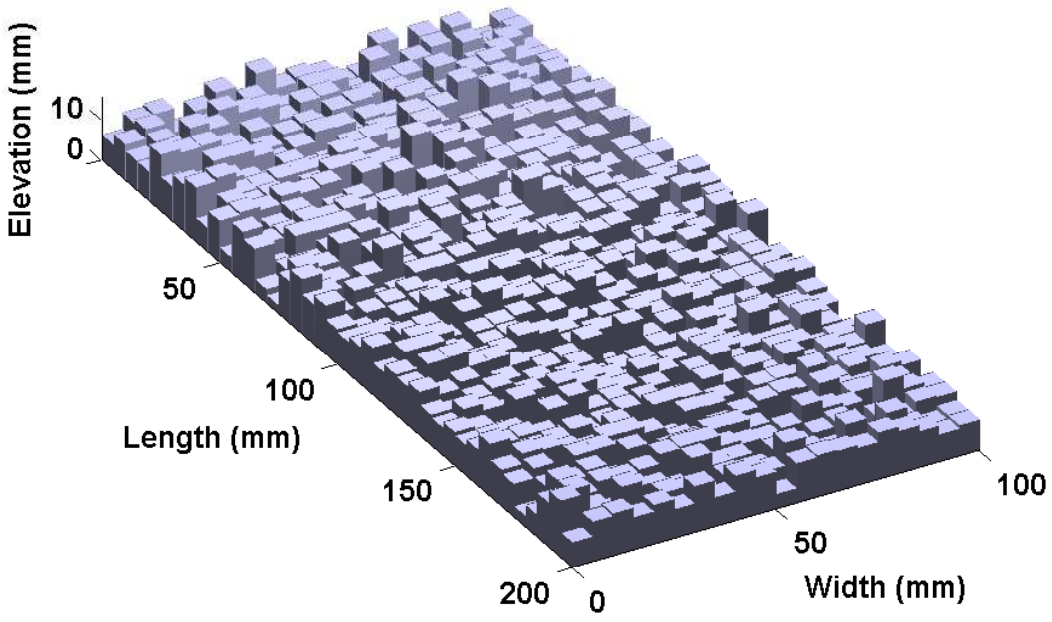

Figure 2.6: Solid model of the 3X rough terrain created from a normal distribution with an upper bound equal to 3 times the hip height of the quadruped (16.9 mm) and a lower bound of 0 mm. The 2X terrain looks similar, with blocks of lower height.

desired separation distance between the actuator magnet and the robot, the actuator magnet needs to be moved, keeping it centered under the quadruped. Kinematic information of the robot, including the the longitudinal, lateral, and vertical position center of mass position as well as the roll, pitch, and yaw angle, was obtained by tracking three IR-reflective markers (3 mm hemispherical facial markers, OptiTrack) attached to the robot using four top-view cameras (OptiTrack, Prime 17W, 360 FPS). Since the robots are tracked, the measured velocity of the quadruped can be fed into the control for the linear stage in real time, keeping the stage's velocity matched to the robot's.

Each quadruped was tested walking on a flat acrylic sheet in this rotating magnetic field over a distance of 450 mm (22.5 body lengths) during several trials. The longitudinal, lateral, and vertical position, as well as the roll, pitch, and yaw of the quadruped were tracked using the infrared tracking system. Experimental results showed that robot performance on flat terrain did not significantly change when torque was reduced to 75% of its nominal value. Experiments in which the distance between the actuator magnet and robot was greater than 77 mm (corresponding to 1.6 body lengths or 3.2 body widths away from the position directly above the actuator magnet) at any point during the run were discarded.

Rough terrains, like that used for testing in [5], were 3D-printed on a UPrint SE Plus using ABS (Stratasys ABS-P430 XL Model). The 5 mm square blocks are scaled to have a side length of 25% the body length of the robot. The heights of the blocks were randomly generated from a normal distribution using a MATLAB script(Appendix A). Two terrains were printed with differing upper bounds on the

normal distributions, defined as 3 standard deviations above the mean. The first used an upper bound defined as two times the robot hip height (2X, 11.28 mm) and the second terrain used an upper bound defined as three times the robot hip height (3X, 16.92 mm). The lower bound in both terrains was 0 mm. The mean heights of the 2X and 3X terrains result in torque decreases of 19% and 31% respectively. While this decreases the torque to levels lower than preferred, it still provides a lower bound on locomotion efficacy. Figure 2.6 shows the generated terrain. The terrains were placed on top of the acrylic sheet and the quadrupeds were tracked traversing the terrain.

2.4 Results

2.4.1 Gait Characteristics

The planar and angular motion with respect to time of the different gaits on a flat acrylic surface can be seen in Figure 2.7. These plots represent a single measurement point (the geometric center of mass) for each gait and are typical of all measurements taken for seven trials each of a single robot for each gait. In these plots, the driving frequency is 4 Hz. A driving frequency approximately one third the calculated step-out frequency was chosen to ensure consistent actuation, ensuring the legs remained synchronized to the actuator magnet. The slope of the longitudinal plots indicate robot speed and the lateral plot provides an indication of horizontal drift (generally less than 1 cm over the course of the study). Pronking and trotting were the fastest gaits at this drive frequency.

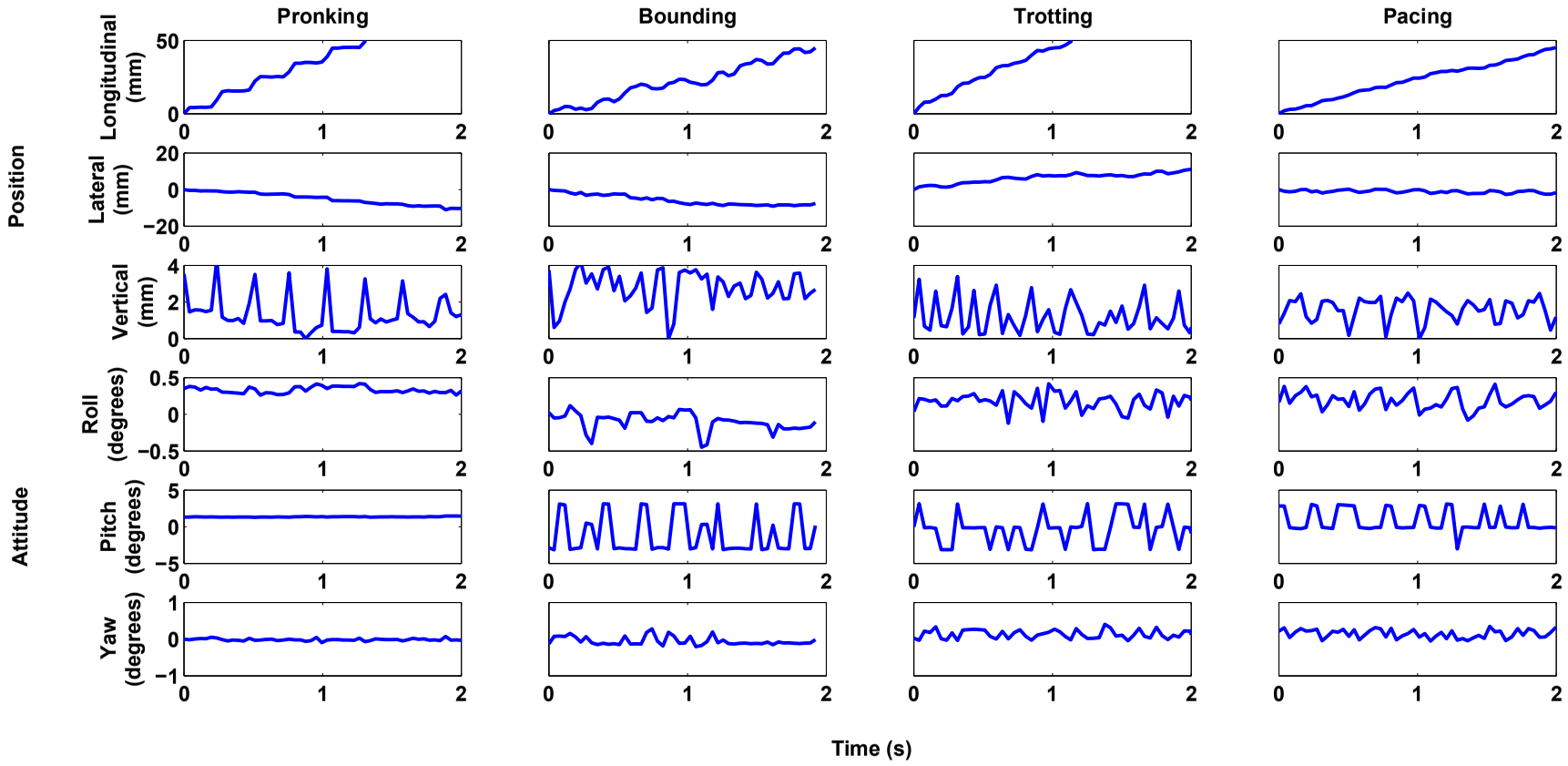

Figure 2.7: Motion data from the four gaits on flat terrain, from left to right: pronking, bounding, trotting, pacing, and from top to bottom: longitudinal, lateral, and vertical positions, and robot roll, pitch, and yaw.

The first column in Figure 2.7 shows the planar and angular motion of the pronking gait. It can be seen that the quadruped moves forward and pauses and shows small hops in the vertical displacement. Pauses are due to the time all legs are in contact with the ground before the robot is launched into the air. The pronking gait has minimal roll, pitch, and yaw since all of the legs are actuated in sync, not causing significant rotations.

The bounding gait, the second column of Figure 2.7, can be characterized by the oscillation in the pitch angle. This is due to the 180° phase difference between the front and back legs. This is also reflected in the vertical motion, showing a similar oscillatory behavior to the pitching of the robot.

The trotting gait has the pairs of diagonal legs in sync. Every step of the quadruped has rotation about a diagonal axis across the body, which can be seen in both the pitch and roll oscillations in third column of Figure 2.7.

The pacing gait configuration causes a more consistent oscillation frequency in roll than other gaits, as seen in the last column of Figure 2.7. The pacing gait can also be characterized by the oscillatory behavior of the yaw of the robot, attributed to the left and right sides of the robot actuated out of phase relative to each other.

2.4.2 Bounding subset

Each rear leg configuration was tested at 4 Hz on flat terrain (acrylic sheet), and the average speed and standard deviation over at least seven trials were calculated. The maximum average velocity was 45.5 mm/s (2.28 body lengths per second) at a

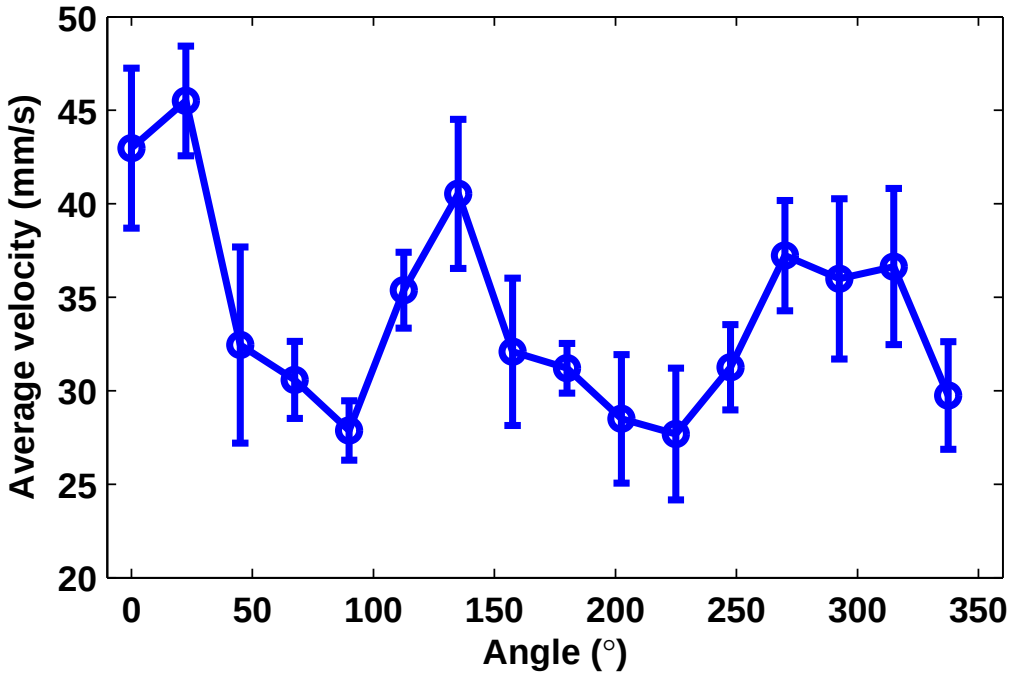

Figure 2.8: Average speed and standard deviation over seven trials of different back leg offset angles from 0° to 337.5° in 22.5° increments. The driving speed is constant at 4 Hz.

phase offset of 22.5°. Figure 2.8 shows the average velocity and standard deviation over seven trials of the different back angle configurations. One robot for each offset value from 0° to 67.5°, four robots total, were tested.

The two largest peaks occur at both 0° and 22.5°. At these angles, the legs of the quadruped are all contacting the ground before the body begins to lift off the ground, contributing to a flight phase in locomotion. A third peak occurs at 135°. In this configuration, the back legs contact the ground just as the front legs are no longer contacting the ground. The body is pitched upward as the back legs contact the ground, providing additional force propelling the robot forward.

2.4.3 Frequency Testing

Each gait configuration was tested with driving voltage applied to the motor between 1.0 V to 4.2 V in 0.2 V increments, corresponding to driving frequencies between 2.0 Hz and 12.4 Hz in evenly spaced increments. The calculated step-out frequency of 12.8 Hz was validated as the robot demonstrated chaotic motion at 4.4 V (corresponding to 13 Hz). Average speeds over at least seven trials were found for each frequency tested, along with standard deviations for each. A comparison of the gaits is shown in Figure 2.9, showing the average and standard deviation of the speed performance over seven trials for each driving frequency with one robot per gait.

The maximum average speed of the quadruped was measured at 77.6 mm/s (3.88 body lengths per second) at 10.5 Hz with the pronking gait configuration. At low frequencies (<5 Hz), the trotting gait has a higher average velocity. However, the pronking gait outperformed the other gaits at higher frequencies. The error bars for pronking and trotting increase at higher frequencies, from approximately 3.16 mm/s at 5.96 Hz to 18.6 mm/s at 12.4. Hz for pronking and from approximately 1.39 mm/s at 5.96 Hz to 8.80 mm/s at 12.4. Hz for trotting These two gaits have a flight phase, making them more dynamic and varied at higher frequencies. Figure 2.10 shows the pronking gait actuated at 10 Hz. Frame (c) shows the flight phase of the pronking gait.

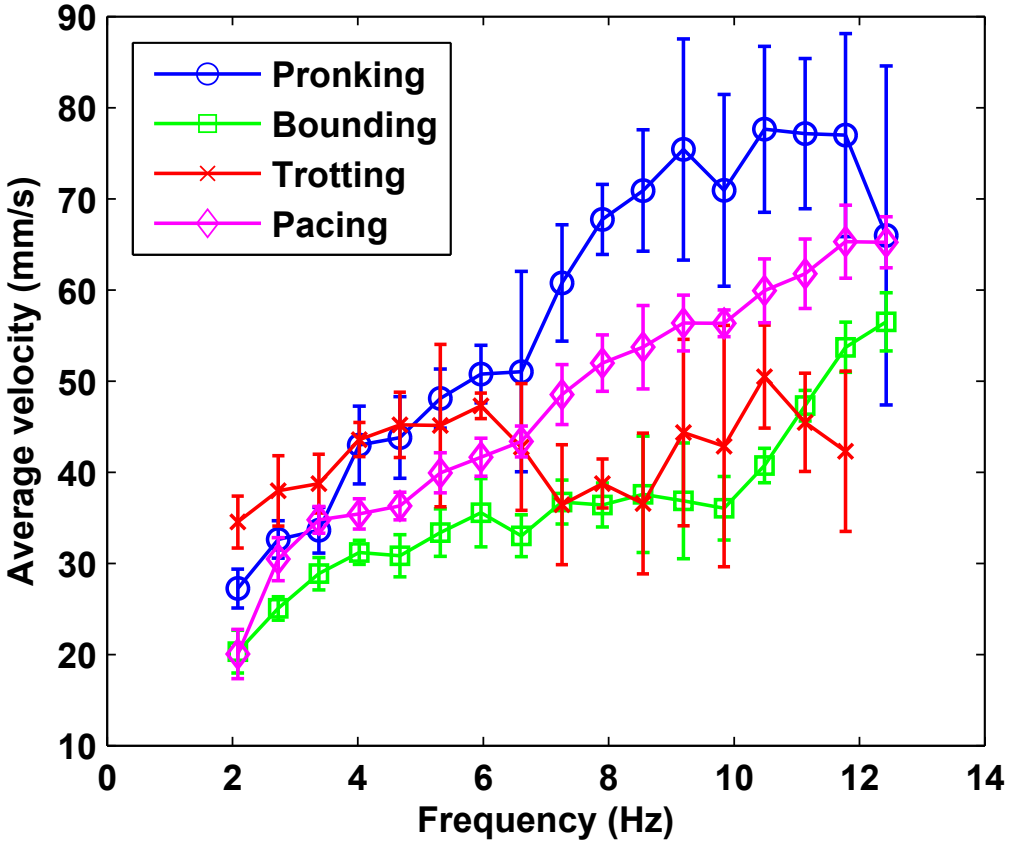

Figure 2.9: Average speed and standard deviation over seven trials for one robot for each of the different gait configurations of the quadruped. Trials were conducted from 2.0 Hz to 12.4 Hz.

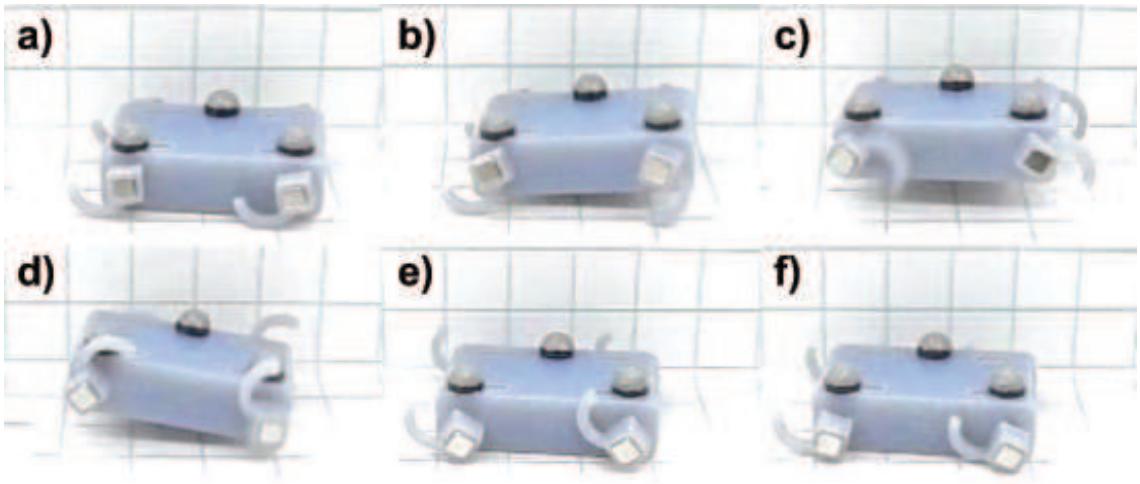

Figure 2.10: Video stills of robot pronking, actuated at 10 Hz.

2.4.4 Rough Terrain

The quadrupeds were tested over two random rough terrains. The terrains, 2X and 3X, refer to the upper bounds of the normal distribution used to make the terrains, as described in Section 2.3. A 1X terrain was not tested, as that distribution did not pose a challenge to the robots. The quadrupeds were tested traversing the terrains at a constant frequency of 6 Hz. The slightly increased speed at 6 Hz helped the robots move over the terrain more consistently than the 4 Hz frequency used in previous trials on flat terrain. Table 2.1 shows the average percent of terrain covered, referenced to the horizontal length of the terrain, independent of path taken, over at least ten trials per terrain (over 20 trials total), along with standard deviations for each. One robot per gait was tested. For each trial, the quadruped was placed at a different starting location, the starting location was not repeated for consecutive tests. When the robots were stuck, no longer advancing forward, the trial was ended. On both terrains, the pronking gait was able to cover the most terrain. In addition,

robots were able to traverse more terrain before getting stuck in either a 'hole' in the terrain or behind a large step height on the 2X versus 3X terrain for all gaits.

Figure 2.11 plots the percentage of robots successfully traversing terrain against the path roughness of the actual path traversed by the robot. This plot is roughly a measurement of the probability of success that a feed-forward robot, similar to the one presented in this work, could traverse a path of that measured roughness. The roughness is calculated as the root mean square (RMS) roughness of the path that the robot 'found' over the terrain (vertical displacement from tracking data used to determine block heights). A larger RMS roughness value corresponds to more variations in the terrain but not necessarily to large step heights from one block to another. Less than half of the robots using the pronking gait can cross terrain with an RMS roughness equivalent to a single step of hip height (4 mm), but almost all of the bounding and trotting robots were successful at this same RMS roughness. There is a less than 10% probability that robots could traverse a path with an RMS roughness of 8.3 mm.

Since the robots are not controlled, they rely on mechanically 'finding' a path that they can cross. In Table 2.1, the pronking gait traversed the longest paths, but when compared to Figure 2.11, it becomes clear that the pronking gait was only successful over terrain with fewer height variations. Often failure occurs when the robots encounter a large step (Figure 2.12) or encounter a 'hole' in the terrain, where the legs get stuck. Comparing the results from Figure 2.11 and the velocity performance in Figure 2.9 show a trade-off with speed performance and the ability

Table 2.1: Percent of rough terrain traversed by quadruped using the different gaits. 2X and 3X refer to the upper bound of the normal distribution used to make the terrain.

	$2X$	$3X$
Pronking	$39.67 \pm 15.64\%$	$22.96 \pm 5.22\%$
Bounding	$18.14 \pm 13.23\%$	$16.46 \pm 7.51\%$
Trotting	$25.60 \pm 14.01\%$	$8.83 \pm 7.95\%$
Pacing	$31.97 \pm 15.03\%$	$5.12 \pm 4.45\%$

to traverse rough terrain. While the pronking gait demonstrates high speed on flat terrain, over rough terrain, a different gait would be more useful.

In addition, the robots were tested over single steps of varying heights formed by stacking 0.8 mm thick layers of Delrin plastic sheet. The robots were consistently able to handle step heights of 4 mm (71% of hip height). This is similar to single step data demonstrated in RHex [24].

2.5 Conclusions

The method presented in this work was used to explore different quadrupedal gaits in a <2 g microrobot. This method allows for known torque and force to be applied to the robot. Both the torque and force can be easily increased by moving the robot closer to the actuating magnet, without having to replace the embedded magnets.

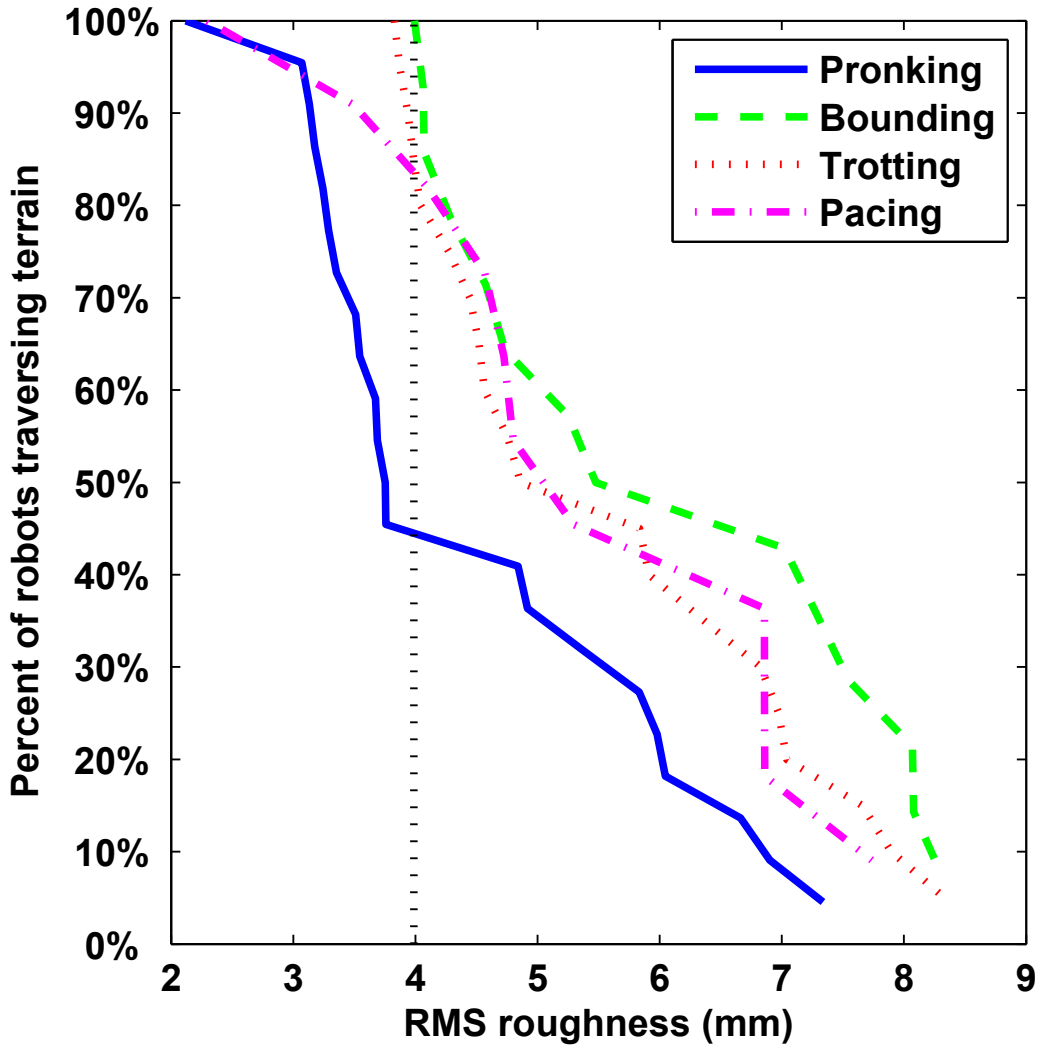

Figure 2.11: The percentage of robots accomplishing traversing a rough terrain. The vertical dotted line corresponds to the RMS roughness value of a step height at hip height.

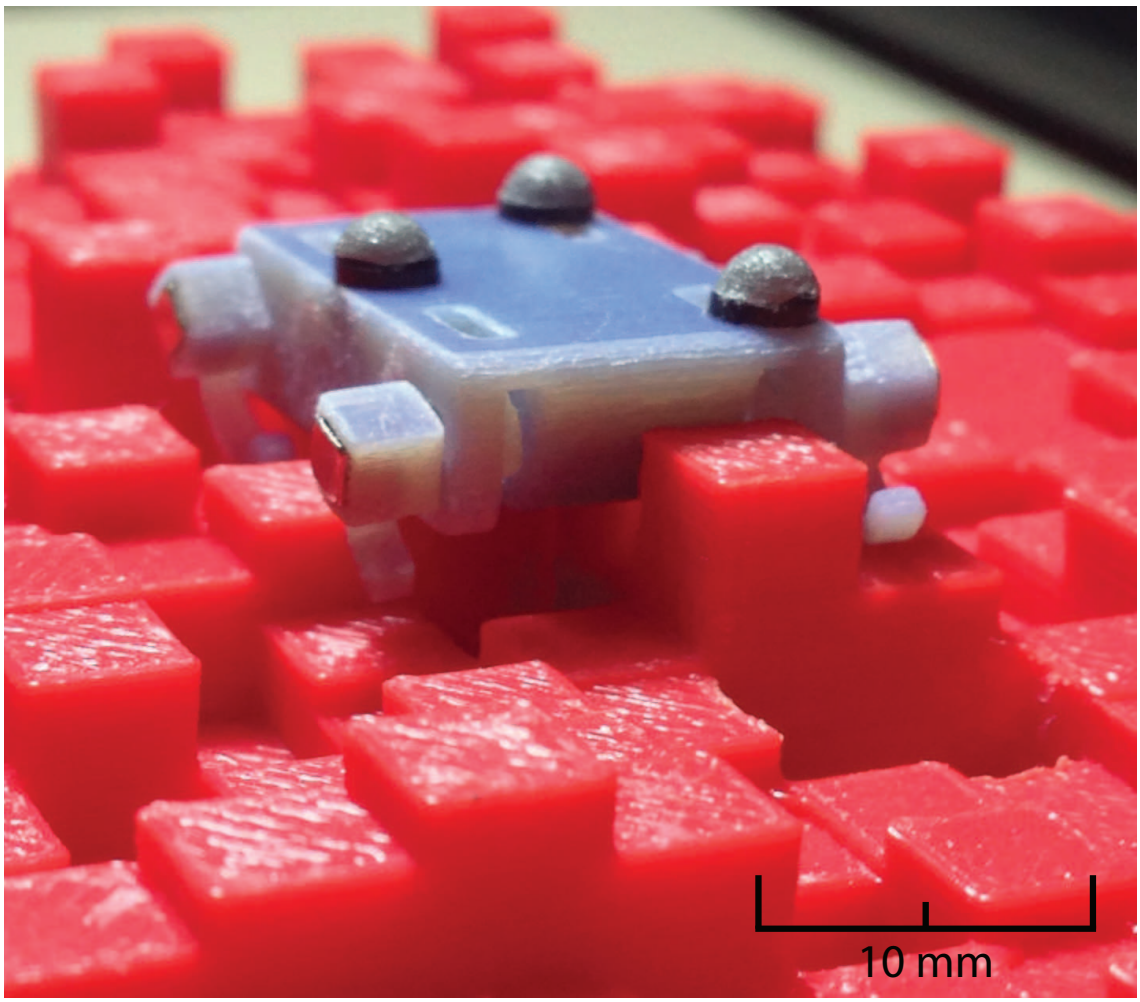

Figure 2.12: A quadrupedal robot failing to cross rough terrain due to high step height. The step height from the block that the robots leg rests on to the block impeding the robots path is 4.7 mm.

However, due to the limitations of using permanent magnets as an actuation method, discussed in Section 2.1, the robots were only actuated up to 12.4 Hz.

The gaits of the quadrupedal robots were easily changed by changing the orientation of the embedded permanent magnets. The robots were then tested over a variety of speeds and over multiple terrains. At 4 Hz, a 22.5° phase offset in the back legs resulted in a maximum average velocity of 45.5 mm/s. On flat terrain, the pronking gait outperformed the other gaits at frequencies above 5 Hz, reaching average speeds up to 77.63 mm/s (3.88 body lengths per second). On rough terrain, the pronking gait was also able to cover more terrain than the other gaits on both the 2X and 3X terrain. However, when the roughness of the path taken was examined, it was found that the pronking gait experienced less rough paths. When compared to the other gaits, more trials using the bounding gait successfully traversed terrain with higher variations in roughness.

The locomotion capabilities of this robot can be improved by adding compliance to both the body and legs, better mimicking insects. This study demonstrated that the pronking gait generally had the lowest cost of transport (COT), a metric that quantifies the energy efficiency of locomoting, compared to the other gaits. However, pronking is not a gait seen in insects.

This work presents a new method to study legged locomotion at small scales. Combining magnetic actuation with 3D printed legged robots allows for both simple testing and rapid design iterations. Force and torque on the robot magnets can be calculated, informing actuation needs for future autonomous robot design. The method is limited by a single control signal provided by the magnetic field of an

actuator magnet. When a permanent magnet is used to generate the magnetic field, drive frequency is also limited by the step-out frequency, proportional to the torque and separation distance between actuator and robot magnets.

This method allows for numerous future studies of locomotion in addition to gait. For example, leg compliance can be modified through the use of multi-material 3D printers to study the effect of leg compliance on locomotion success, and locomotion efficiency (cost of transport) can be studied by studying the torque required for successful locomotion. Use of a multi-axis robot to position the actuator magnet can allow for locomotion through even more complex terrains and an optimized feedback controller can provide more accurate positioning at higher speeds for improved torque estimates. Study of locomotion at even smaller robot scales is limited by the availability of magnetic material and manufacturing technique.

Chapter 3

Compliance and damping in legged, small-scale robots

Material and morphology play an important role in the control of biological systems. Specifically, in the context of legged locomotion, the interaction between the leg and ground, coupled with the mechanical properties of the leg, form a base set of behaviors promoting stable locomotion patterns [65]. Biological systems, in particular, take advantage of viscoelastic materials for energy removal to enable stable, high-speed locomotion. Soft tissue is not only compliant, but provides damping through viscoelastic effects, promoting dynamic stability [66]. In flapping wing flight, the steering muscle of a blowfly removes energy to enable stability [67]. In legged locomotion, the morphology as well as the material of the guinea fowl leg enable stability even when subject to impulse [68]. In cockroaches, muscles within the same group behave alternately as motor and brake [69], actively damping out energy to enable running at top speeds [4]. Even the mechanical properties of the overall musculoskeletal system of the cockroach enable recovery [70] and the cockroach relies on both energy storage and dissipation for effective locomotion [71].

In robotics, exploiting the benefits of both material and morphology can boost the performance of the robotic system without added cost to a controller. By outsourcing control to the robot's mechanics, complex maneuvers can be enabled with minimal active control. This concept is best highlighted through the use of com-

putational design to simulate tensegrity structure robots that couple the dynamics of locomotion with the mechanics, enabling locomotion with minimal active control [72]. The morphology allows a more robust design-space to embed control in a robot. This can also be illustrated for legged robots like RHex [24] (7 kg). Simulations in [73] reduced the mechanisms to a SLIP model, and examined the effect of varying the leg compliance on both stability and speed. This work exceptionally highlights the utility of simple locomotion model as a guide for design, showing that varying the compliance of the leg produced faster and more stable robots than just changing a control system. In an experimental study, tunable compliant legs were incorporated on a RHex platform in [74], demonstrating the effectiveness of changing leg stiffness to run efficiently and stably. iSprawl [46] (300 g), was designed with compliance and damping in the legs and joints, serving as mechanical preflexes, to enable rapid, stable running at top speeds of 15 body lengths per second with only a feed-forward control.

Building on the work presented in Chapter 2 and incorporating a modular design, the material choice is expanded for robot legs. In this chapter, while most of the components were 3D printed, robot legs were made in other processes, such as molding. By choosing materials with different stiffnesses and internal damping values, stable and rapid locomotion can be made possible with minimal feed-forward control, and no feedback control. This chapter characterizes different leg materials and uses both experimental and simulation insights to determine the role of passive energy storage and removal for small-scale legged robots. The insights gained from the experimental results and complementary simulations provide a map for

the design of future small-scale robots, exploiting passive dynamic stability through material choice of the leg.

3.1 Leg properties

3.1.1 Experimental setup

Four different polymers were explored for the legs of the quadrupedal robots. The C-shaped geometry was fixed for each leg and measured 5.64 mmlong hip-to-toe. Legs were cast from three polymers, MRTV (MRTV9, Insulcast), PDMS (Sylgard 184, Dow Corning), and silicone foam (Soma Foama, Smooth-On), and 3D printed (TangoBlack+, Stratasys).The PDMS and MRTV were both mixed in a 10:1 base to curing agent ratio, as specified by the manufacturers. The polymers were poured into a $\frac{1}{16}$" thick acrylic mold that was laser cut on a VLS3.50 Desktop 50W CO_2 laser cutter from Universal Laser Systems. The polymer in the mold is placed in a vacuum chamber to remove any bubbles to prevent voids. The MRTV and PDMS molded legs were cured at 100 °C on a hotplate. After curing, the molds were planarized with a razor blade, cutting away excess polymer on the top of the molds. The silicone foam was mixed in a 1:1 ratio and poured into the acrylic mold. The polymer was cured at room temperature overnight; excess polymer was cut away from the top of the mold using a razor blade. The TangoBlack+ legs were 3D printed on a Stratasys Objet500 Connex3. Support material surrounding the leg was removed manually, peeling away support material from model material, and

then chemically using a 2% solution of NaOH heated to 20 °C and agitated with a magnetic stir bar.

The viscoelastic properties of the legs were measured through dynamic oscillations from a dual-mode muscle lever system, 300B Aurora Scientific, similar to the experiments in [71]. The microrobot leg is suspended above the lever arm with a #3 insect pin (0.508 mm diameter) attached to the foot of the microrobot leg. The pin is bonded to the servo arm using a mounting adhesive, Crystal Bond 509. Each leg is compressed 0.5 mm (just under 10% of leg length) sinusoidally at frequencies from 0.1 Hz to 50 Hz, swept logarithmically. The corresponding force and displacement is measured using a DAQ (NI USB-6361, National Instruments) sampling at 100,000 samples/sec. Figure 3.1.1 shows a schematic of the test setup.

3.2 Results

3.2.1 Mechanical impedance and phase shift

The mechanical impedance is the ratio of greatest peak-to-peak amplitude of a sinusoidally varying force to the greatest magnitude of a displacement [75]. This metric captures both a static component, related to displacement, and dynamic component, related to the velocity and acceleration. The mechanical impedance is defined as

$$Z = \frac{F_{max} - F_{min}}{x_{max} - x_{min}} \tag{3.1}$$

where F is the force induced and x is the displacement measured per oscillation.

Figure 3.2 shows the measured mechanical impedance of the different leg types,

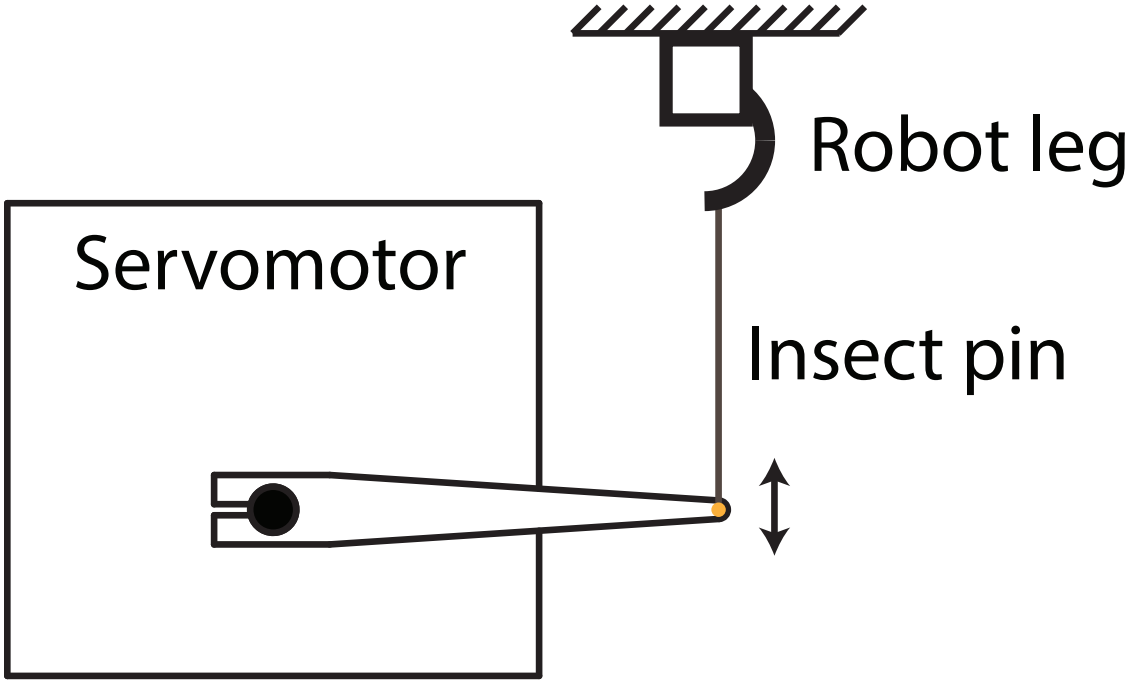

Figure 3.1: A schematic of the experimental setup. Robot legs were compressed sinusoidally with the servomotor, which reads back the position and force exerted by the leg on the servo motor arm.

excluding the rigid legs. Trendlines from [71] for similarly displaced cockroach legs are included. In measuring the mechanical properties of the cockroach leg, the authors in [71] measured properties for two different leg preparations: 1) a fixed coxa preparation in which the joint attaching the leg to the body was fixed, and 2) the free coxa preparation in which that joint could freely rotate. In both the work presented here, as well as in [71], the leg is compressed at frequencies faster than the maximum sustainable stride frequency (13 Hz in [52] and <25 Hz in the work here).

The silicone foam shows a similar mechanical impedance to the free coxa preparation of the cockroach leg, while MRTV shows a similar mechanical impedance to the fixed coxa cockroach leg preparation. The mechanical impedance of the cast polymers, MRTV, PDMS, and Soma Foama, are relatively constant over the frequency range. However, mechanical impedance the 3D printed polymer, TangoBlack+, varies over an order of magnitude in the frequency range. After approximately 10 Hz, the TangoBlack+ leg has a mechanical impedance over 100 mN/mm, essentially acting as a rigid leg for robots with a body mass less than 1 g. The polymer legs have mechanical impedance values that both span the range of biologically relevant values for a similarly sized cockroach [71] and move beyond these values.

The viscoelastic property of the leg types is captured by the phase shift, expressed as $\tan\delta$, and is defined as [76]

$$2\pi \tan\delta = \frac{E_{load} - E_{unload}}{E_{load}} \tag{3.2}$$

where E_{load} and E_{unload} are the loading and unloading energy of the leg, calculated

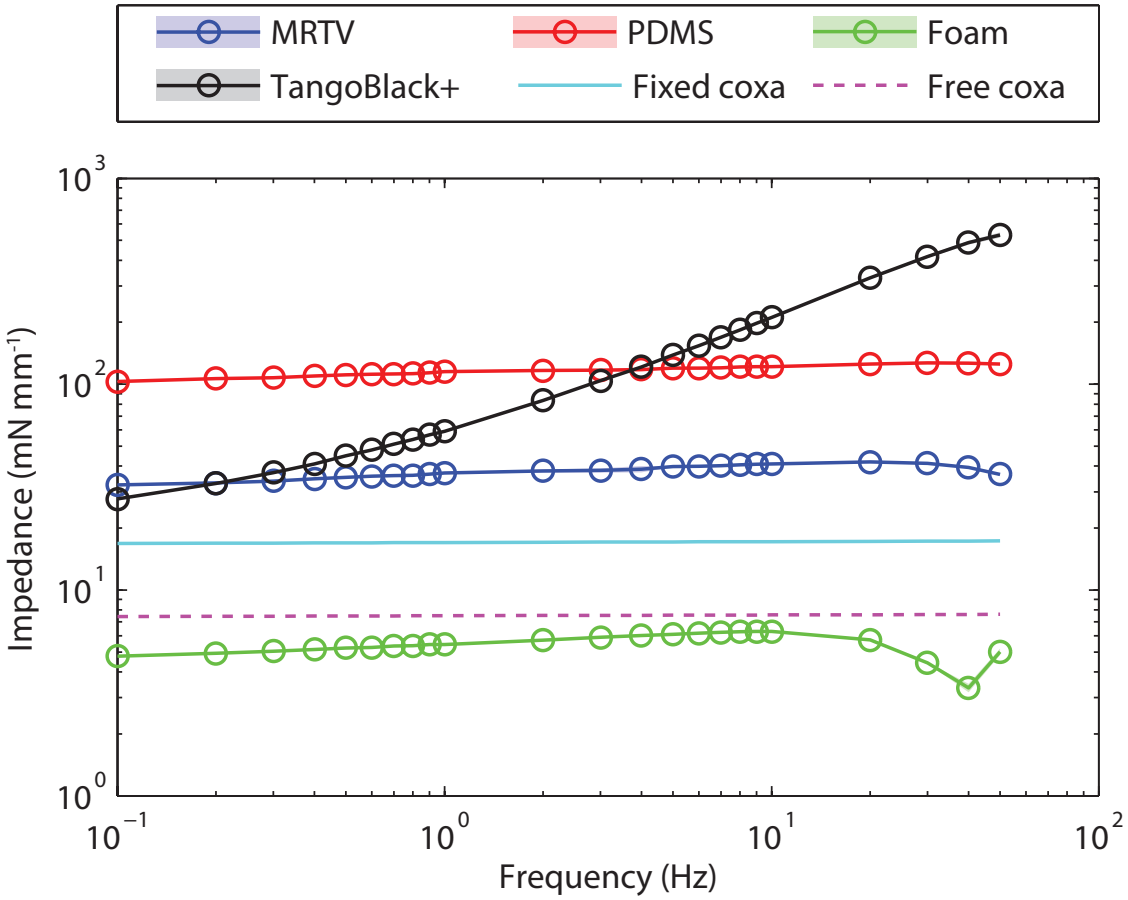

Figure 3.2: Mechanical impedance of different leg types (MRTV, PDMS, Soma Foama, and TangoBlack+) oscillated sinusoidally from 0.1 Hz to 50 Hz and displaced 0.5 mm. The fixed and free coxa trendlines are from [71] with cockroach legs displaced and oscillated similarly.

from integrating the force-displacement curves. Figure 3.3 shows the calculated $\tan\delta$ values for the polymer legs and trendlines from [71]. The MRTV and PDMS legs are well matched to the free and fixed coxa preparations, respectively. The silicone foam legs become more damped at the high end of the frequency range, most likely attributed to a nonlinear behavior of foams. The TangoBlack+ legs show an increasing phase shift as frequency increases, consistent with the trend of mechanical impedance. Again, the polymer legs show similar viscoelastic properties to a similarly sized insect in [71].

3.2.2 Spring and damping constants

The spring and damping constant of a massless, parallel spring-damper model were obtained through a least squares regression to the experimentally measured force and displacement. The parallel spring-damper model is described mathematically as,

$$F = kx + c\dot{x} \tag{3.3}$$

with F and x as the measured force and displacement, while $\dot{x}$ is calculated numerically (the finite difference of the measured displacement data, taken by the forward difference method, divided by the sampling period). Using a least squares regression, k and c were fit to the model. Figures 3.4 and 3.5 show the resulting spring constant (k) and damper (c) values of the polymer legs and similarly fit spring constant and damper values for a cockroach leg [71]. The PDMS and MRTV spring constants are relatively constant over the frequency range tested. However, their

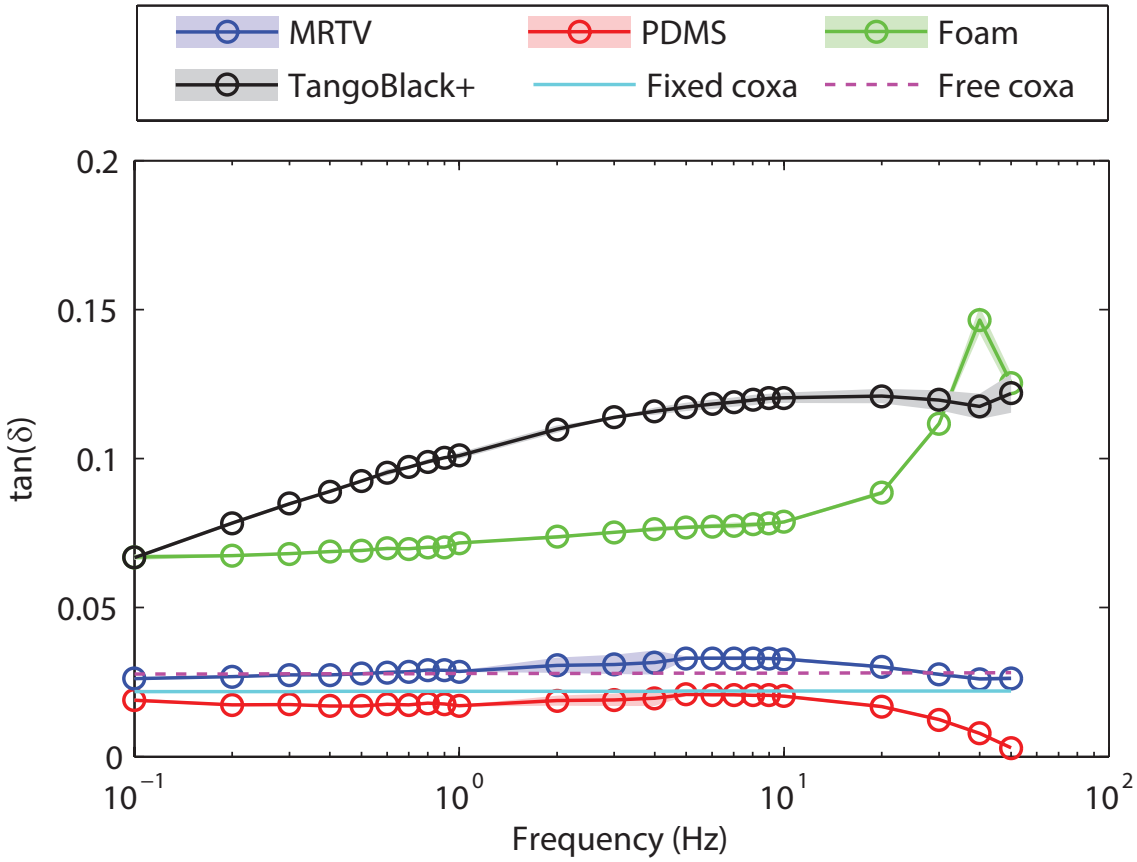

Figure 3.3: Phase shift of different leg types (MRTV, PDMS, Soma Foama, and TangoBlack+) oscillated sinusoidally from 0.1 Hz to 50 Hz and displaced 0.5 mm. The fixed and free coxa trendlines are from [71] with cockroach legs displaced and oscillated similarly.

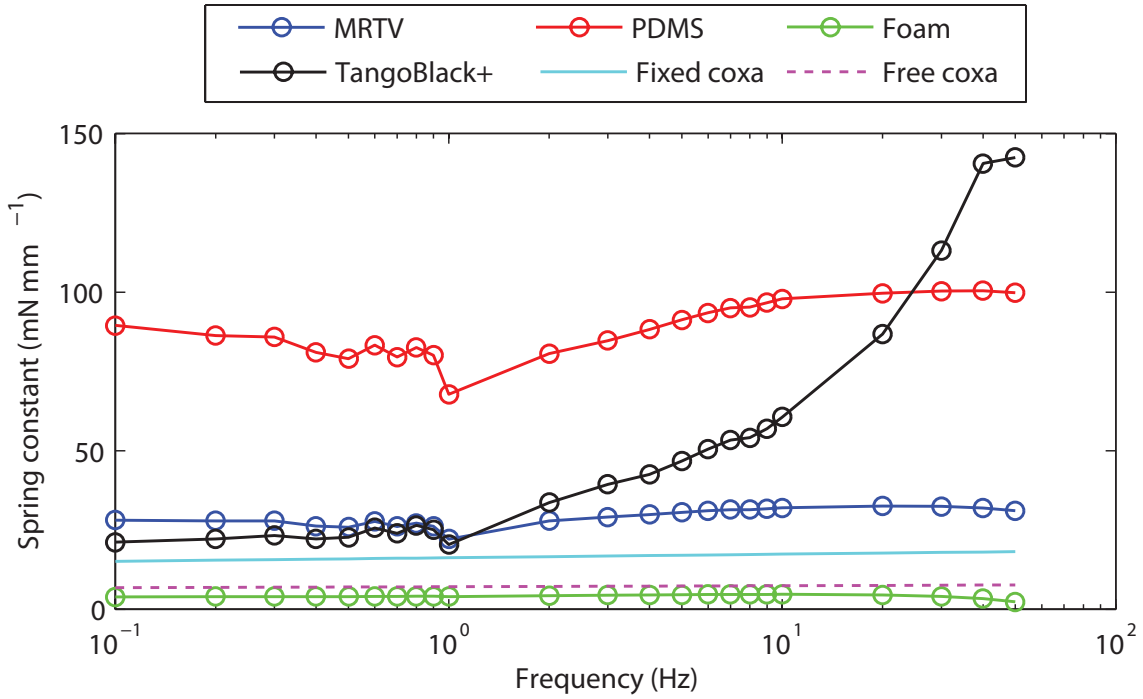

Figure 3.4: Least squares fit of the spring constant of different leg types (MRTV, PDMS, Soma Foama, and TangoBlack+) oscillated sinusoidally from 0.1 Hz to 50 Hz and displaced 0.5 mm. The fixed and free coxa trendlines are from [71] with cockroach legs displaced and oscillated similarly.

respective damping values decrease over two orders of magnitude with increasing frequency, showing a less damped system with increased actuation frequency. The TangoBlack+ spring constant increases almost an order of magnitude over the frequency range with a damping ratio that only drops one order of magnitude over the frequency range. The silicone foam shows the lowest spring constant with a damping constant similar to the MRTV and PDMS legs.

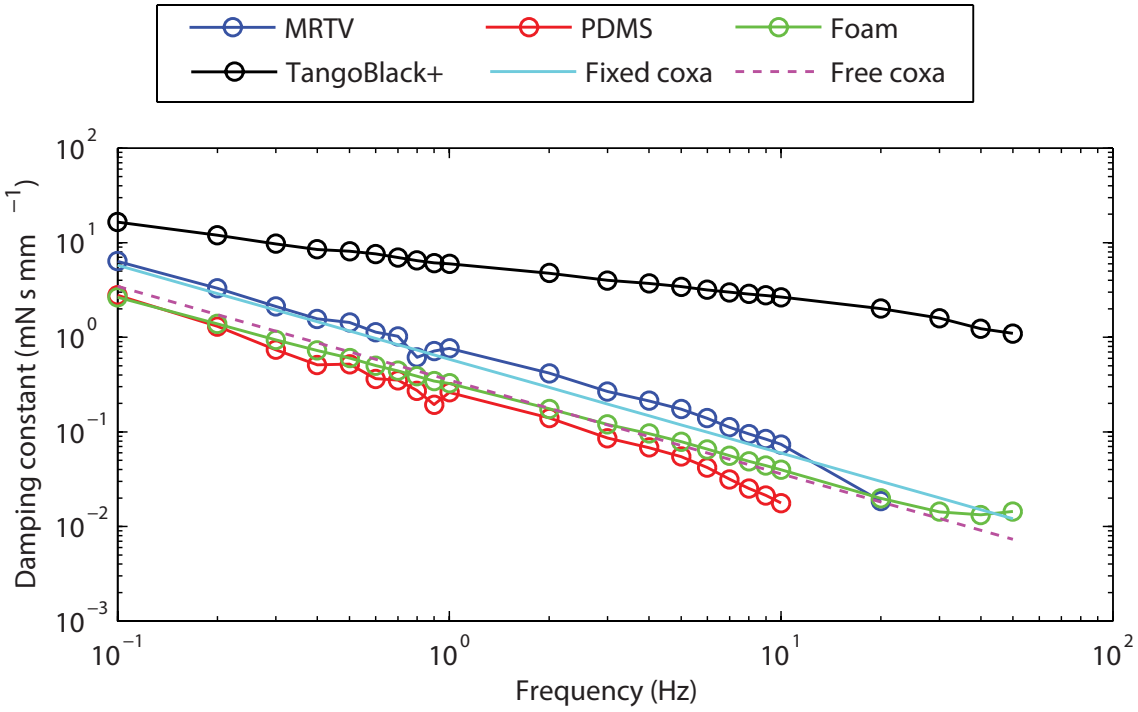

Figure 3.5: Least squares fit of the damping constant of different leg types (MRTV, PDMS, Soma Foama, and TangoBlack+) oscillated sinusoidally from 0.1 Hz to 50 Hz and displaced 0.5 mm. The fixed and free coxa trendlines are from [71] with cockroach legs displaced and oscillated similarly.

3.3 Robot fabrication

Figure 3.6 shows a diagram of the assembly of the robots. First, the body and the hip joints, without legs, were printed on an Objet 30 Pro 3D printer using a rigid opaque photopolymer (VeroBlue RGD840). After printing, the bulk of the support material is removed mechanically with dental tools, and then chemically in a 2% solution of NaOH heated to 20 °C and agitated with a magnetic stir bar. To assemble the robot, 2 mm cube magnets (SuperMagnetMan C0020) were inserted into hip joints (Figure 3.6c). Polymer legs were cast in a laser cut mold (Figure 3.6d) and the TangoBlack+ legs were printed on the Connex3. Finally, the legs were then attached to the hip joints of the quadrupeds with cyanoacrylate, Loctite 401, as shown in (Figure 3.6e). A set of rigid legs was also printed on the Connex3 with a of 125 μm thick band of TangoBlack+ the on back of the legs to provide a frictional ground contact similar to the other polymer legs without significantly changing the stiffness of the rigid legs.

3.4 Experimental setup

The quadrupeds were actuated and tracked as described in Chapter 2. In addition to the rigid body data from the OptiTrack, the locomotion of the quadrupeds in the sagittal plane was recorded with high speed video (FASTCAM Mini UX100) at 1,000 frames per second.

In this set of experiments, the magnets were the same as described in Chapter 2, however, the distance between the robot magnetics and actuator magnet was

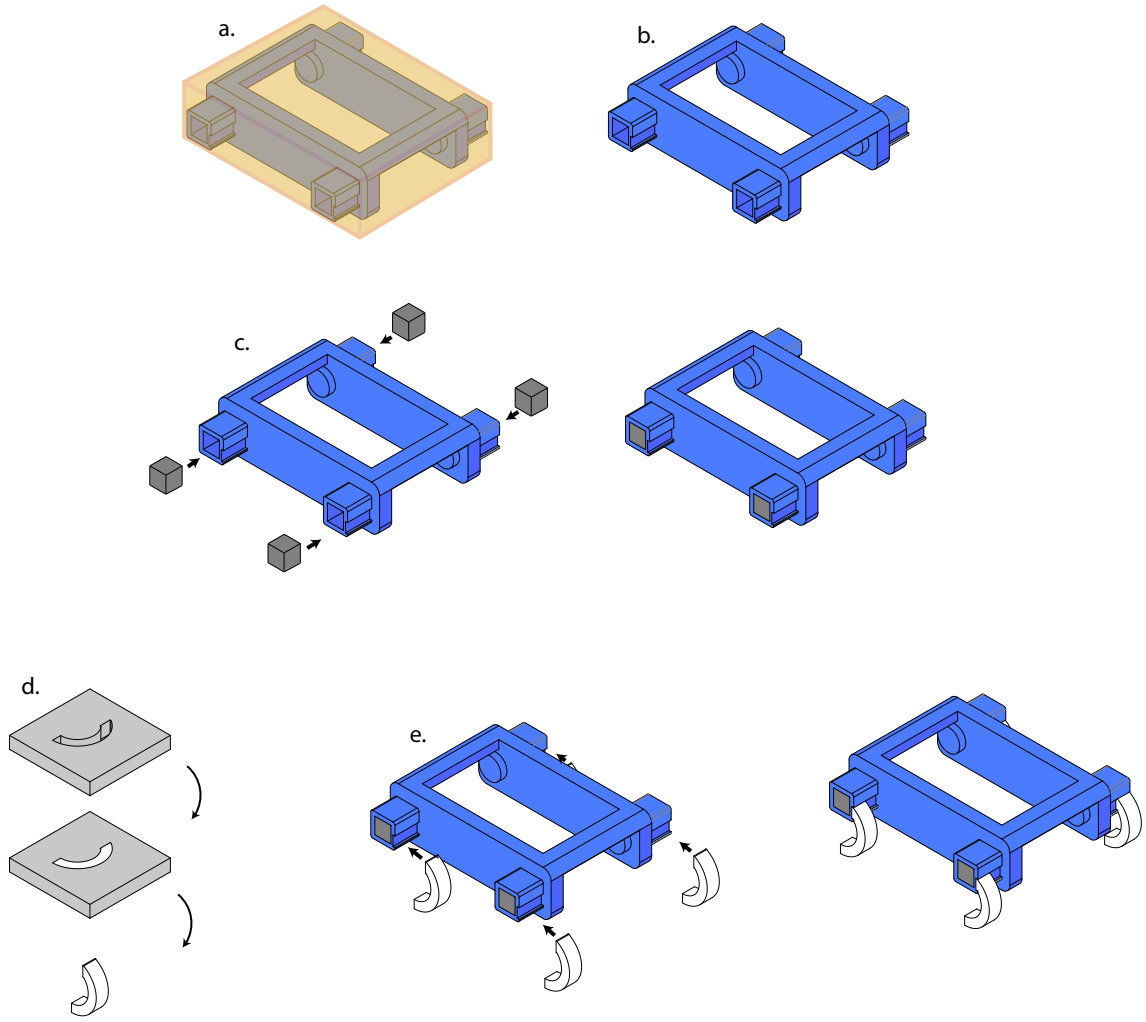

Figure 3.6: Exploded view of the modular quadruped solid model assembly. The compliant legs can be made in processes other than 3D printing and then attached to the hip

increased to 100 mm. At this distance, the magnetic field from the actuator magnet was calculated as 2.12 mT, resulting in a calculated maximum applied torque of 27.7 mN $\cdot$ mm and a calculated force of 0.83 mN to each robot magnet, corresponding to a total payload of 0.34 g(45% of the bodyweight). The robots were actuated from 1.3 Hz to 28 Hz in equal increments of 1.8 Hz, corresponding to motor voltages from 1.0 V to 8.5 V in 0.5 V increments.

3.5 Experimental results

3.5.1 Velocity

In addition to looking at the locomotion performance of the different leg types, the gaits were changed as well, resulting in 20 different configurations of gait type and leg type. Figure 3.7 shows the average forward velocity of the different leg and gait configurations of the robots over three trials for a single robot of each leg type on flat terrain. Generally, the robots with MRTV legs outperformed the other robots when compared using the same gait. The robot with MRTV legs achieved top speeds of 233 mm/s (11.7 body lengths/s) with a trotting gait. It is notable that the trends for the robots with silicone foam legs, regardless of gait, were generally linear. The stiffness of the silicone foam legs is so low that the legs are compressed by the robot, essentially forming tires around the hip joint of the robot.

The bounding and pacing gaits (top row) show similar performance across all leg types. Largely, these gaits are dominated by the dynamics of the body either pitching, in the bounding gait, or rolling, in the pacing gait. With both of these

gaits, the body impacts the ground and, in effect, 'resets' the dynamics. The collision of the body with the ground dissipates energy, negating any elastic energy stored in the legs. The leg choice for these gaits is seemingly irrelevant. However, this does mean that a gram-scale robot could be designed with almost any material for the leg and would run predictably with these gaits. In this case, the choice of gait can override benefits or detriments that a compliant leg might have on the robot body dynamics.

However, leg-dominated gaits, such as pronking and trotting, shown in the bottom row, offer benefits when choosing differing leg materials. In pronking, the more elastic legs (MRTV and PDMS) typically outperform the other leg types up to 15 Hz. These legs compress under the weight of the robot and upon release, add additional energy towards the aerial phase moving the robot forward. The rigid and TangoBlack+ legs perform similarly in this gait. The highly viscoelastic properties, characterized by the increasing mechanical impedance and phase shift with frequency, of the TangoBlack+ legs most likely act rigid under this gait type with the driving frequencies tested. It is possible that a lower frequency actuation might distinguish the performance of these two leg types. However, this work builds towards highly dynamic robots, so a lower driving frequency is undesirable. In the trotting gait, again the more elastic legs outperform the other leg types up to 17 Hz. In this gait, two legs are on the ground at any time, therefore, the robot can come down from an aerial phase and load the legs elastically to propel the next steps. Typically, MRTV outperforms other leg types in these leg-dominated gaits.

The choice of leg material influences the leg dynamics, clearly affecting the

robot body dynamics in these leg-dominated gaits. For example, stiffer legs can cause the robot to undergo large vertical displacements, resulting in missed steps in which a leg completes a rotation without contacting the ground. These missed steps ultimately result in a drop in performance, characterized by a reduction in the average forward velocity. The influence of leg dynamics on the body dynamics can also be seen from the effect of damping and compliance between the MRTV legs and PDMS legs. The PDMS legs reached a peak performance at a lower frequency than the MRTV legs comparing across leg-focused gaits. Looking at high speed video of the robots running, the MRTV leg promoted a more inelastic contact with the ground, as compared to the PDMS legs, resulting in legs delaying the release of the stored elastic energy until the center of mass is ahead of the ground contact point.

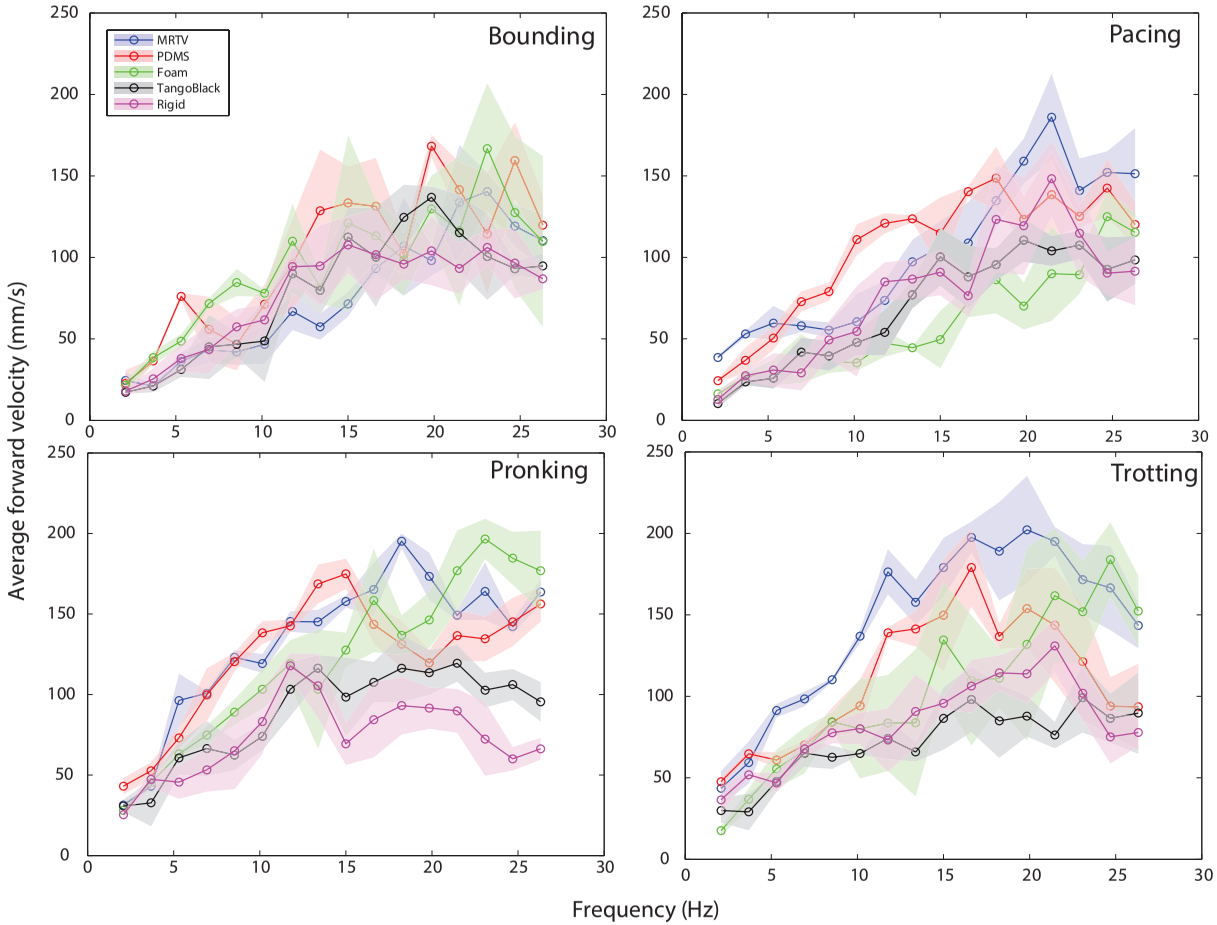

Figure 3.7: Average forward velocity of the different robot leg and gait configurations. The circle markers represent the average over 3 trials, while the shaded area represented the standard deviation.

3.5.2 Energy phasing

The relative phasing of the horizontal kinetic energy ($\frac{1}{2}m\dot{x}^2$) and gravitational potential energy (mgh) give insight into the dynamics of locomotion, and ultimately the model best suited to describe the locomotion. In general, when the peaks of the kinetic energy and gravitational energy are co-located, corresponding to a phase shift of 0°, the locomotion is described as running, generally with a spring-loaded inverted pendulum (SLIP) model [6]. When the peak of the kinetic energy occurs with a trough of the gravitational potential energy, or the troughs of the kinetic energy with the peaks of the gravitational potential energy, the phase shift is 180° out of phase and indicative of inverted pendulum (IP) walking [17]. Figure 3.8 shows the phase shift, calculated from the temporal difference of the peaks of the energy profiles, for each gait type and leg type. The solid lines represent the average phase shift, averaged over more than 10 stride cycles of each of the three trials for a single robot, while the shaded area represents the standard deviation.

Figure 3.8(top left) shows the phase shift for the bounding gaits. An analysis of covariance compares the linear regressions of the phase shift against frequency across the leg types. For the bounding gait, the ANCOVA shows no statistically significant difference among the slopes of the phase shift with respect to frequency, $p = 0.175$ for a confidence level of 95%. The statistically insignificant difference in slope demonstrates that the locomotion dynamics is largely unaffected by leg type. The locomotion is dominated by the body pitching and colliding with the ground during each gait cycle. The locomotion of the pacing gait is similar to the

bounding gait, however, the body rolls and collides with the ground. An analysis of covariance shows a similar behavior, showing no statistically significant difference in slopes, $p = 0.056$ for a confidence level of 95%. These two types of gaits are dominated by the dynamics of the body, showing similar trends in the phase shift of the kinetic energy and gravitational energy regardless of the compliance of the leg. The dominance of the body dynamics is again reflected in the velocity performance of the robot, Figure 3.7, which shows roughly similar performance for the bounding and pacing gaits regardless of leg type.

The pronking and the trotting gaits, bottom row of Figure 3.8, show an influence of leg type on the phase shift of kinetic and gravitational energy. Pronking (bottom left Figure 3.8) shows an overall statistically significant difference in the slopes, $p = 2.50e{-}9$ at a confidence level of 95%. In this gait, the MRTV and silicone foam legs maintain a phase shift around 0° through all driving frequencies, demonstrating a SLIP-like energy exchange. The PDMS, TangoBlack+, and rigid legs show similar behaviors, increasing in phase shift with increasing driving frequency after 17.4 Hz. The departure from a phase shift of 0° shows a shifting locomotion model, from a SLIP-like running to an IP walking, or IP kinematic running. An analysis of covariance on the trotting gait shows a statistically significant difference in the slopes of the phase shift related to the frequency as well, $p = 0.001$ at a confidence level of 95%. Leg material trends are similar to those seen in pronking gaits.

Studying the phase shift provides insight into the dynamics of locomotion, largely regarding how gravitational energy is exchanged with kinetic energy. By

looking at the phase shift over both gait and leg type, the influence of these two factors on overall locomotion dynamics is assessed. The body-dominated gaits, bounding and pacing, both show a deviation from a 0° phase shift with increasing frequency. However, the leg materials (and therefore dynamics) have little effect on the overall locomotion dynamics. The phase shift in the pronking and trotting gaits shows that these two gaits are influenced by the mechanical properties of the legs, showing statistically significant differences in the slopes of phase shift relating to driving frequency.

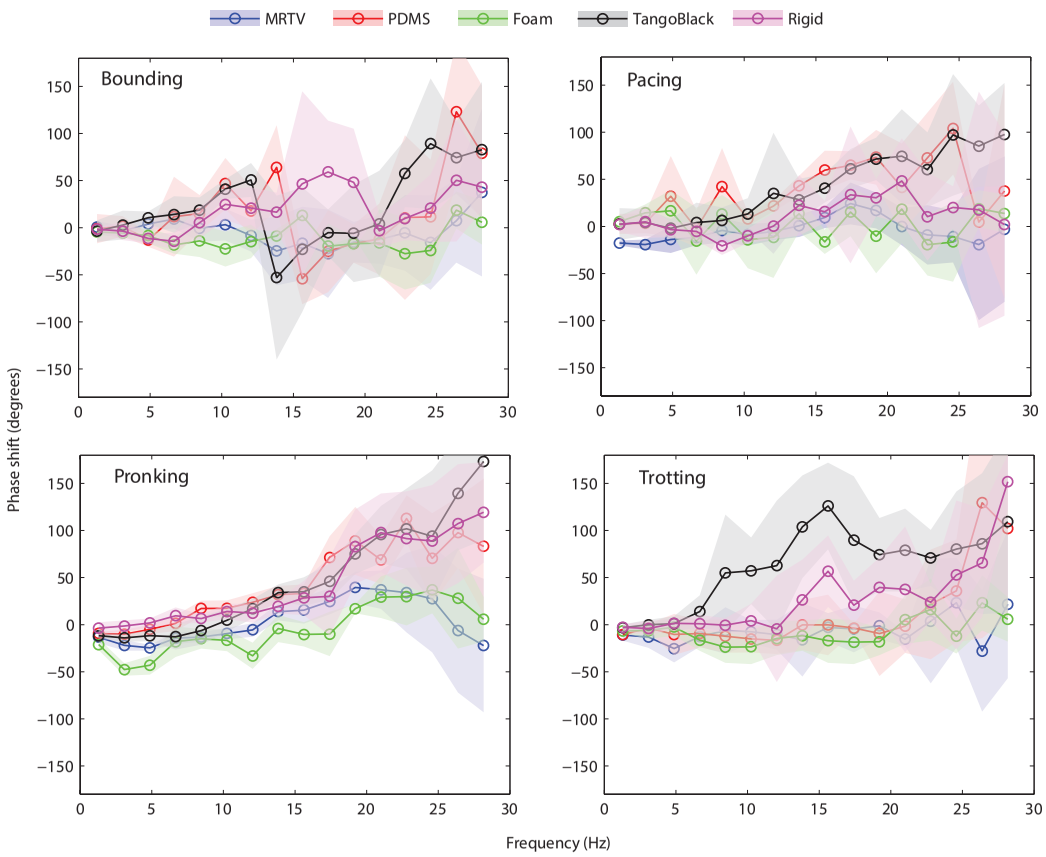

Figure 3.8: The calculated phase shift for each gait type and leg type. The solid lines represent the average phase shift, averaged over more than 10 stride cycles of each of the three trials for a single robot, while the shaded area represents the standard deviation.

3.5.3 Dynamic repeatability

3.5.3.1 Metrics

To better evaluate locomotion stability across leg type and gait, Floquet theory was used to look at the dynamic stability of the locomotion of the quadrupeds [77]. Given that locomotion is cyclic, the stability of the gait from cycle to cycle can be analyzed by looking at the mapping from one critical point in a stride to the next. The full state vector, q, of the quadrupeds is:

$$q = [x\ y\ z\ \theta\ \phi\ \psi\ \dot{x}\ \dot{y}\ \dot{z}\ \dot{\theta}\ \dot{\phi}\ \dot{\psi}]^{\top} \tag{3.4}$$

with the state vector consisting of x, y, and z as the linear positions, and θ, ϕ, and ψ as the angular positions of the robot and their respective time derivatives.

A mapping of the system representing the dynamics at a Poincaré section from the ith to the $i + 1^{th}$ cycle is shown by:

$$q^{i+1} = P(q^{i}) \tag{3.5}$$

where P is a nonlinear function.

The steady-state state vector, q^{*}, is calculated by

$$q^{*} = \frac{1}{m} \sum_{i=1}^{m} q^{i} \tag{3.6}$$

where m is the number of locomotion cycles. The deviations from the state-steady, Δq^{i}, is

$$\Delta q^{i} = q^{i} - q^{*} \tag{3.7}$$

which represents the deviations from the steady-state locomotion per cycle at the point of interest.

When the system reaches steady-state locomotion, the mapping from equation 3.5 becomes:

$$q^* = P(q^*) \tag{3.8}$$

where q^* and P are the steady-state state vector and Poincaré mapping respectively. Any perturbation from this steady-state, given by Δq^i, is mapped by:

$$\Delta q^{i+1} = J(\Delta q^i) \tag{3.9}$$

where J is the Jacobian matrix. The mapping of perturbations, from cycle to cycle, of the steady-state by the Jacobian matrix gives a numerical value to stability. The stability of q^* can then be determined by the eigenvalues of J. When the gait is stable, the magnitude of all of eigenvalues is less than 1. The stability metric will be measured by taking the maximum of the absolute values of the eigenvalues, given by $|\lambda|_{max}$.

3.5.3.2 Experimental results

While the full state vector is available using the OptiTrack setup, it is advantageous to use the reduced state of the quadrupeds taken with high speed cameras, resulting in more data points per stride with less noise in the time derivative terms than using the OptiTrack system. The reduced state vector, given by q_r,

$$q_r = [x \ z \ \theta \ \dot{x} \ \dot{z} \ \dot{\theta}]^\top. \tag{3.10}$$

describes the motion of the robot in the sagittal plane. Although the reduced state neglects the yaw and roll of the robot directly, it is indirectly captured in the high

speed video as a projection onto the reduced state. The high speed video was analyzed with TEMA (Image Systems) marker-less tracking software, tracking the geometric center of the body of the robot to extract the reduced state vector at 0.001 s intervals.

The Jacobian, from equation 3.9, mapping the ith and $i+1^{th}$ deviations from steady-state (equation 3.7), was fit using the **lsqcurvefit** function in MATLAB, similar to [78]. The eigenvalues are calculated from the fit Jacobians to determine the stability.

Figure 3.9 shows the average maximum eigenvalue of more than 10 gait cycles over three trials of a single robot (solid lines) with the shaded area representing the standard deviation. The silicone foam legs, regardless of gait type, always exhibited stable locomotion, showing a maximum eigenvalue less than one. This is attributed to the high compliance of the silicone foam legs, wrapping around the hip joints of the robot and acting as tires. Tires, as opposed to legs, keep consistent contact with the ground and produce a stable forward locomotion. The rigid legs, as compared to any of the compliant legs using the same gait, crossed over into the unstable region at lower driving frequencies than any of the compliant leg counterparts. In part, the ground contact of the rigid leg is different than the polymer legs, generally providing an elastic collision with the ground, causing the rigid leg to rotate opposite to the intended direction and often missing the subsequent step. The MRTV polymer legs, when compared across similar gaits, remain stable and with lower eigenvalues than the other legs, excluding the silicone foam ones. From these results, it is clear

that the mechanical properties of the MRTV legs are advantageous for high-speed, dynamically stable running.

The experimentally determined eigenvalues provide insight into the influence of leg material and gait on locomotion stability. By choosing a leg and gait type with favorable mechanical properties, the locomotion remains stable over a larger actuation frequency range. Additionally, calculating the experimental eigenvalue provides a metric related to the efficacy of passive control for stable locomotion. In the experimental platform, the robots are driven in a feed-forward strategy, without any feedback. A robot with a gait and leg material that results in an eigenvalue below one requires less active control to maintain stable locomotion. However, robots that show unstable dynamics, with eigenvalues greater than one, would require active control to maintain stability. Therefore, when sensing and computing resources are limited as in gram-scale robots, it is advantageous to choose a gait, leg material, and operational parameters, such as driving frequency, that promote stability in a feed-forward configuration.

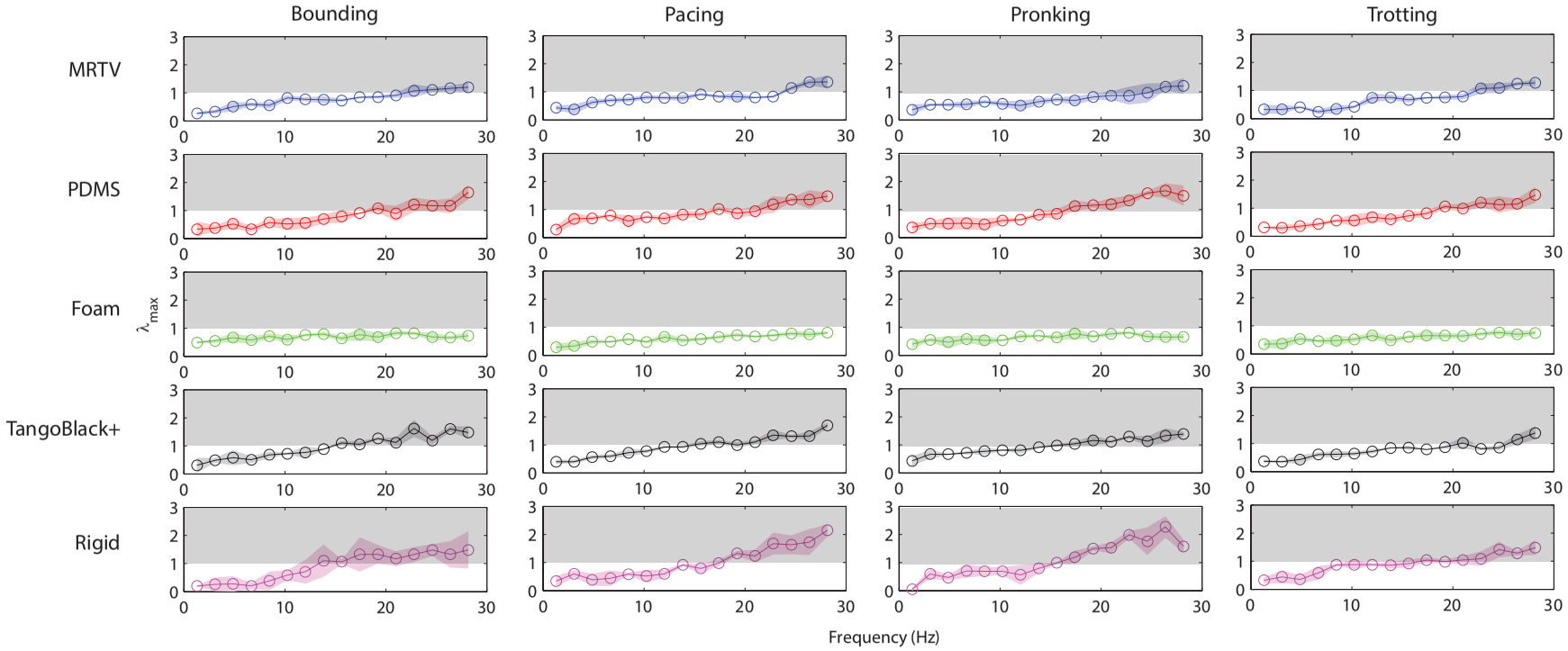

Figure 3.9: Calculated average maximum eigenvalue (solid line) and standard deviation (shaded area) for each gait and leg type. The eigenvalue is calculated over ten strides and averaged over three trials for a single robot for each leg type.

3.6 Simulation insights

While the experimental data highlight the effects of leg compliance and damping on the overall performance (e.g., speed, energy-exchange, and dynamic repeatability) of the robot, the experimental data only examine five different leg types with varying compliance and damping. Exploring a larger parameter space of compliance and damping is a challenge experimentally. However, a simulation with reduced complexity gives insight into the the behavior of the robot with varying compliance and damping values attributed to the leg. These simulations are focused only on the trotting gait, which benefits from the dynamics influenced by leg type, producing the fastest speed performance with a large stability range.

The simulations were performed by Wei Gao and Professor Jonathan Clark of Florida State University using a simulation environment previously developed and used in [79, 80]. The resulting data were shared and overall conclusions were discussed as a group. The following sections present that shared data and explores the insights from these simulations on the design and ultimately control of gram-scale legged robots.

3.6.1 Overview of simulation

Figure 3.10 shows a sketch of the modified SLIP model, incorporating a linear damper in parallel with the spring leg. The leg rotates fully around the point mass representing the body, driven by a torque acting on the hip, similar to the experimental setup. Equations 3.11 and 3.12 describe the stance phase, in polar

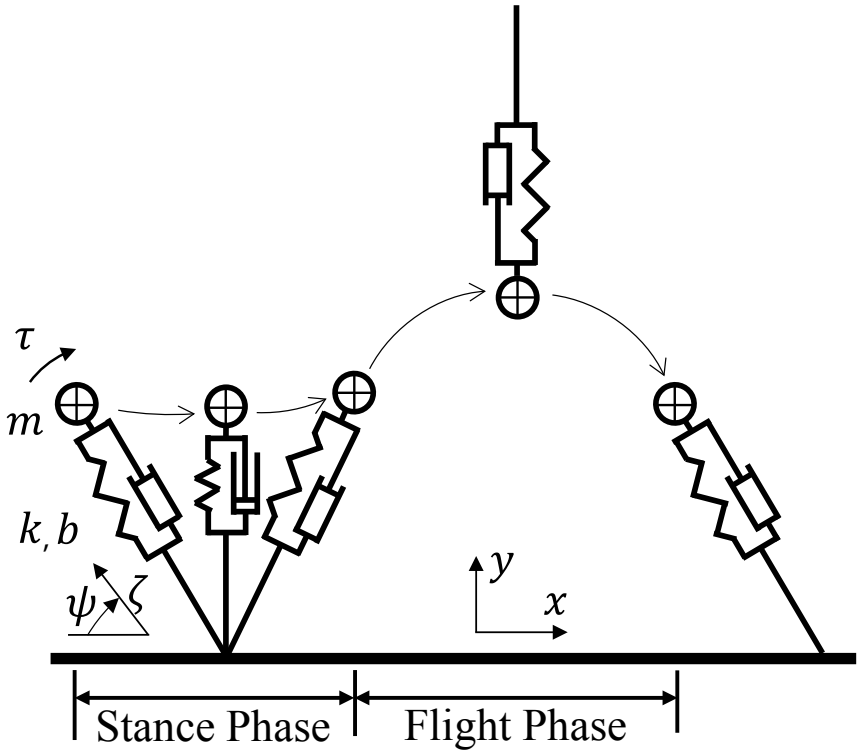

Figure 3.10: Schematic of the torque-driven SLIP model with a damper in parallel to the spring within the leg.

coordinates, and the aerial phase, in Cartesian coordinates.

$$\begin{cases} \ddot{\zeta} = \zeta\dot{\psi}^2 - g\sin\psi - \frac{k}{m}(\zeta - l) - \frac{b}{m}\dot{\zeta} \\ \ddot{\psi} = -\frac{2\dot{\zeta}\dot{\psi}}{\zeta} - \frac{g\cos\psi}{\zeta} + \frac{\tau}{m\zeta^2} \end{cases} \tag{3.11}$$

$$\begin{cases} \ddot{x} = 0 \\ \ddot{y} = -g \end{cases} \tag{3.12}$$

m and l are the mass and nominal leg length parameters for the robot at 1.09 g (including a downward force from the actuator magnet) and 5.64 mm distance hip to toe. k and b are the spring and damping constants. For a fair comparison between the simulated system to the experimental system, the spring and damping constants were multiplied by a factor of two to account for the double-legged stance phase within the trotting gait. The input torque, τ, was modeled from the interaction of the robot magnets and actuator magnet as a PD controller. The PD controller equation describing applied torque is

$$\tau = k_p(\psi_{des} - \psi) + k_d(\dot{\psi}_{des} - \dot{\psi}) \tag{3.13}$$

where ψ_{des} and ψ and their time derivatives are the desired and actual angular position and velocity of the torque controller. The gains, k_p and k_d, were found experimentally. To find these gains, the robot was suspended directly above the magnet without ground contact at a distance of 100 mm, similar to the experimental conditions. The rotation of the actuation magnet and robot was filmed at 2,500 fps (Photron FastCam UX100). The rotations of the leg, representing the actual angle (ψ) and of the actuator magnet, representing the desired angle (ψ_{des}), were tracked

using markerless tracking software (TEMA ImageSystems). The applied torque on the leg is assumed to be

$$\tau = J\ddot{\psi} \tag{3.14}$$

where the applied torque goes fully into the rotational acceleration ($\ddot{\psi}$) of the rotating leg. The mass-moment of inertia, J, of the leg is estimated from SolidWorks as 0.26 g $\cdot$ mm. Assuming all of the torque generated goes towards rotating the leg, equations 3.13 and 3.14 are equal. Fitting the tracked angular position, velocity, and acceleration data at driving frequencies from 1.29 Hz to 28.2 Hzto equations 3.13 and 3.14 gives a lumped parameter estimation of k_p and k_d . The fit k_p and k_d parameters used in the simulations are $2.40e-5$ N $\cdot$ m/rad and $5.01e-10$ N $\cdot$ m $\cdot$ s/rad.

3.6.2 Simulation results

Figure 3.11(left) shows the average experimental data for the trotting gait for the MRTV, PDMS, and TangoBlack+ legs plotted against the non-dimensional speed, given as the Froude number (Fr), and the cost of transport (COT), with the shaded area surrounding the markers representing the error on the Froude number and COT. The simulation used stiffness values ranging from 10 N/m to 200 N/m in 10 N/m steps, while the damping ranged from 0.05 N $\cdot$ s/m to 0.5 N $\cdot$ s/m in steps of 0.05 N $\cdot$ s/m. The simulated data for varying damping and compliance values for the leg is shown in the right column and plotted on the same axes. The simulated data differentiates the more stable points; simulations with an eigenvalue less than 0.75 are represented by a filled marker, and less stable points with an eigenvalue

between 0.75 and 1 are represented by an unfilled marker. Froude number (Fr) is defined as

$$Fr = \frac{v^2}{gl_0} \tag{3.15}$$

where v is the velocity, g is the acceleration of gravity, and l_0 is the nominal leg length [81]. The Froude number is the ratio of the centripetal force to the gravitational force and is often used as a dimensionless velocity term to compare speeds across scales. A higher Froude number signifies a higher velocity. The cost of transport (COT) is a dimensionless number comparing the energy efficiency when moving a mass. In these simulations and experimental work, COT is considered as mechanical COT, which only looks at the mechanical power to move the center of mass. COT is defined as

$$COT = \frac{P}{mgv} \tag{3.16}$$

where P is the mechanical power ($P = \tau 2\pi f n_{legs}$) , m is the mass, g is the acceleration of gravity, f is the frequency, n_{legs} is the number of legs, and v is the velocity. Therefore a lower COT can signify a lower power needed to move the mass of the robot at a given velocity, a faster velocity at the same power, or both lower power and higher velocity.

The top plots in Figure 3.11 show the experimental data and simulation data plotted with a color map representing the energy recovery ratio (ERR). ERR is a metric presented here to describe the ratio of energy stored elastically in the spring against the energy dissipated through the damper. It is defined mathematically as

$$ERR = \frac{E_{max_{spring}} - E_{take-off_{spring}}}{E_{damper}} \tag{3.17}$$

where

$$E_{max_{spring}} = \frac{1}{2} k \delta_{max}^2 \tag{3.18}$$

$$E_{take-off_{spring}} = \frac{1}{2} k \delta_{take-off}^2 \tag{3.19}$$

$$E_{damper} = \int_{t_1}^{t_2} \frac{1}{2} c \dot{\delta}^2 dt. \tag{3.20}$$

The deflection of the leg is δ, with the deflection of the leg at take-off (when the leg is no longer in contact with the ground) as $\delta_{take-off}$, and the rate of the deflection of the leg is $\dot{\delta}$. The energy in the damper is integrated over the time in which the leg is in contact with the ground. A high ERR, $ERR > 1$, implies that energy is predominately stored and returned elastically, with minimal amounts lost to damping, while a low ERR, $ERR < 1$, suggests less elastic energy storage and greater energy dissipated by the damper.

ERR is obtained experimentally from the high speed videos of the robots by tracking the displacement of the foot relative to the hip to find δ and $\dot{\delta}$ using markerless tracking software. The TangoBlack+ legs have a low ERR (< 0.5), predominately from the lack of deflection in the legs of the robot (and therefore minimal stored and recovered energy). Robot trials using these legs also resulted in a low Froude number value and a high COT. The PDMS legs have ERR values from 1 to 2.5 and contribute lower COT values than the TangoBlack+ legs due to the comparatively larger aerial phase, and Froude values up to 0.5. The MRTV legs show the highest Froude number values with the lowest COT values. The energy

recovery ratio for MRTV is low, compared to PDMS, having values between 0.5 and 1.0.

Looking at the simulated data on the right, most of the stable points (filled) have ERR values of 0.5 and lower. Data points with higher Froude numbers and lower COTs show higher ERR values, but lower stability (higher eigenvalues). In simulation, points with very high ERR values also have low velocities, shown by the low Froude number. Overall, the energy recovery ratio in locomotion is related to the magnitude of the aerial phase as well as the contact time on the ground. Effective, high speed, legged locomotion balances large aerial phases with favorable ground contact.

The second row of Figure 3.11 shows the same data, however, the color map distinguishes the stride frequency. In the experimental data, a higher stride frequency results in a higher COT without a similar increase in Froude number. In simulation, the higher driving frequencies result in higher velocities, thus higher Froude numbers, along with lower COT values. Even if only more stable points are considered from the simulation data (e.g., driving frequencies below 22 Hz), higher driving frequencies show both lower COT values and higher Froude numbers in comparison to experimental data. This differing trend between experiment and simulation is in part due to the idealized simulation environment, which assumes no missed or slipped ground contact.

The same data are again shown in the third row of Figure 3.11 with a color map distinguishing the phase shift in kinetic and gravitational potential energy. The phase shift, as discussed in Section 3.5.2, provides insight into the locomotion behav-

ior. The experimental data shows that the more compliant legs, MRTV and PDMS, exhibit a running behavior with a phase shift close to 0°, while the TangoBlack+ legs show a phase shift between 60° and 80°. In simulation, the points suggesting a running energy phasing are also the more unstable points. Running, in these simulations, has a large aerial phase, contributing to the higher eigenvalue, but overall a higher velocity. Larger phase shifts imply a walking locomotion profile, and in this case, generally slower speeds. However, these points are comparatively more stable. In a feed-forward actuation of legged robots, a predominately kinematic locomotion profile is predictable as compared to more dynamic locomotion, e.g. running.

Overall, the plots shown in Figure 3.11 start to build insight into the trade-offs of stability, speed, and efficiency when designing gram-scale legged robots with a feed-forward control. For further insight into the design map, Figure 3.12 plots the simulated points against the relative stiffness and damping ratio. Each point on the plot represents a stable point, an eigenvalue less than one, and are plotted without regard to stability as in Figure 3.11. While multiple stable points at each relative stiffness and damping ratio point exist, each point represents the maximal speed performance for each spring and damper combination. Again, the stiffness values ranged from 10 N/m to 200 N/m in 10 N/m steps, while the damping ranged from 0.05 N $\cdot$ s/m to 0.5 N $\cdot$ s/m in steps of 0.05 N $\cdot$ s/m. The relative stiffness is defined as

$$k_{rel} = \frac{kl_0}{mg} \tag{3.21}$$

where k is the stiffness, l_0 is the nominal leg length, m is the mass, and g is gravity.

The damping ratio is

$$\zeta = \frac{b}{b_{cr}} \tag{3.22}$$

where

$$b_{cr} = 2\sqrt{km}. \tag{3.23}$$

Within these plots, the experimental values corresponding to the maximal performance of the MRTV and PDMS legs are plotted alongside the simulation data. For the MRTV and PDMS legs, the relative stiffness is 34.5 and 114, while the damping ratios are 18.2% and 9.98% respectively. The TangoBlack+ legs are not included due to their high damping > 1 N $\cdot$ s/m, beyond the range of simulation.

Figure 3.12(top left) maps the cost of transport onto the relative stiffness and damping ratio map. Low COT values coincide with low damping ratios, less than 25%, and over a range of relative stiffnesses, up to 86.2, well beyond the biologically relevant range of 7 to 27 [6, 21, 82]. The calculated COT for the experimental points for MRTV and PDMS legs are higher than the simulation trends. Largely, the simulations are idealized and neglect any losses that the physical platforms experience.

The top center plot of Figure 3.12 looks at the non-dimensional speed, the Froude number, over the relative stiffness and damping ratio space. The highest Froude numbers, over 2.5, are seen over relative stiffness between 34.5 and 51.7 and very low damping ratios, below 10%. These same points show the lowest COT. The majority of the points exist with Froude numbers less than 1. In general, slower speeds are more stable, but a wide range of values for the stiffness and damping

promote similar locomotion speeds, showing a relatively insensitive design space of the spring and damper for moderate performance. The Froude number of the experimental points are lower than the predicted simulation trends, again attributed to the idealized simulation.

The energy recovery ratio is shown in the top right plot. Larger ERR values occur with high relative stiffnesses and low damping ratios. As the damping ratio increases, with the same relative stiffness, the energy recovery ratio decreases. Similarly, increasing the relative stiffness with a somewhat constant damping ratio increases the energy recovery ratio. The MRTV ERR value is similar to the predicted trend, however, the PDMS ERR value is low in comparison to an extrapolated trend. However, due to the lack of stable gaits at the parameter space near PDMS, the overall trend could be different than an extrapolated trend that assumes a high ERR value at the PDMS location. Overall, a high ERR value implies a high stiffness with a low damping value that promotes large aerial phases, but can also promotes largely vertical, rather than horizontal, take offs from the ground, lowering the horizontal velocity component and promoting unstable behavior.

The maximum eigenvalue is shown in the bottom left plot and gives a sense of stability for the system. In general, a low eigenvalue signifies that the corresponding physical system will be stable. The high Froude number and low COT points correspond to high eigenvalue points. Largely, the stable points, with eigenvalues of 0.6 and under exist over a relative stiffness up to 74.7, but with damping ratios from 50% to 250%. The experimentally determined eigenvalue for MRTV coincides with the predicted trends. While the PDMS experimental eigenvalue is stable, with an

eigenvalue around 0.85, simulation data with eigenvalues less than one do not exist at this high stiffness. Physical systems with relative stiffnesses and damping ratios all throughout the space can be constructed, but it is likely that their operational ranges will be limited.

Figure 3.12(bottom center) shows the stride frequency of the point with the maximum velocity performance. The points with the highest stride frequency coincide with the points with the highest Froude number. The relative stiffness values with the highest damping ratios show the lowest stride frequencies. In general, a high damping ratio limits the actuation frequency. The MRTV and PDMS experimental actuation frequencies are lower than predicted trends, assuming that the simulation points near PDMS would show stride frequencies greater than 20 Hz.

Finally, the bottom right plot of Figure 3.12 show the energy phasing of the kinetic and gravitational potential energy. Low damping ratio values keep the kinetic and gravitational energies in sync, consistent with a running profile. Mechanically, a damping element causes a phase lag between the force and displacement. In this system, that same lag is apparent between the kinetic and gravitational potential energy; with a higher damping ratio, the phase shift between the energies increases. The experimental values are consistent with a predicted phase shift close to 0°.

3.7 Discussion

Gram-scale robots are generally resource-limited – an inherent limitation with decreasing size of robots. Resource-limited robots have limited sensing abilities, actua-

tors, power, communication, largely due to the lack of readily available, miniaturized components to support these abilities on an autonomous gram-scale robotic system. Balancing performance demands, e.g. high speed, with higher level goals, e.g. moving to a specified location, requires a gram-scale autonomous robotic system to use finite resources, such as battery power, judiciously. By designing a robot with stable dynamics, the demand for an active controller with corresponding sensors, actuators, and power consumption, is reduced. Therefore, creating autonomous gram-scale robots requires an understanding of the locomotion dynamics through design to promote stable behaviors and passive control, a strategy used in the design and control of marine vehicles [83, 84].

The utility of Figures 3.11 and 3.12 comes from considering the design of a gram-scale legged robot. These figures represent an eight-dimensional space; locomotion metrics such as cost of transport and velocity map onto the leg design parameters, expressed as relative stiffness and damping ratio. Using these maps, a gram-scale legged robot can be designed with a relative stiffness and damping ratio to promote desired behaviors. These maps can also be used to explore the trade-offs of these often competing interests. For example, high Froude numbers, signifying high velocities, competes with stability.

For example, to promote a running behavior, a phase shift around 0° (Figure 3.12 bottom right), leg design parameters with a relative stiffness between 17.3 and 80.5 and damping ratios between 8.33% and 22.4% could be used. However, these same points correspond to points with eigenvalues greater than 0.80 (Figure 3.12 bottom left). While these design parameters would promote a running

behavior, the high eigenvalues (>0.75) suggest a need for an active controller to maintain stable running. However, to design a robot requiring minimal active control, leg design parameters promoting stable dynamics with low eigenvalues (<0.75) need to be chosen. In this case, the damping ratio for the legs needs to be higher, greater than 22.4%, with the same range of relative stiffnesses. The increased damping causes a phase lag between the kinetic and gravitational energy, changing the locomotion dynamics. However, the increased stability requires little active control to maintain stability, maintaining passive control through the mechanical design.

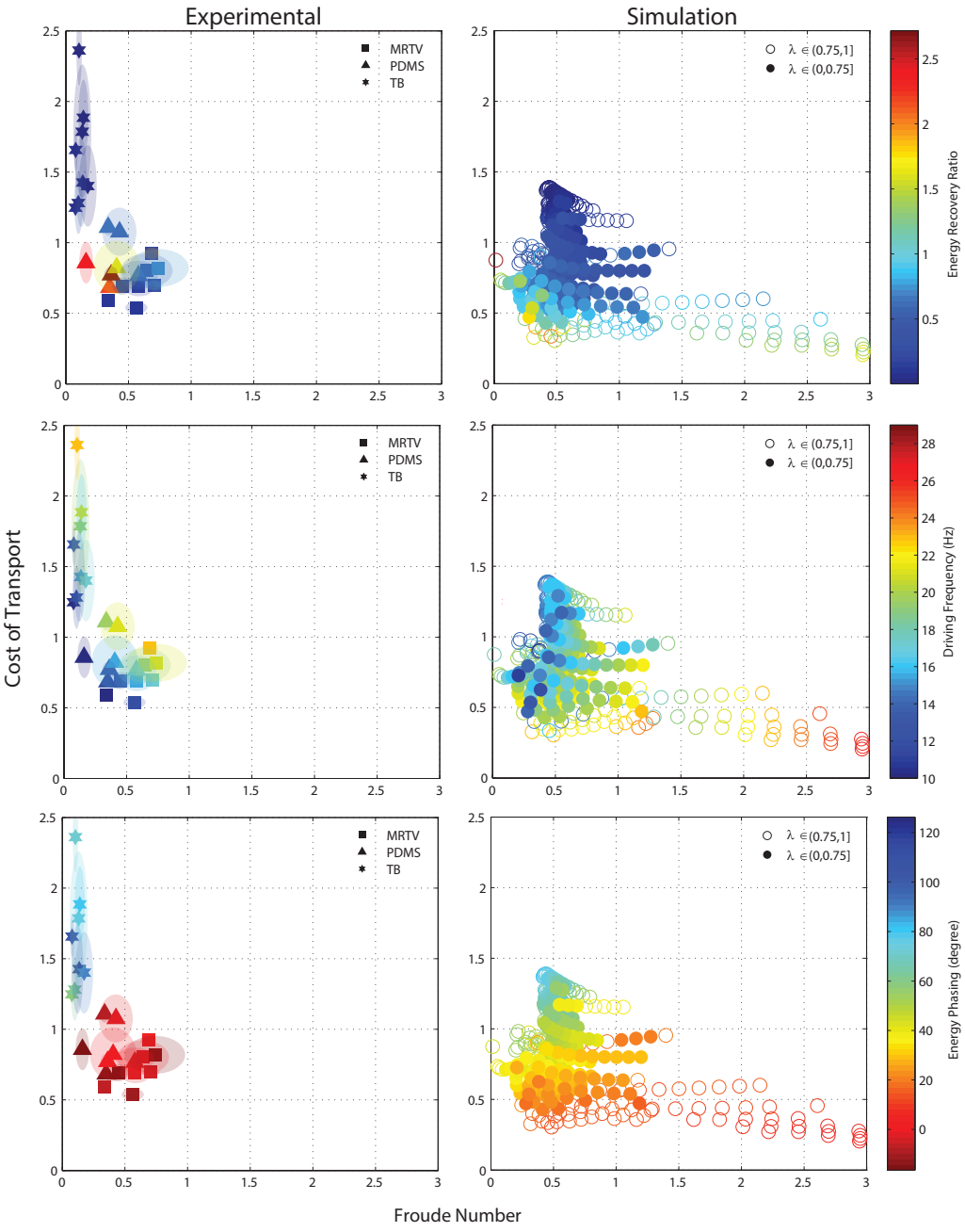

Figure 3.11: Experimental (left) and simulated (right) data points of legged locomotion plotted with the axes of non-dimensional speed (Froude number) and cost of transport. Each pair of plots is repeated with varying color maps, representing the energy recovery ratio (ERR), driving frequency, and energy phasing.

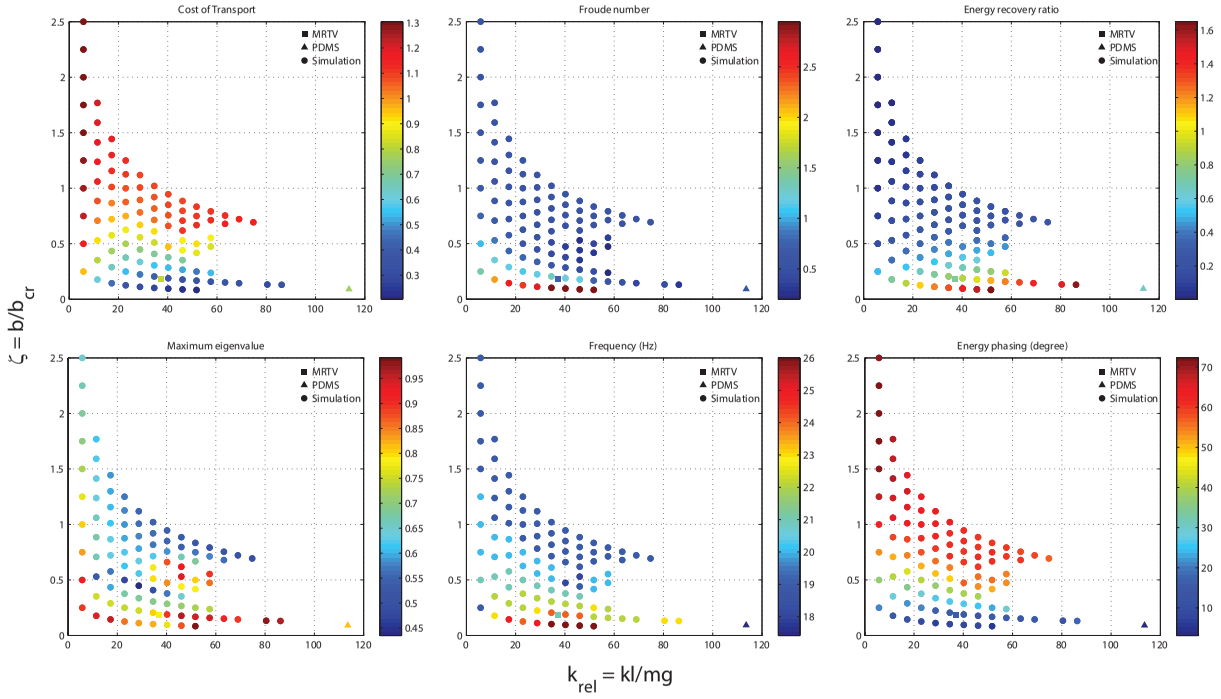

Figure 3.12: Experimental and simulated data points of legged locomotion plotted with the axes of relative stiffness and damping ratio. Each plot is repeated with varying color maps, representing cost of transport, Froude number, energy recovery ratio, eigenvalue, stride frequency, and energy phase shift.

3.8 Conclusions

The work presented in this chapter explores the use of viscoelastic legs as a means to promote fast and stable running in gram-scale legged robots. Gram-scale legged robots were tested over a variety of driving frequencies, gaits, and leg types and ultimately achieved top speeds of 233 mm/s (11.65 body lengths/s) using a trotting gait with compliant and damped MRTV legs. These legs had a relative stiffness of 37.1 and a damping ratio of 18%. The experimental work is brought together with a numerical model to explore a larger space of stiffness and damping values, ultimately providing insight into the design of legs for gram-scale robots that promote desired behavior, such as stable locomotion at reasonable speeds.

The compliance and damping of the various polymer legs were characterized and compared to the legs of cockroaches, a legged runner of a similar size to the robots presented here. Simply matching the compliance and damping of a biological system to a robotic system can offer improved performance, this work explores the design space more fully to understand the trade-offs associated with mechanical design parameters. Through simulation, this work explores the effect of relative stiffness and damping ratio within the legs and finds combinations of those design parameters with predicted speed performance up to 372 mm/s (18.6 body lengths/s). The simulation also provides insight into creating inherently stable robots, using only a feed-forward strategy, by increasing the damping ratio of the legs. However, this often reduces speed. Ultimately, the simulation results also provide a design map for creating gram-scale legged robots, allowing the trade-offs between speed

performance, stability, and efficiency to be explored. This work can then be applied towards tuning the mechanics and dynamics of a robot system to run stably with minimal control.

Chapter 4

μQuad: a 2.5 mm, 1 mg legged microrobot

Legged locomotion in ants spans orders of magnitude in body mass from over 200 mg in *Paraponera clavata* [85] to $<$ 1 mg seen in ants of the subfamily *Myrmicinae* [11]. To understand how locomotion scales with decreasing body mass, this chapter presents a microrobot as an experimental platform to study locomotion at the milligram scale. This chapter characterizes the friction bearings created through the direct laser writing fabrication of the microrobot (robots with body masses under 100 mg), as well as initial insights into the locomotion of the robot.

Empirical biological scaling laws show an increase in relative velocity (body length per second) with decreasing body mass [7]. However, as robots are scaled down, their relative speeds pale in comparison to biological counterparts; most robots have a top speed less than 1 body length per second. At 10 mg a solar-powered polysilicon robot demonstrated autonomous push-ups on two legs [38]. This robot was fabricated with actuators, control electronics, and solar cells for power demonstrating autonomous movement, but no forward motion. At 80 mg a thermally actuated, four-legged microrobot achieved forward locomotion at 6 mm/s (0.4 body lengths per second) [45]. Two lead zirconate titanate (PZT) microrobots were developed to investigate the dynamics of contact interactions in microrobotic legs. The two microrobots, a quadruped (0.16 g) and a hexapod (2.7 g) use off-the-shelf

PZT piezoelectric biomorph structures to created vertical motion in their legs. As these are test structures, a horizontal component has not yet been incorporated, so forward motion has not been demonstrated [43]. More recently though, similarly structured legged microrobots weighing 4.4 g and 379 mg have demonstrated walking at 0.06 body lengths per second and 0.1 body lengths per second, respectively [42]. In terms of speed, the most successful legged microrobot was demonstrated by Vogtmann; at 25 mgthis robot incorporated compliant materials in the leg design and used untethered magnetic actuation to achieve top speeds of 5 body lengths per second [44].

The experimental method outlined in Chapter 2 is limited by the resolution of the manufacturing technique as well as the availability of magnetic material. Polyjet printing on the Objet30 Pro can scale the design down by a factor of 2, creating a 10 mm long, 100 mg robot. However, to further scale down the robot, the manufacturing technique must be changed. Direct laser writing enables microscale 3D printing with feature sizes of 100 nm [86]. 3D printing allows designs to be changed easily to understand legged locomotion at the milligram scale, where mechanics and ground interaction dominate. Larger, insect-inspired robots, like RHex [24], provide a platform for understanding both the morphology and control of legged locomotion, while this work incorporates microscale 3D printing with magnetic actuation to study legged locomotion of robots with a mass 1,000,0000 times smaller.

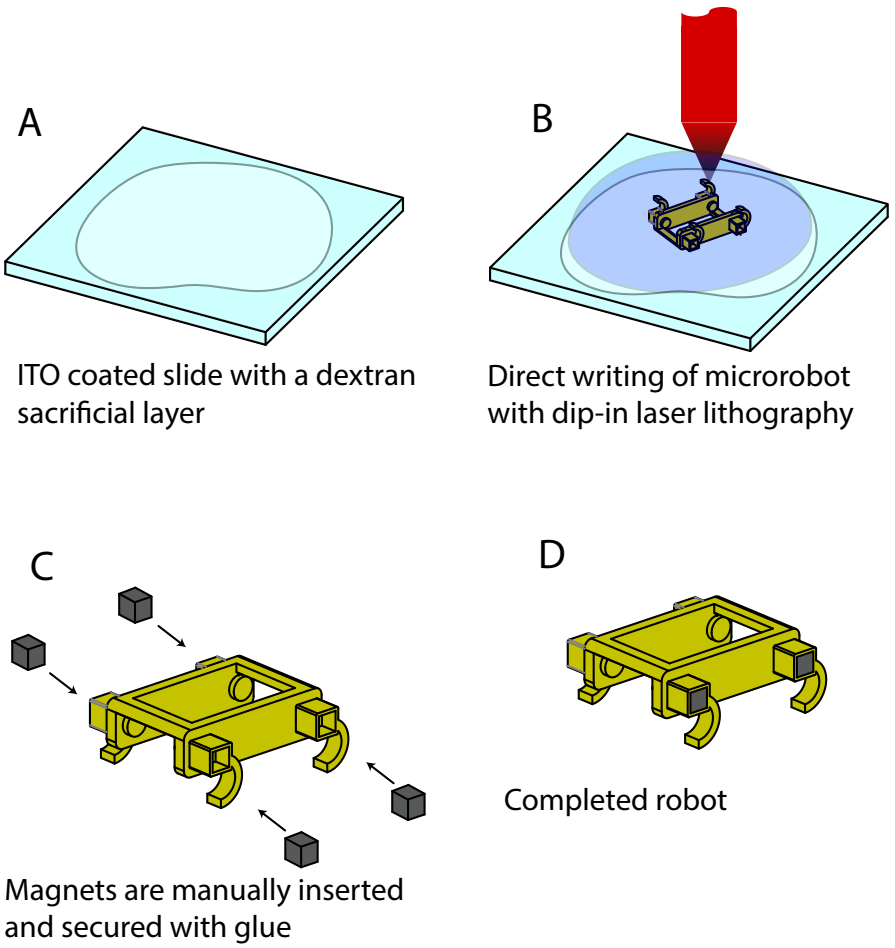

Figure 4.1: Fabrication process for direct laser writing and embedded permanent magnets for actuation.

4.1 Fabrication

The microrobots are fabricated using direct laser writing for 3D printing at the microscale, as illustrated in Figure 4.1. The sacrificial material was made by mixing dextran (Dextran 70 Sigma-Aldrich) with deionized (DI) water to create a 20 wt% solution with DI water. The sacrificial layer of 20% dextran (Dextran 70 Sigma-Aldrich) was spin-coated onto an ITO-coated glass slide (Nanoscribe) at 1,500 rpm for 1 minute (Fig 4.1A). The microrobot structure was written using dip-in laser lithography (DiLL) with a Nanoscribe Photonic Professional GT using the 25X objective (Carl Zeiss Microscopy) and a negative tone photoresist (IP-S Nanoscribe). After printing, the microrobots were developed in propylene glycol monomethyl ether acetate (PGMEA) for 2 hours. The slide was removed from the PGMEA bath and rinsed with isopropyl alcohol (IPA) washing away the PGMEA and excess photoresist. The microrobots were released from the sacrificial layer by dissolving the dextran with DI water. The microrobots were placed in a bath of IPA and sonicated overnight in a heated bath (3510 MTH Branson) to remove excess photoresist in the rotary joints of the robot. Once fully cleaned, 250 μm cube magnets (SuperMagnetMan) were placed in the hip joints manually and secured with cyanoacrylate (Loctite 401). The final fabricated robot is shown in Figure 4.2. The orientation of the dipoles of the embedded magnets mechanically programs the gait for the microrobot. In this work, the dipoles were aligned in the same direction, creating a pronking (4-legged hopping) gait.

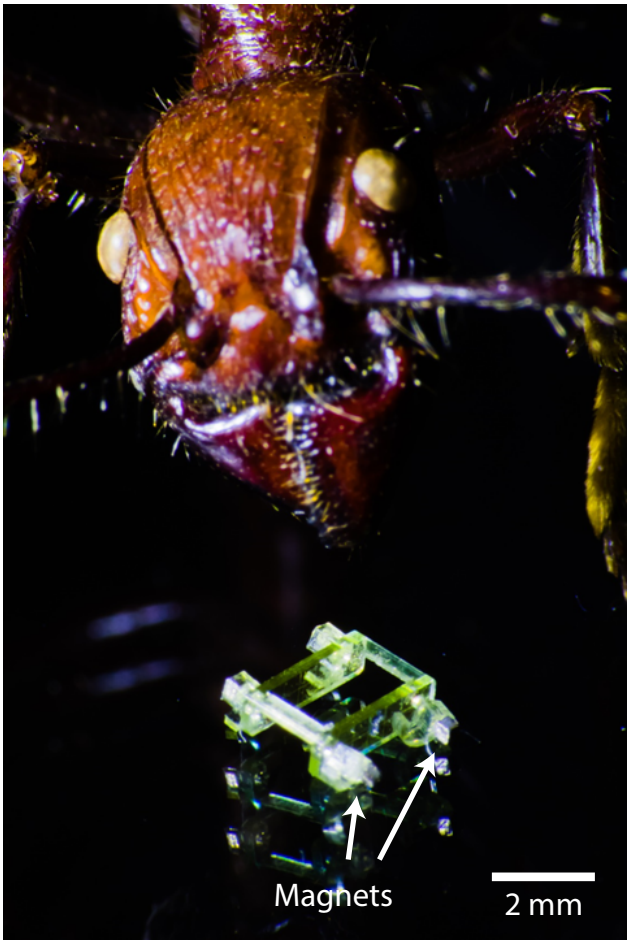

Figure 4.2: Fabricated 1 mg, 2.5 mm x 1.6 mm x 0.7 mm quadrupedal microrobot pictured with a dessicated bullet ant head (Paraponera clavata).

4.2 Experimental setup

Robots are actuated in a custom-made two-axis Helmholtz coil system, used to generate a rotating magnetic field to actuate the embedded magnets. A schematic of the interaction is shown in Figure 4.3. The coil brackets are 3D printed (UPrint Plus SE Stratasys) and wrapped with 22 gauge enameled magnet wire. The (vertical) inner coil pair has a nominal diameter of 120 mm and 60 turns of wrapping, while the outer pair has a nominal diameter of 160 mm and 50 turns of wrapping. To create a rotating magnetic field, each channel of a 2-channel arbitrary function generator (AFG3022C Tektronix) is connected to a current amplifier (TS200-0A Accel Instruments). The output of each channel of the function generator is set to balance the coils, creating a maximum symmetric rotating field of 0.78 mT. The dipole of the 250 μm cube magnets is estimated from the volume and material of the magnets by

$$m_r = \frac{B_r V}{\mu_0} \tag{4.1}$$

where B_r is the residual flux density. The residual flux density of N50 neodymium magnets is between 1.41 T and 1.45 T [87]. V is the volume of the magnet and μ_0 is the magnetic permeability of free space ($4\pi \times 10^{-7}$ N/A^2). Using a mid-range value (1.43 T) for the residual flux density results in an estimated dipole of 17.8 A $\cdot$ mm^2. Using the point-dipole model in [63], the maximum applied torque is calculated to be 13.8 μN $\cdot$ mm.

Since the robot is actuated within a Helmholtz coil, which consists of two solenoid electromagnets on the same axis, and not a permanent magnet as in Chap-

ter 2, the geometric center of the coil pair provides a magnetic field without a gradient. This means that there is not an additional force acting on the robot. However, the zero-gradient portion of a Helmholtz coil system is ±20% of the radius from the center of the coil pair. This corresponds to zero-gradient region in the pair of 32 mm (13 body lengths) in the horizontal direction and 24 mm (9.6 body lengths) vertically.

To track the motion of the robot, the robot was filmed in the sagittal plane with a high-speed camera (Fastcam UX100) at 1,000 fps using a macro lens (Zeiss Makro-Planar T* 2/100mm ZF.2 Macro Lens). The field of view of the macro lens was 150 mm wide, accommodating 7.5 body lengths of travel. The motion of the robot was tracked using markerless tracking software (TEMA Image Systems).

4.3 Characterization of 3D printed rotational bearings

Fully rotational microscale mechanisms are limited by surface forces, such as friction, in their ability to rotate. Solid-solid interfaces in rotating parts often suffer from wear, further decreasing performance. To minimize the effect of friction in rotary devices, contact needs to be limited by either micro-ball bearings [88], hydro-dynamic bearings [89], air bearings created through magnetic or electrostatic suspension [90, 91], or a liquid film [92, 93, 94]. Most of these strategies require complex manufacturing processes with tight tolerances. While the bearings used in this work are still ultimately limited by friction, the fabrication is simple, requir-

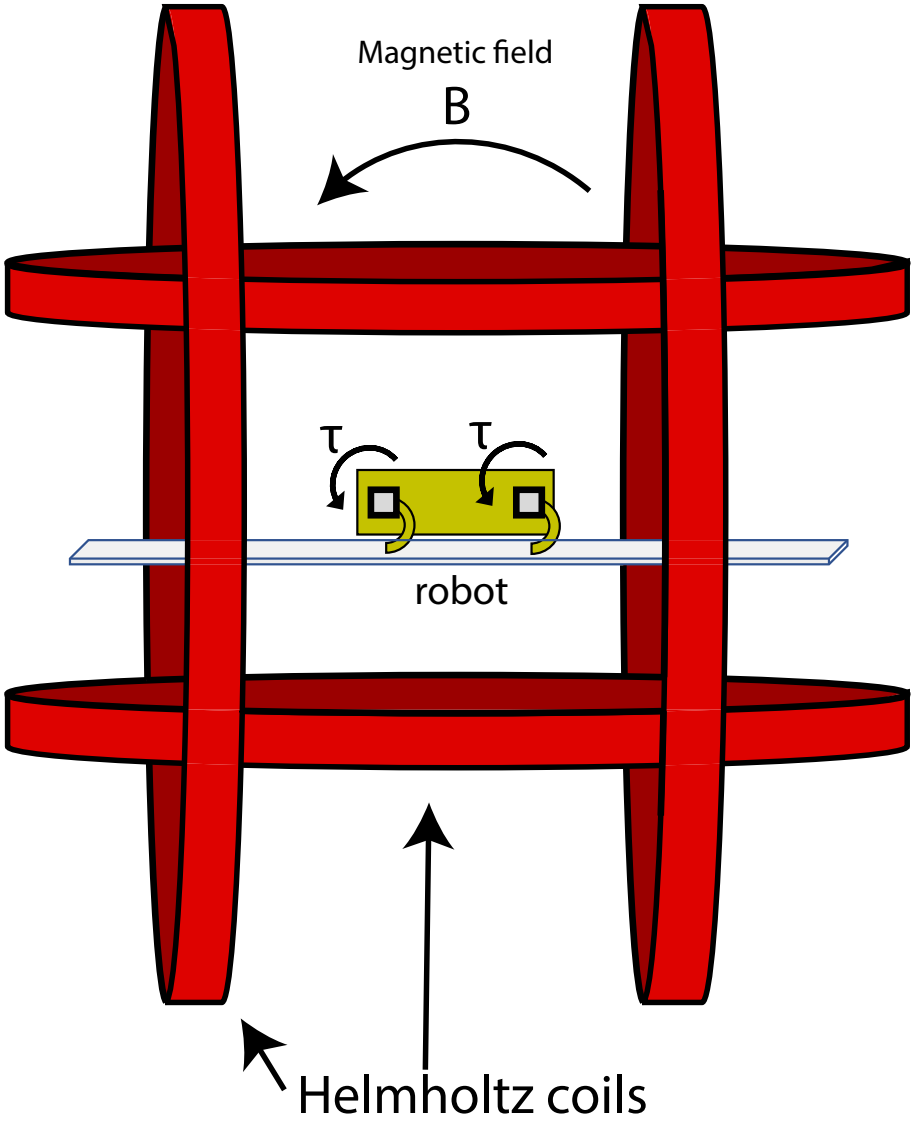

Figure 4.3: The microrobot is actuated in a rotating magnetic field (B), resulting in a torque applied to each of the embedded magnets in the hip joints. The vertical and horizontal components of the magnetic field are generated from each coil pair.

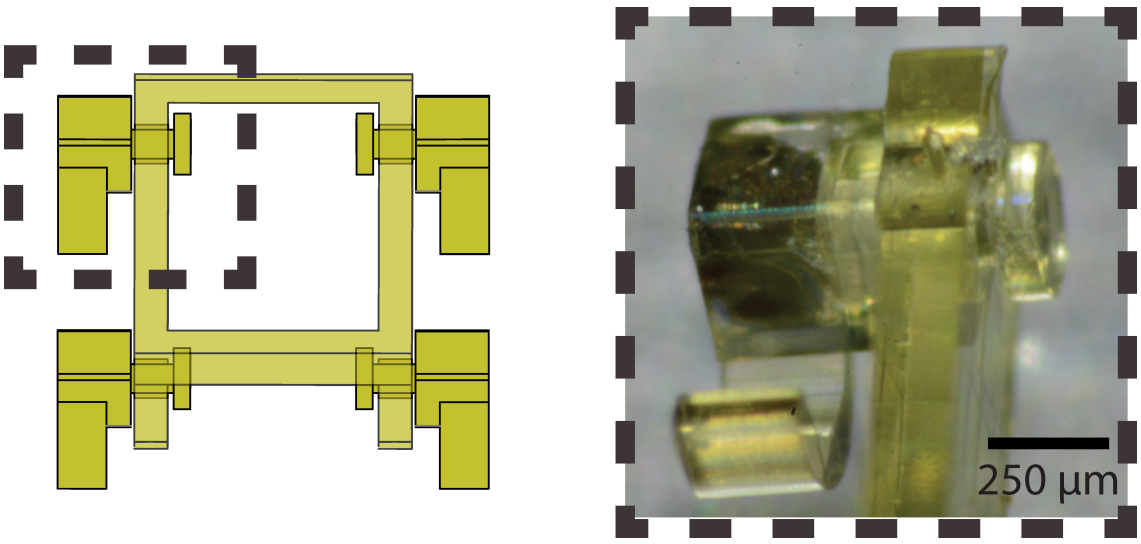

Figure 4.4: (Left) CAD illustration showing the embedded legs within the (transparent) body to create a monolithic bearing. (Right) Photograph of printed component.

ing only a single step. A solid model and photograph of the bearing is shown in Figure 4.4.

4.3.1 Startup torque

The startup torque is the minimum torque applied for the leg to start moving and overcome static friction within the joint. The startup torque was found by positioning the leg both downward and upward, to compensate for any gravitational effects, and energizing the horizontal coil pair to apply a maximal torque to the leg. The coils are powered by a 420 W power supply (Sorensen XPF60-20 DPF) and the voltage is slowly increased until the leg moves and the corresponding current is recorded. The applied voltage and current to the coil is 1.63 ± 0.02 V and

0.55 ± 0.00 A, resulting in a field of 0.31 mT and a calculated start up torque of 5.47 $\mu\text{N} \cdot \text{mm}$.

4.3.2 Actuation response

The rotational mechanism (robot leg) was suspended without ground contact and actuated from 10 Hz to 180 Hz in 10 Hz increments. High speed video of the mechanism rotating was recorded at 2,500 fps (Fastcam UX100) and processed in markerless tracking software (TEMA Image Systems) to determine the average rotational speed. Figure 4.5 shows the average rotational speed of the leg as a function of the driving frequency of the coil system. The leg rotation stays in sync with the actuation up to 150 Hz. Obtaining a higher actuation frequency requires either a stronger magnetic field or a reduction of the friction in the joint, though neither is explored here. However, applying the equation for the step-out frequency in the point-dipole model in [63] gives an overall lumped approximation of the viscous damping in the friction bearing by

$$\omega_{S-O} = \frac{|\tau|}{c} \tag{4.2}$$

where ω_{S-O} is the step-out frequency when the magnets are no longer in sync, τ is the applied torque, and c is the viscous damping. The viscous damping in the system can be calculated as 13.7 $\mu\text{N} \cdot \mu\text{m} \cdot \text{s/rad}$.

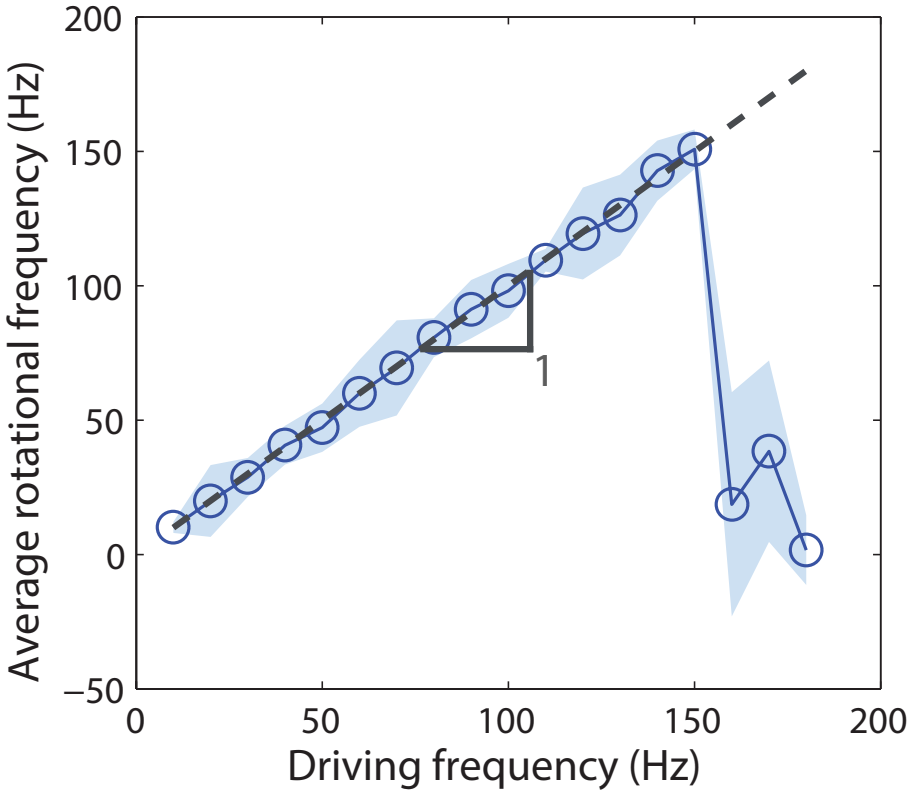

Figure 4.5: The average rotational frequency of a leg of the microrobot not in contact with the ground vs rotating magnetic field frequency. Solid line represents the average and the shaded area represents the standard deviation over >5 rotations. The dashed line visualizes when the rotational frequency of the leg is equal to the driving frequency.

4.3.3 Wear

The leg was actuated at 100 Hz for three hours, corresponding to over 1,000,000 cycles. A high speed video taken at 2,500 fps was recorded at 30 minute intervals, corresponding to 180,000 cycle intervals. The data was processed in TEMA to determine the average rotational speed of the mechanism at each video capture. Figure 4.6 plots the average rotational speed at each 30 minute interval with the shaded area corresponding to one standard deviation. Overall, the average speed does not decrease over 1,000,000 cycles. However, the relatively large standard deviations (10 Hz) are a combination of both tracking error and frictional properties in the joint, though no visible signs of wear were observed.

4.4 Locomotion results

4.4.1 Velocity

The average horizontal velocity of the robot is shown in Figure 4.7. The solid line corresponds to the average value, while the shaded area represents one standard deviation over 3 trials for one robot. The maximum observed velocity of 37.3 mm/s (14.9 body length/s) occurs at 35 Hz. Video stills of the robot running at 23.8 mm/s (9.52 body length/s) are shown in Figure 4.8.

The average velocity is approximately linear from 5 Hz to 25 Hz, suggesting that this portion of locomotion is governed largely by the kinematics of the robot design; as frequency increases, more steps are taken, increasing the horizontal ve-

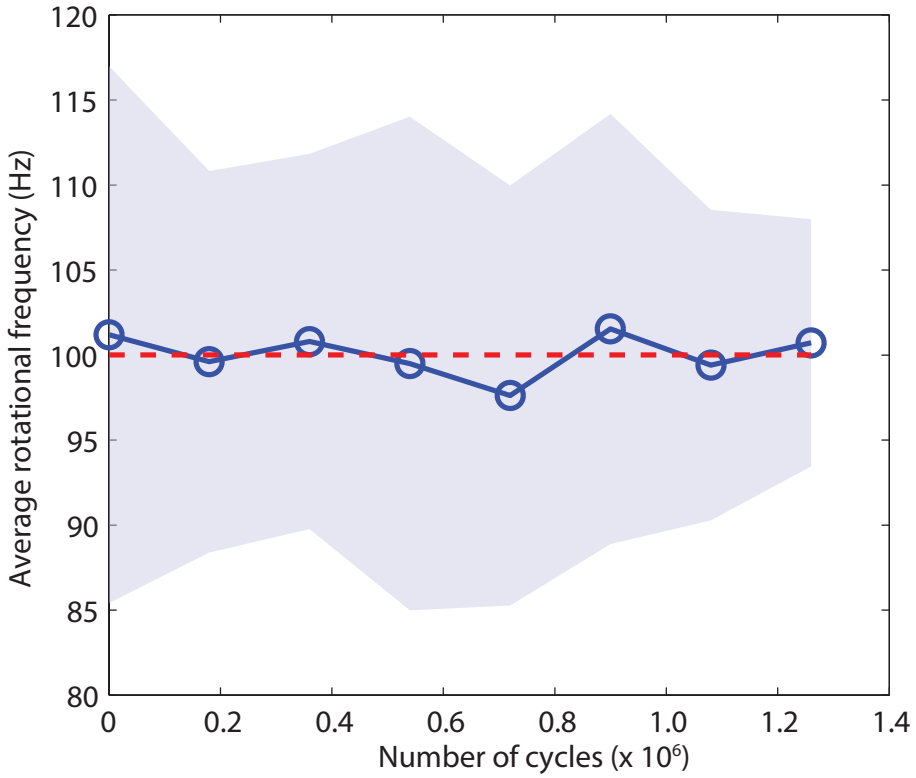

Figure 4.6: The average rotational frequency (solid line) and standard deviation (shaded area) over ten rotations of the leg actuated at 100 Hz (dashed red line) captured at 30 minute intervals (180,000 cycle intervals).

locity proportionally. The slope of this linear fit, corresponding to the stride length, is 0.88 mm, or 0.35 body lengths.

As stride frequency is increased beyond 35 Hz, the velocity performance begins to drop and becomes more inconsistent. The robot is more dynamic, as opposed to kinematic, in this regime, however, the body dynamics are unfavorable to high speed running. The robot body is perpetually pitched downward, and pushes itself forward with the back legs rather than perform the pronking gait. This downward-pitched posture could result from drag as the robot runs forward. The Reynolds number is calculated by

$$Re = \frac{vD}{\nu} \tag{4.3}$$

where v is the velocity of the robot, D is the characteristic length, in this case body length, and ν is the kinematic viscosity of air (15.4 mm^2/s). At the top speed, the Reynolds number is 6.06, signifying that the robot is operating under laminar conditions and according to Stokes's law, viscous drag increases with increasing speed. An estimate of the drag force is found by

$$F_D = \frac{1}{2}\rho v^2 A C_D \tag{4.4}$$

where ρ is the density of air (1.23 kg/m^3), A is the cross-sectional area of the robot, and C_D is the drag coefficient ($C_D = 2.1$ for a rectangular box). The drag force is equal to 1.90 nN when the robot is running at top speeds, roughly 0.19% of the body weight. It is unlikely that the drag force is what is impeding the robot performance, and more likely the unfavorable ground contact, where the leg slips rather than sticks, is limiting performance.

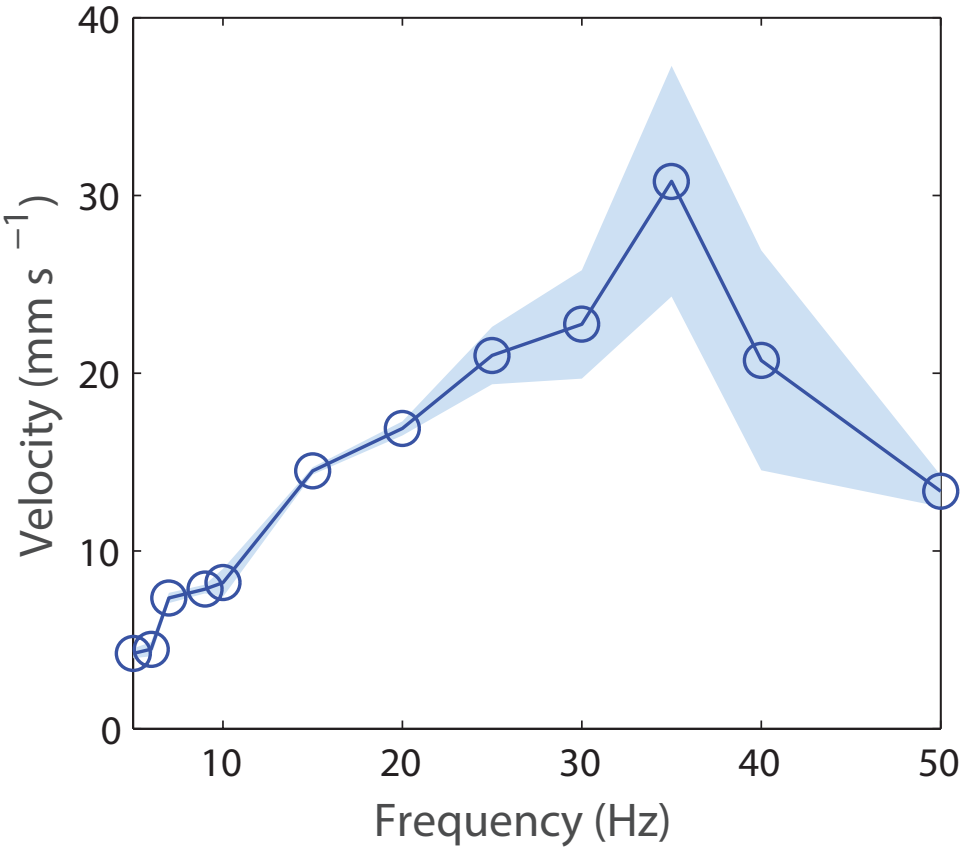

Figure 4.7: Robot speed vs rotating magnetic field frequency. Solid line represents the average over three trials and the shaded area represents the standard deviation for one robot.

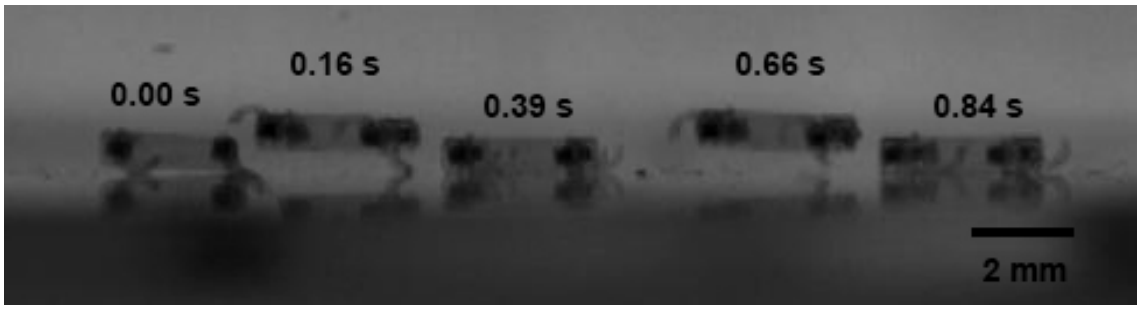

Figure 4.8: Overlaid frames captured from video of the microrobot walking at approximately 9.5 body length per sec

4.4.2 Energy phasing

Horizontal kinetic energy (HKE) and gravitational potential energy (GPE) are calculated from the tracking of the center of mass. HKE is calculated as $\frac{1}{2}m\dot{x}^2$ and GPE as mgh. Locomotion models, such as the spring-loaded inverted pendulum (SLIP) [95] and the inverted pendulum (IP) [96], exchange energy either through elastic storage in a spring, as in SLIP, or through gravitational energy exchange, as in IP. Therefore, the phasing of kinetic energy relative to gravitational energy lends insight to the applicable locomotion model. In SLIP, the stored elastic energy launches the mass in an aerial phase with a high velocity, and consequently a high potential energy, resulting in no phase difference between the kinetic energy and potential energy. The inverted pendulum walking model uses gravity to propel the next step, resulting in an increasing kinetic energy, while potential energy decreases. The kinetic energy and potential energies are 180 ° out of phase in this model.

Figure 4.9 plots the phase shift of the kinetic energy relative to the potential energy as a function of the driving frequency. At low frequencies, up to 30 Hz, the robot has the HKE and GPE in phase. An example of the energy profiles at 20 Hz is shown in Figure 4.10. While the energies are in-phase, indicative of SLIP-like behavior, there is no elastic energy storage within the system. The in-phase behavior is primarily attributed to the robot being a torque-driven system; providing actuation through the whole stride, and consequently, a high kinetic energy when gravitational energy is also high.

At higher driving frequencies, greater than 30 Hz, the robot no longer performs

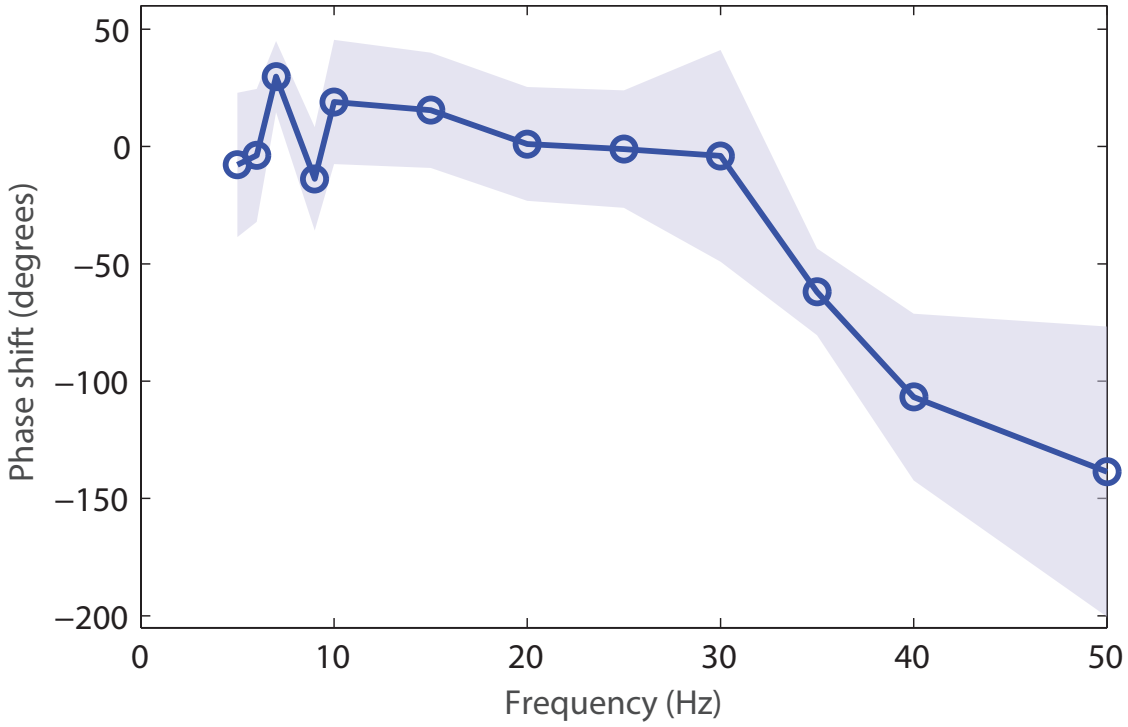

Figure 4.9: Relative phasing of the kinetic energy to the gravitational energy of the robot pronking as a function of driving frequency.

the pronking gait and moves unexpectedly. However, slipping of the legs on the ground is more visible in this regime, namely due to the robot landing on the legs, rather than the body as seen in slower driving frequencies. Ultimately, the slipped ground contact causes a shift in the energy phasing, where the kinetic energy begins decreasing prior to the gravitational energy decrease. Figure 4.11 shows the energy profiles at 35 Hz with the kinetic energy leading the gravitational energy by 50 °. As the locomotion becomes more chaotic with increased driving frequency and the robot is no longer pronking, the energy trends towards 180 °out of phase. Only considering the numerical value of the phasing suggests a walking model. However, this conclusion does not fit with observed motion. Additionally, due to the small mass (1 mg) and actuation scheme, it is unlikely that locomotion is reliant on gravitational energy exchange. Therefore, the information from the energy phasing is inconclusive towards describing the mechanics of locomotion.

4.5 Conclusions

This work shows one of the smallest legged robots, capable of achieving biologically relevant speeds, up to 15 body lengths per second with a mechanical cost of transport ($COT = \frac{P}{mgv}$) of 5.3. This microrobot also provides a platform for studying locomotion at the milligram scale by incorporating microscale 3D printing with magnetic actuation. The monolithically printed chassis creates friction bearings used in the microrobot to provide full rotary actuation, up to 150 Hz, in this experimental

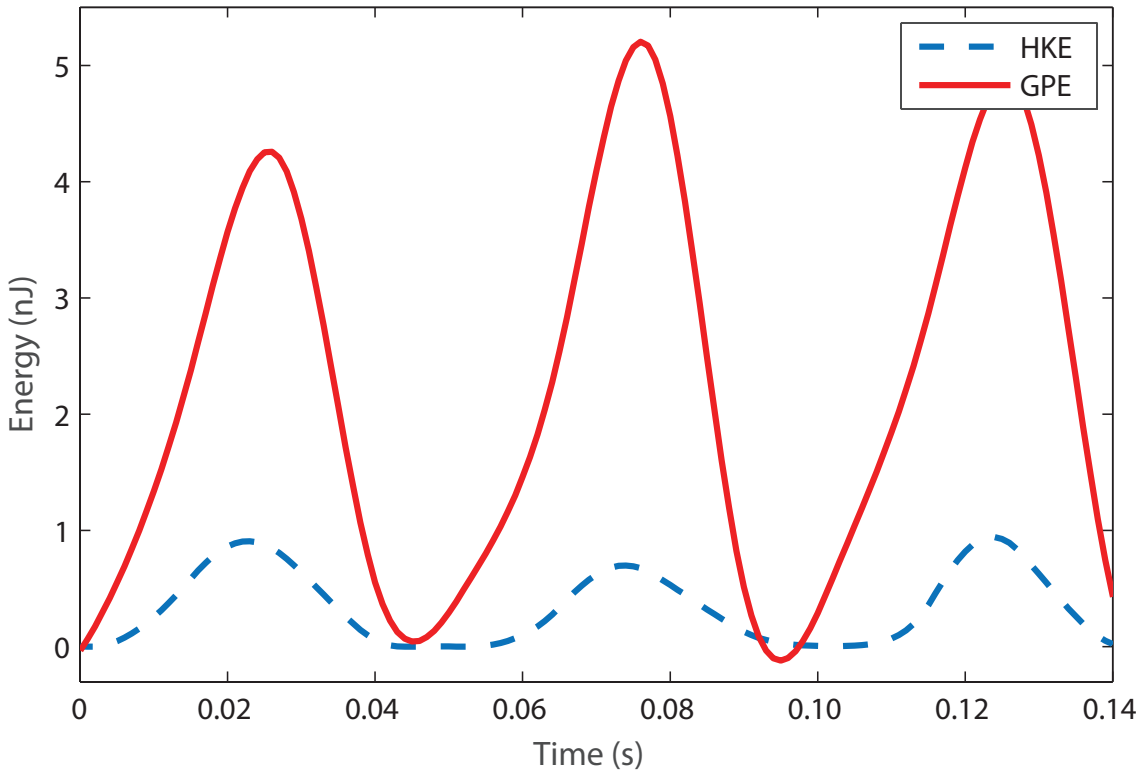

Figure 4.10: In-phase energy profiles of gravitational and kinetic energy of the robot pronking at 20 Hz.

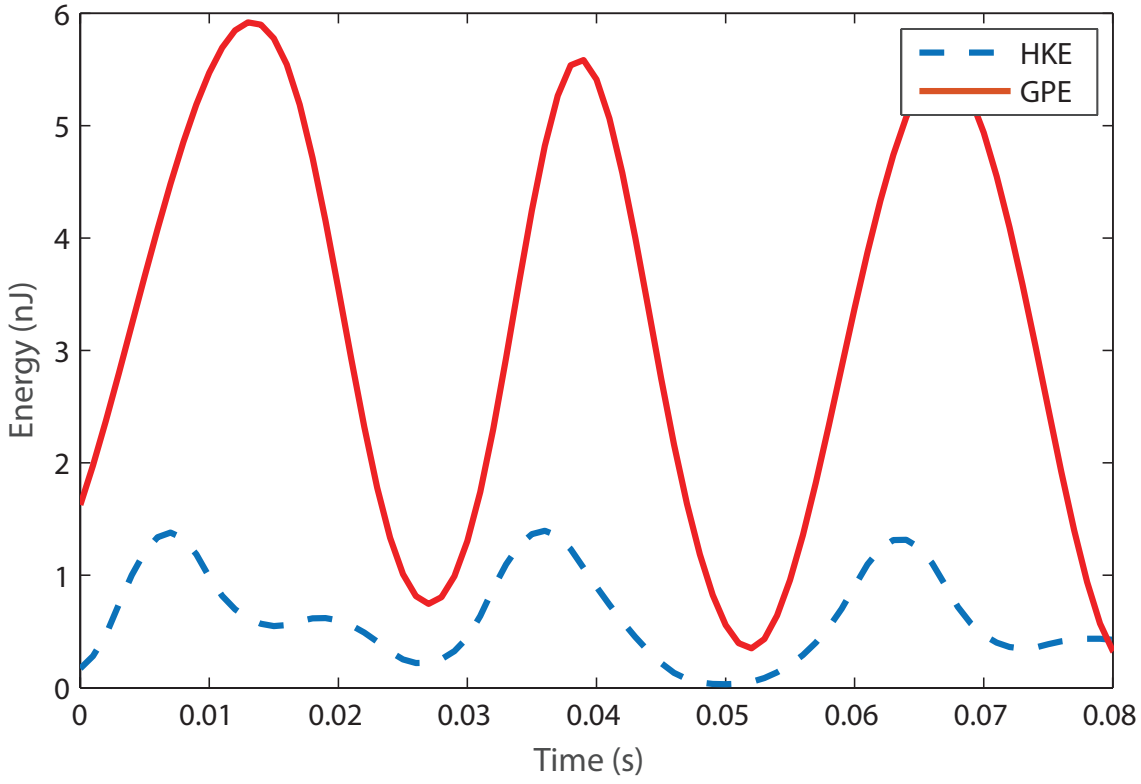

Figure 4.11: Energy profiles of the robot pronking at 35 Hz. In this trial, kinetic energy leads gravitational by 50°.

setup. with no signs of visible wear or decreased performance after over 1,000,000 cycles of actuation.

This work provides preliminary insight into locomotion at the milligram scale by exploring the energy profiles of the robot while running. While lower frequencies exhibit SLIP-like energy phasing, the mechanics of the system do not include elastic energy storage within the legs. As the robots move faster, the phasing of the gravitational and kinetic energies trend towards 180° out of phase, indicative of IP. However, the robot did not perform the prescribed pronking gait, making it unclear if the locomotion can be described with the IP model. Further work exploring ground contact and ground reaction forces can provide insight into the appropriate description of locomotion at the milligram scale.

Chapter 5

Mechanics of milligram-scale running

Insects are fast and agile runners. Ants, such as the desert ant (*Cataglyphis fortis*) run at speeds over 400 mm/s ($\approx$ 133 BL/s) with a body mass of around 10 mg [97]. To create similarly fast robots, it is important to understand the influencing factors that promote fast running in legged insects. Examining the morphology, kinematics, and ground reaction forces of ants builds an understanding of locomotion models for milligram-scale locomotion. Ultimately an understanding of the locomotion models promotes a greater understanding of ant biomechanics as well as an informed design and control approach for legged microrobots that can take advantage of passive dynamic properties.

Making ant-scale microrobotics (specifically, robots less than 100 mg in body mass) is an impressive feat in itself; these robots need to incorporate aspects of mechanical design, actuation, power, and control into a very small robotic system. Surveying existing robots shines light on important lessons in both biologically inspired locomotion as well as microrobotic locomotion. Robots, such as in [45, 35], use thermal expansion to drive the legs. However, the stride length in both of these robots was low, compared to their body lengths, ultimately decreasing their overall speed performance. Yasuda et al. created a robot structure with flexible linkages acting as spring-mass systems. The robot is driven by exciting the entire

structure using mechanical vibrations at the resonant frequency of the spring-mass systems [37]. Running at resonance is a strategy used in biological runners [6], and is important for legged locomotion at any scale. Hollar et al. demonstrated a legged robot using polysilicon hinges to rotate the legs [38]. While the robot did not walk forward, this demonstrated a robot moving autonomously. More recently, Qu et al. demonstrate lead zirconate titanate (PZT) actuated legged microrobots studying the ground contact at scales as low as 2.1 mg [42]. This work demonstrates the importance of ground contact to achieve forward propulsion in small-scale systems. Contreras et al. demonstrate a walking robot powered by electrostatic actuators [39], showing the capability of MEMS actuators to power milligram-scale walking. The robot presented by Vogtmann et al. incorporated elastic structures with magnetic actuation to demonstrate high velocity (over 5 body lengths per second) running. All of these robots are impressive in their own right, but understanding the locomotion dynamics at this scale will enable faster, dynamic microrobots from the identified design parameters.

The best data on ant locomotion dynamics was presented by Reinhardt et al. [14]. In this work, ground reaction forces were collected for a 20 mg ant, *Formica polyctena*, running over a force sensor. The kinematic data and ground reaction force suggest a SLIP-like running template, however, the ant lacks the distinct aerial phase seen in SLIP-like running. Apart from the aerial phase, the primary features of the SLIP template is the spring exchanging elastic potential energy for kinetic energy. While larger insects, such as cockroaches, have joint axes aligned vertically in the hind leg, serving as a passive elastic structure [71], it is unclear to what

extent the legs of ants act as elastic structures, either passively or actively. While there is resilin, an elastic protein [18], in the legs of ants, as legged runners are scaled down, the relative friction and viscosity within the leg joints increase [98]. By understanding the role of legs within milligram runners, addressing the passive and active contributions of the legs, and ultimately the mechanics of locomotion, fast and capable microrobots can be designed.

This chapter presents modifications to the robot presented in Chapter 4 enabling higher speed running. The locomotion of the robot is analyzed using high-speed video, extracting kinematic data. A force sensor is designed to capture the ground reaction force of the robot running. The experimentally captured data is brought together in a simple model, exploring the role of compliance within a torque-actuated SLIP model with a body mass of 1 mg.

5.1 Robot design and modifications

The robots used in this work are manufactured similarly to the robots presented in Chapter 4. However, the legs are molded separately as in Chapter 3. The mold for the legs is printed using the Nanoscribe on an ITO coated glass slide. The mold is printed with IP-S (Nanoscribe) photoresist using the DiLL mode. After printing, the part is developed in PGMEA for one hour followed by rinsing with IPA. The printed mold was silanized using vacuum deposition of trichlorosilane (Sigma-Aldrich, 448931) to prevent adhesion of the silicone to the printed mold.

In Chapter 3, robot legs made with MRTV outperformed other polymer molded

legs, considering both speed and stability as the two defining metrics. MRTV (MRTV9 Insulcast) is prepared by mixing 10 parts of the base agent to 1 part of the curing agent and mixed until thoroughly combined. Using a razor blade, the polymer is pushed into the mold and placed under vacuum to ensure minimal voids. The mold is placed on a hot plate at 100 °C for one hour.

When the robot legs were removed from the mold and attached to the robot, the robot could not move forward. It was also discovered that the petri dish, in which the robot was stored, could be inverted without the robot falling from the ceiling. Although the value needed is not known, the torque required to overcome the 'stickiness' of the polymer legs could not be provided by the two-axis coil system. To reduce the stickiness, the robot legs were legs were put in an oxygen plasma (Photo-14 Barrel resist stripper Branson) at 30 W for 7 minutes to create a silicon oxide layer on the back of the legs to reduce the adhesion, according to the recipe in [99].

5.2 Ground reaction force sensing

The measurement of micro-scale forces is largely done through elastic structures with different physical principles such as piezoresistive [100, 101, 102], magnetic [103], optical [104, 105], and capacitive [106, 107, 108]. Strain in elastic structures can also be measured through strain gauges, such as in [109, 110, 111], and related back to an applied force. However, integrating force sensing within an alternating magnetic field poses additional challenges in measurement because many transduction

methods are affected by an alternating magnetic field. Vision-based force sensing is largely unaffected by alternating magnetic fields. Vision-based force sensing has been integrated into control loops of microgrippers, adjusting force and position feedback in [112]. In [113] a two-dimensional, vision-based force sensor is designed for micro-assembly. More recently, a flexural structure was printed using direct laser writing on a Nanoscribe system to provide vision-based force sensing within a scanning electron microscope [114].

5.2.1 Design and fabrication

The force sensor is designed by concatenating cantilever beam elements in series and mirroring the overall design, adding two linkages in parallel. The design and analysis of this technique is described in [115, 116, 117]. In this work, only one type of building block is used in designing the force sensor. Each building block element is a cantilever beam, assuming one grounded end and one free end, capable of deflecting in x, y, and θ. The compliance matrix for a single cantilever beam is

$$C = \begin{bmatrix} \frac{L}{EA} & 0 & 0 \\ 0 & \frac{L^3}{3EI} & \frac{L^2}{2EI} \\ 0 & \frac{L^2}{2EI} & \frac{L}{EI} \end{bmatrix} \tag{5.1}$$

where L is the length of the cantilever beam element, E is the modulus, A is the cross sectional area, and I is the area moment of inertia. Each beam can be rotated

by some arbitrary angle, ψ, counter-clockwise by the matrix R,

$$R = \begin{bmatrix} \cos\psi & -\sin\psi & 0 \\ \sin\psi & \cos\psi & 0 \\ 0 & 0 & 1 \end{bmatrix} \tag{5.2}$$

and the rotated compliance matrix C' is

$$C' = R^T C R. \tag{5.3}$$

Each beam building block can vary in length, L, and angle, ψ. When two elements are placed together in serial, the resultant compliance matrix, $C_{resultant}$, of two beams, n and $n-1$ is [116]

$$C_{resultant} = C'_n + T^T C_{n-1} T \tag{5.4}$$

where

$$T = \begin{bmatrix} 1 & 0 & 0 \\ 0 & 1 & 0 \\ l_r \sin\zeta & l_r \cos\zeta & 1 \end{bmatrix} \tag{5.5}$$

and l_r and ζ are the length and orientation from the input of the first element to the second. In this case, using cantilever beam building blocks, l_r is equal to L and ζ is the supplementary angle of the design parameter ψ.

In the design of compliant mechanisms, the center of elasticity (also called the center of compliance or the elastic center [117]) is the point on a compliant mechanism where the spring constants are decoupled, or rather the compliance or stiffness matrices evaluated at this point are diagonal.

The vector from the input of the compliant mechanism to the center of elasticity can be found by calculating the magnitude and orientation of the vector. The magnitude of that vector, r_e, is [116]

$$r_e = \frac{\sqrt{C_{13}^2 + C_{23}^2}}{C_{33}} \tag{5.6}$$

where the subscripts on C denote the entry in the 3×3 tensor. The tangent of the orientation can be found by

$$\tan \beta = \frac{-C_{13}}{C_{23}}. \tag{5.7}$$

To design a low-stiffness and balanced spring system, a genetic algorithm in MATLAB was used to minimize the cost function,

$$\left(\frac{k_x}{k_y} - 1\right)^2 + \left(\frac{k_y}{k_x} - 1\right)^2 + \left(\frac{k_x}{k_s} - 1\right)^2 + \left(\frac{k_y}{k_s} - 1\right)^2 \tag{5.8}$$

where k_x and k_y are the spring constants in the horizontal and vertical directions, evaluated at the center of elasticity. While, k_s is the goal spring constant. One half of the linkage system was designed with the genetic algorithm and mirrored when the part was drafted in a CAD program (SolidWorks). In this optimization, fifteen building blocks are concatenated, with the length and orientation allowed to vary, and a goal spring constant, k_s, of 0.10 N/m for half of the sensor, 0.20 N/m for the completed design. The final design is shown in Figure 5.1 with a simulated spring constant of 0.31 N/m in both the x and y direction. The calculated natural frequency of the sensor ($f = \frac{1}{2\pi}\sqrt{\frac{k}{m}}$) is 151 Hz based on a calculated mass of the center piece of 0.31 mg estimated from the volume in SolidWorks and the density of SU-8 as 1.20 g/cm^3.

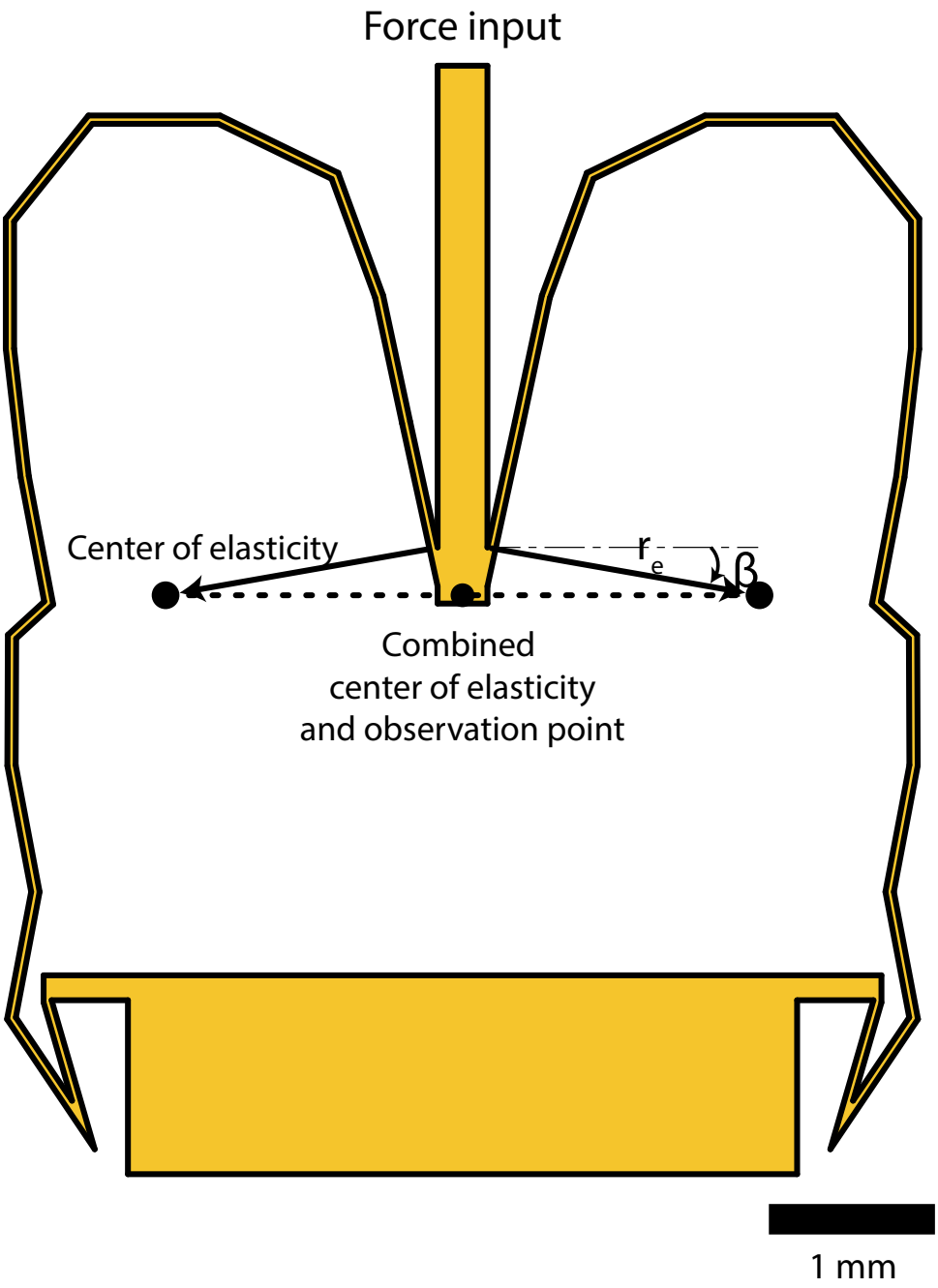

Figure 5.1: A solid model of the genetic algorithm designed force sensor. The input force and center of elasticity are connected through a rigid link. The deflection of the force sensor is observed at the center of elasticity.

5.2.2 Calibration

The vertical spring constant of the printed device was calibrated by contact-mode atomic force microscopy (MFP-3D Infinity AFM, Asylum Research), similar to [113]. In this mode, the AFM cantilever tip contacts the device while the base is translated downward. The translation of the cantilever deflects the device, which pushes back on the AFM cantilever beam, resulting in a deflection of the AFM beam. Measuring the deflection of the AFM cantilever beam and translation of the base of the cantilever beam enables the calculation of the device spring constant by

$$k_{AFM}\delta = k_{device}(\Delta\delta - \Delta z). \tag{5.9}$$

where k_{AFM} is the spring constant of the AFM cantilever, δ is the measured deflection of the cantilever, and z is the downward translation of the AFM cantilever. The changes in the deflection and z travel of the AFM cantilever beam is a result of the device pushing back on the cantilever beam. The device spring constant is found by the balanced force applied by the AFM cantilever to the spring force of the device applied to the AFM cantilever.

The device spring constant was measured with two different AFM cantilever beams (NanoAndMore USA). The spring constants of the AFM cantilever beams, calibrated by the thermal noise method [118], had spring constants of 7.72 N/m and 2.59 N/m. The device was pushed down 100 nm, 500 nm, and 1 μm, over three trials with each cantilever beam (18 total trials). The average vertical spring constant is calculated as 0.36±0.03 N/m, averaged over all trials. The natural frequency of the sensor is 162±7.39 Hz, using the calculated spring constant and calculated mass

from SolidWorks. This natural frequency is approximately five times larger than the actuation frequencies used in measuring the ground reaction forces, therefore the robot is unlikely to excite the resonance of the structure when walking over the force sensor.

While the horizontal spring constant could not be measured in a similar manner, the deflection of the force sensor in the horizontal direction is similar to the deflection in the vertical direction when a silicon cube is attached to the force input and the entire device is rotated to orient the horizontal axis of the device parallel to the direction of gravity. For the ground reaction force measurements, the horizontal spring constant is assumed to be equal. While this assumption may not be entirely supported by experimental results, this assumption enables the empirical observation of the phasing and shape of the ground reaction forces, which is still informative in model construction.

5.3 Experimental setup

The experimental setup is shown in Figure 5.2. The magnetic actuation scheme is the same as in Chapter 4. The printed force sensor is integrated into the 'ground', with a 500 μm × 500 μm × 500 μm silicon cube attached to the top of the device to increase the probability of the robot stepping on the sensor. The top of the silicon cube is flush with the rest of the ground. Two high-speed cameras are synced together to record the robot running. A top-down view of the robot is captured (Camera view 1, Photron AX100) with a macro lens (Zeiss Makro-Planar T* 2/100 mm ZF.2). A

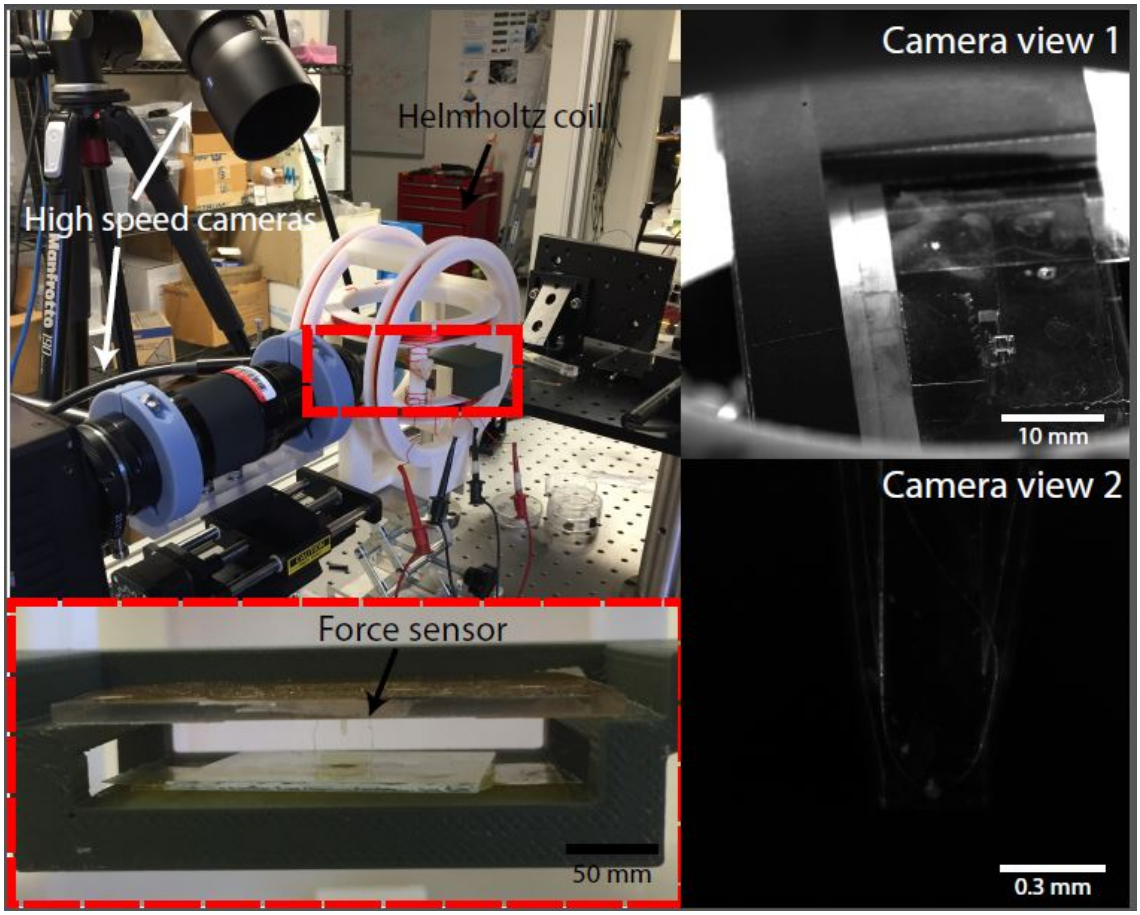

Figure 5.2: Experimental setup for measuring the ground reaction force. The first camera focuses on the robot from a top-down view, while the second camera images the force sensor.

side view focused on the force sensor is captured with a second high speed camera (Camera view 2, Photron UX100) equipped with microscope lens system (Model K1 CentriMax, Infinity) and 2.90X objective (MX-6, Edmund Optics). Both cameras recorded at 1,000 frames per second, the maximum attainable frame-rate given the light available in the confined circumstances of the force sensor, even with a fiber optic light source illuminating the sensor (SugarCUBE LED Illuminators, Edmund Optics).

5.4 Locomotion results

5.4.1 Velocity

Figure 5.3 shows the average horizontal velocity of the robot. The solid line and markers correspond to the average value, while the shaded area represents one standard deviation over 3 trials for a single robot. The maximum observed velocity of 120 mm/s (47.9 BL s^{-1}) occurred at 70 Hz. In general, the average speed saturates near 35 Hz at 78.6 mm/s despite increasing the stride frequency. Since this is an uncontrolled rotary system, the average stride length decreased with increasing stride frequency. The legs are rotating faster, making contact with the ground at a steeper touch-down angle, decreasing the actuated angle when in contact with the ground, and ultimately decreasing the stride length achievable by the robot.

5.4.2 Motion and energetics of the center of mass

The motion of the robot's center of mass, and the time derivatives, give insight into the locomotive profile of the robot, and ultimately the construction of a locomotion template. Figure 5.4 shows the motion of the center of mass of the robot actuated at 15 Hz, close to the frequency predicted by $1/2\pi\sqrt{g/l} \approx 18$ Hz. On average, the robot had a stride length of 2.48 mm with an average vertical deflection of 0.75 mm, similar to the length of the leg, hip to toe. In the vertical deflection, there is not a distinct downward deflection at the peak in the vertical deflection of center of mass, indicative of elastically loading the leg. It is possible that the robot wasn't dynamic enough and did not have an acceleration larger than gravity to load the leg. The

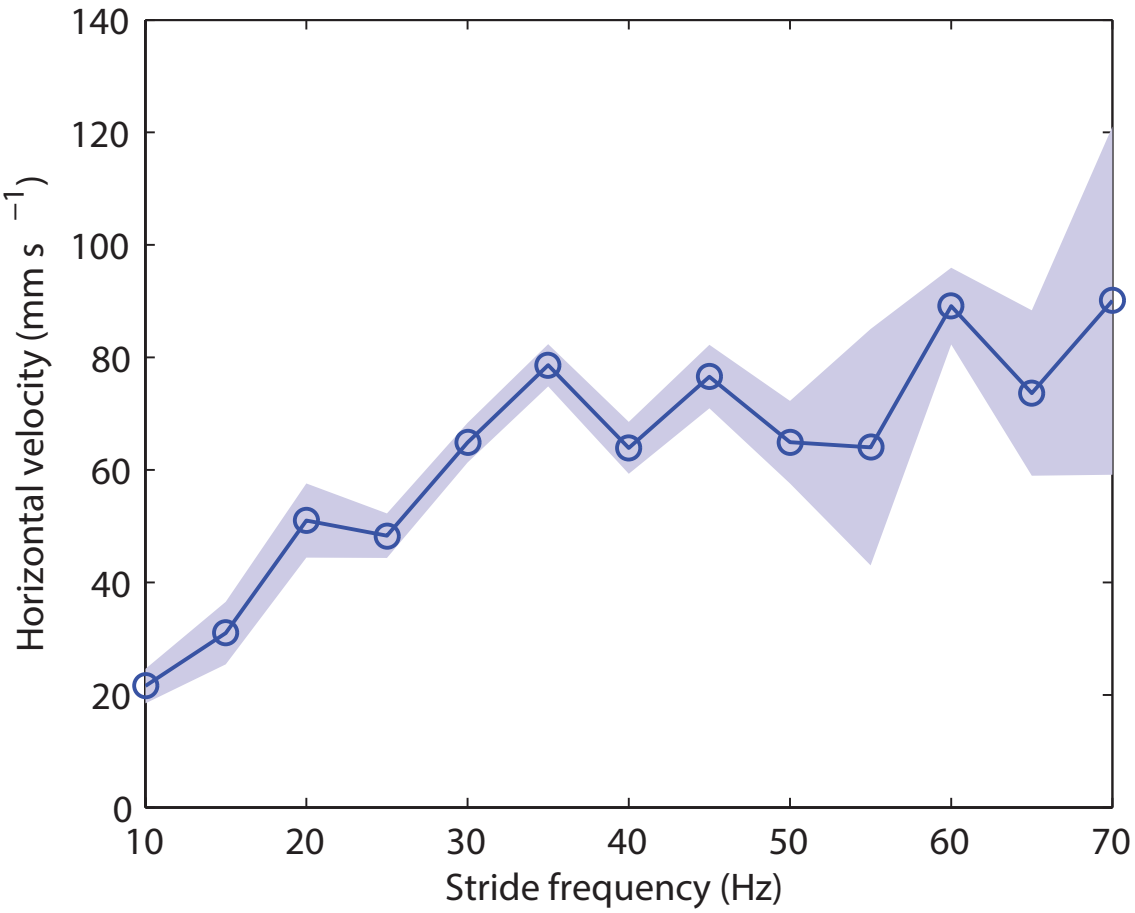

Figure 5.3: The average forward velocity (solid lines) and standard deviation (shaded area) over three trials of a robot actuated from 10 Hz to 70 Hz.

robot reached peak horizontal velocity of 50.7 mm/s with the velocity decreasing at mid-cycle of the gait. This is from both the design of the robot, as well as the actuation scheme and driving frequency. Since the legs are 180° out of phase and the actuation angle is less than a 180° sweep, there is a point where there is no leg in contact with the ground. The robot reached peak average vertical velocities of 53.7 mm/s at 21%, slightly before the peak in displacement. Peak horizontal accelerations of 7.10 m/s^{2}at 19.5%, 37.8° ahead of the peak velocity. Peak positive and negative vertical accelerations of 6.84 m/s^2 at 54% and 93.6 mm/s^2 correspond to body forces of 6.84 μN and 0.94 nN. The small downward acceleration shows a controlled descent of the center of mass back to the ground, rather than a ballistic phase with a free-fall accelerated by gravity.

Figure 5.5 shows the average position, velocity, and acceleration of the center of mass of the robot actuated at 35 Hz, close to the predicted scaled frequency of 33 Hz from [8] even including ant data from [119]. In a single gait cycle, the center of mass moves, on average, 2.16 mm forward, 13% less than the stride length of the robot at 15 Hz. The vertical component of the position of the center of mass vaulted, reaching an apex of 0.87 mm at the mid-gait cycle, higher than the leg length, indicting a small flight phase of the robot. However, there is not a clear indication of leg compression. At this driving frequency, the swing leg transitions to the stance leg prior to the body coming to a complete rest. The forward speed decreased at 50% of the gait cycle, this corresponds to the portion of the gait cycle where the sets of legs are transitioning their contact with the ground. The vertical velocity crosses 0 mm/s at the mid-cycle and continues to decrease until 75% of

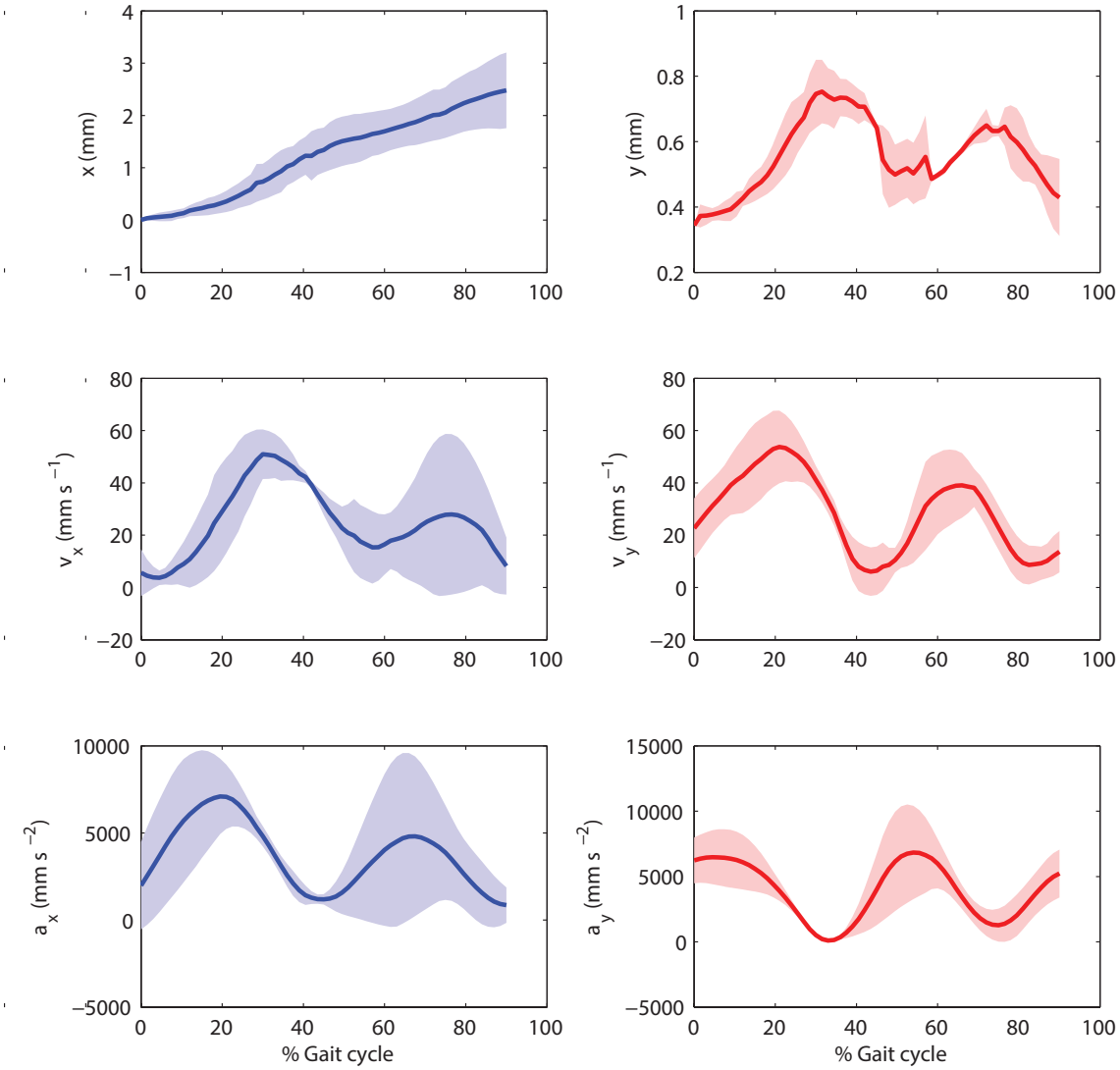

Figure 5.4: The position (top), velocity (middle), and acceleration (bottom) of the horizontal (left) and vertical (right) components of the center of mass of the robot actuated at 15 Hz.

the gait cycle. It is possible that there is some elastic energy stored within the legs, propelling the robot for the next cycle. At the mid-cycle the robot reached negative horizontal accelerations of 2.73 m/s^2, and negative vertical accelerations of 6.31 m/s^2, or 6.31 μN of force, enough to compress the legs, with a scaled spring constant of 7.50 N/m, 0.84 μm.

Comparing the center of mass profile of the robot to the center of mass profile of the ant,*Formica polycenta*, in [14], there are some distinct differences. The ant shows a lower center of mass at mid-stance, either due to passive compliance in the leg or through an active movement of the ant itself. The ant also shows an oscillatory vertical acceleration at the peak vertical position, possibly from an either passive or active response to maintain contact with the ground. The center of mass motion of the robot shows a stiff legged locomotion profile. While there are some distinct differences between the ant and robot, it is unclear, from the kinematics alone, if either profile is representative of the locomotion dynamics at the milligram-scale.

In addition to the kinematics, the energetics of the system are informative in determining a locomotion template. Figures 5.6 and 5.7 show the average horizontal kinetic and gravitational potential energies of the robot actuated at 15 Hz and 35 Hz respectively. The horizontal kinetic energy is calculated as

$$HKE = \frac{1}{2}m\dot{x}^2 \tag{5.10}$$

where m is the mass of the robot and $\dot{x}$ is the horizontal velocity. The gravitational energy is calculated as

$$GPE = mgh \tag{5.11}$$

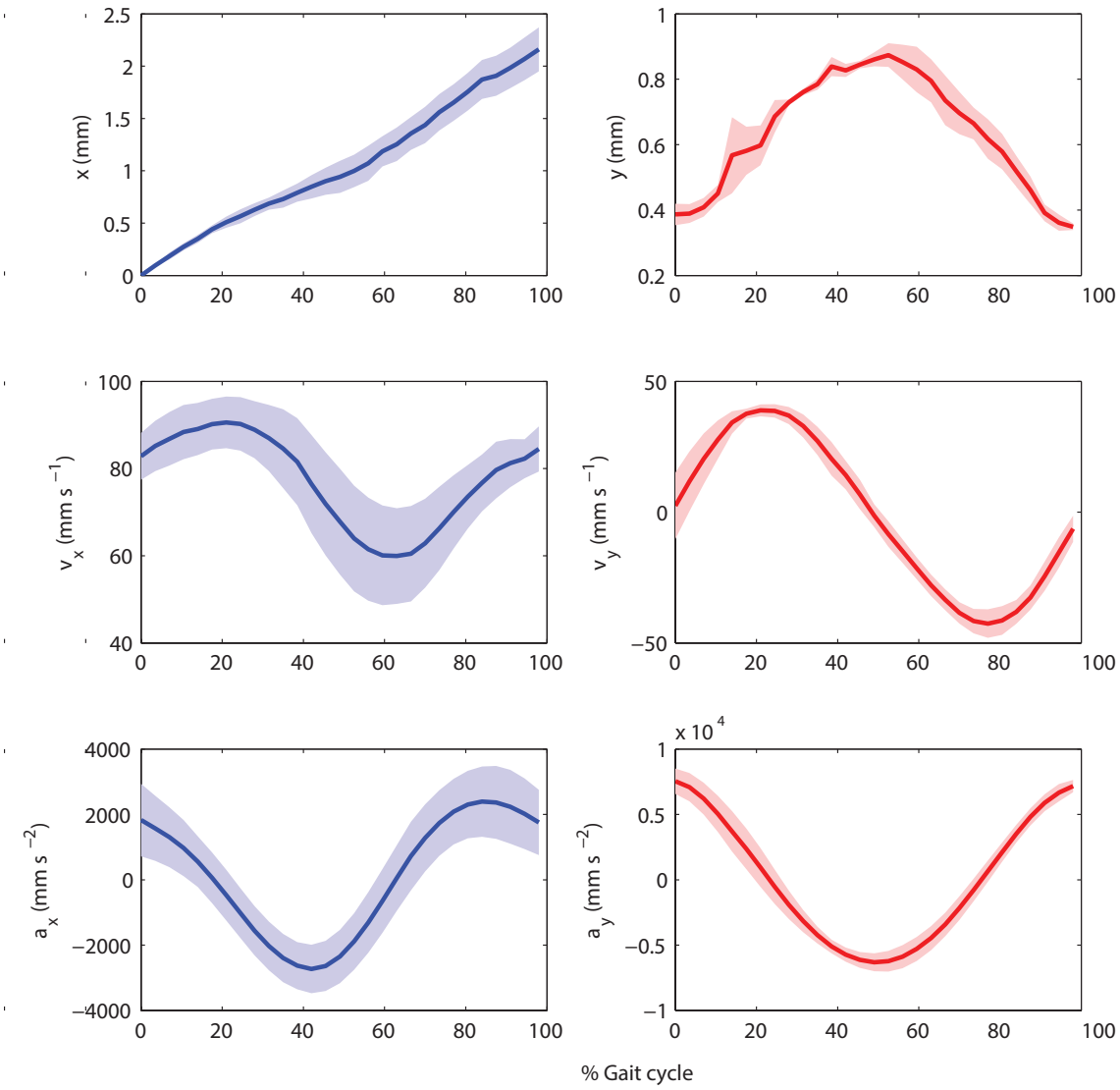

Figure 5.5: The position (top), velocity (middle), and acceleration (bottom) of the horizontal (left) and vertical (right) components of the center of mass of the robot actuated at 15 Hz.

where g is the acceleration of gravity (9.81 m/s^2) and h is the distance the center of mass is elevated above the ground. In Figure 5.6, the horizontal kinetic energy is in-phase with the gravitational energy. On average the kinetic energy leads the gravitational energy by 5.40° when the robot is actuated at 15 Hz. At 35 Hz , kinetic energy leads gravitational energy by 113°(Figure 5.7). While this energy phasing exists between SLIP and IP, where the expected phasing is 0° and 180°, respectively. Slipping in the ground contact would contribute to deviations from the ideal phasing. Examining the energy phasing alone does not conclusively indicate a locomotion template.

5.4.3 Congruity and recovery

The synchronization and exchange of gravitational potential energy and horizontal kinetic energy is quantified by the metrics congruity and recovery. Congruity is a metric quantifying the synchronization of the change in kinetic and gravitational energies [120]. Percent congruity is defined as the portion of the cycle when the kinetic and gravitational energies change similarly. An idealized model of SLIP corresponds to a percent congruity of 100%, while the IP model corresponds to 0% congruity. Figure 5.8 shows the calculated percent congruity as a function of frequency. The marker represents the average percent congruity calculated over three trials, while the shaded area represents one standard deviation. The percent congruity remains constant, between 50% and 55%, as frequency is increased. A Pearson linear correlation coefficient shows no significant correlation between percent congruity and

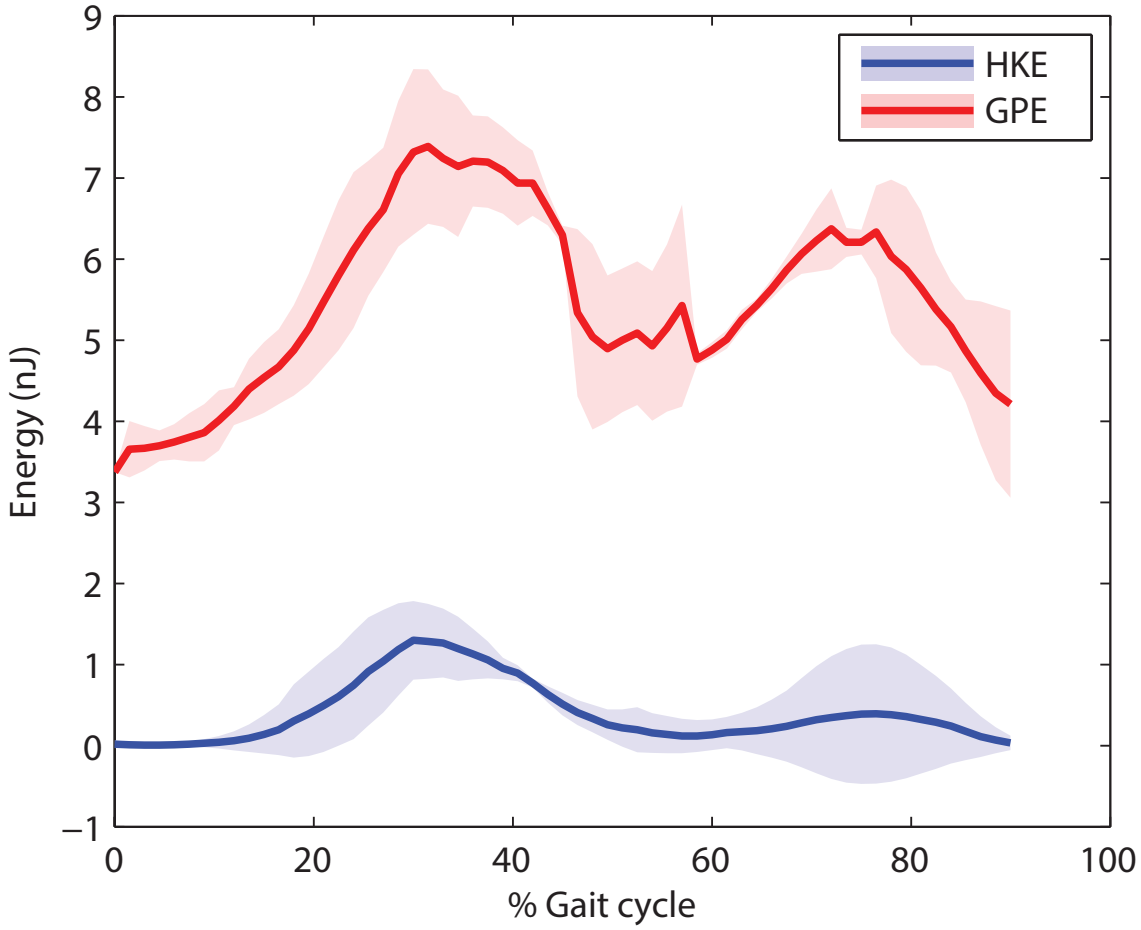

Figure 5.6: The average horizontal kinetic energy (blue) and gravitational potential energy (red) over a gait cycle of the robot actuated at 15 Hz.

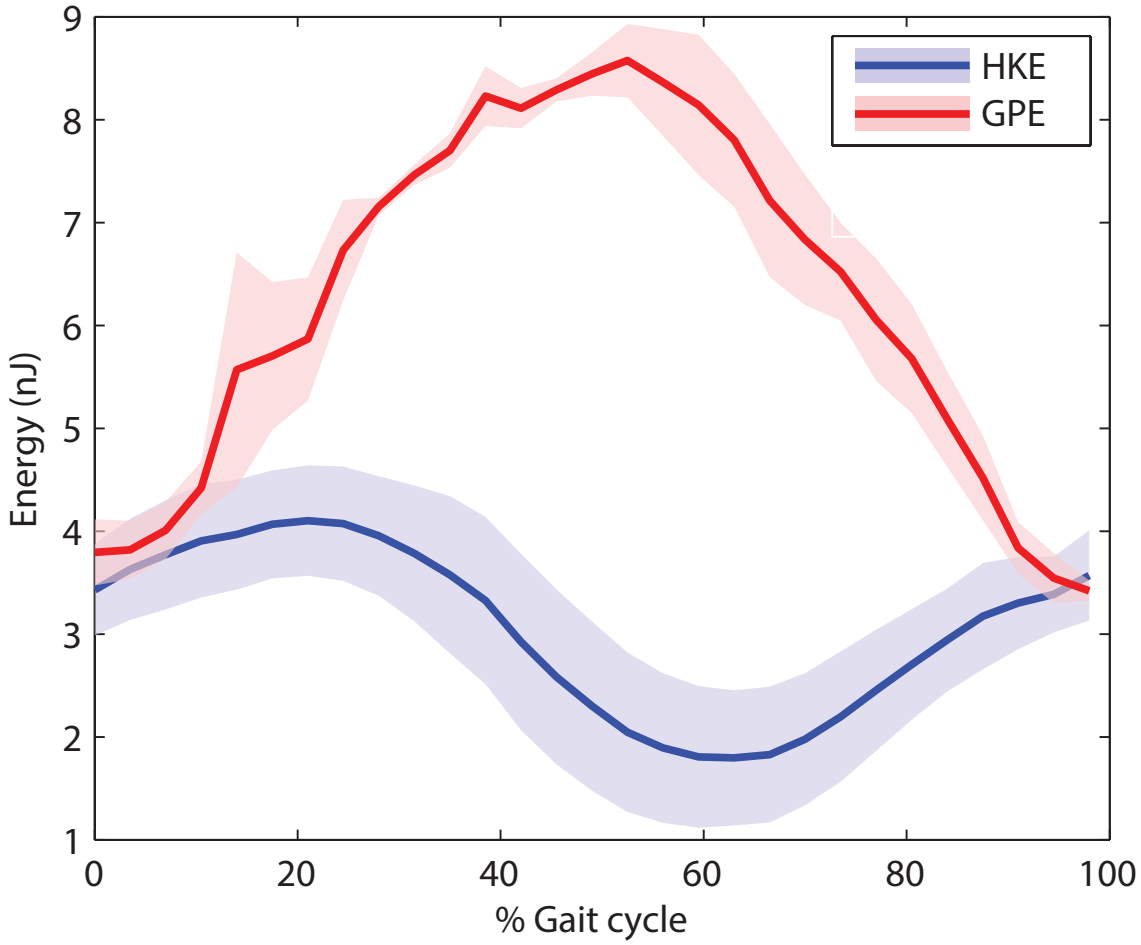

Figure 5.7: The average horizontal kinetic energy (blue) and gravitational potential energy (red) over a gait cycle of the robot actuated at 35 Hz.

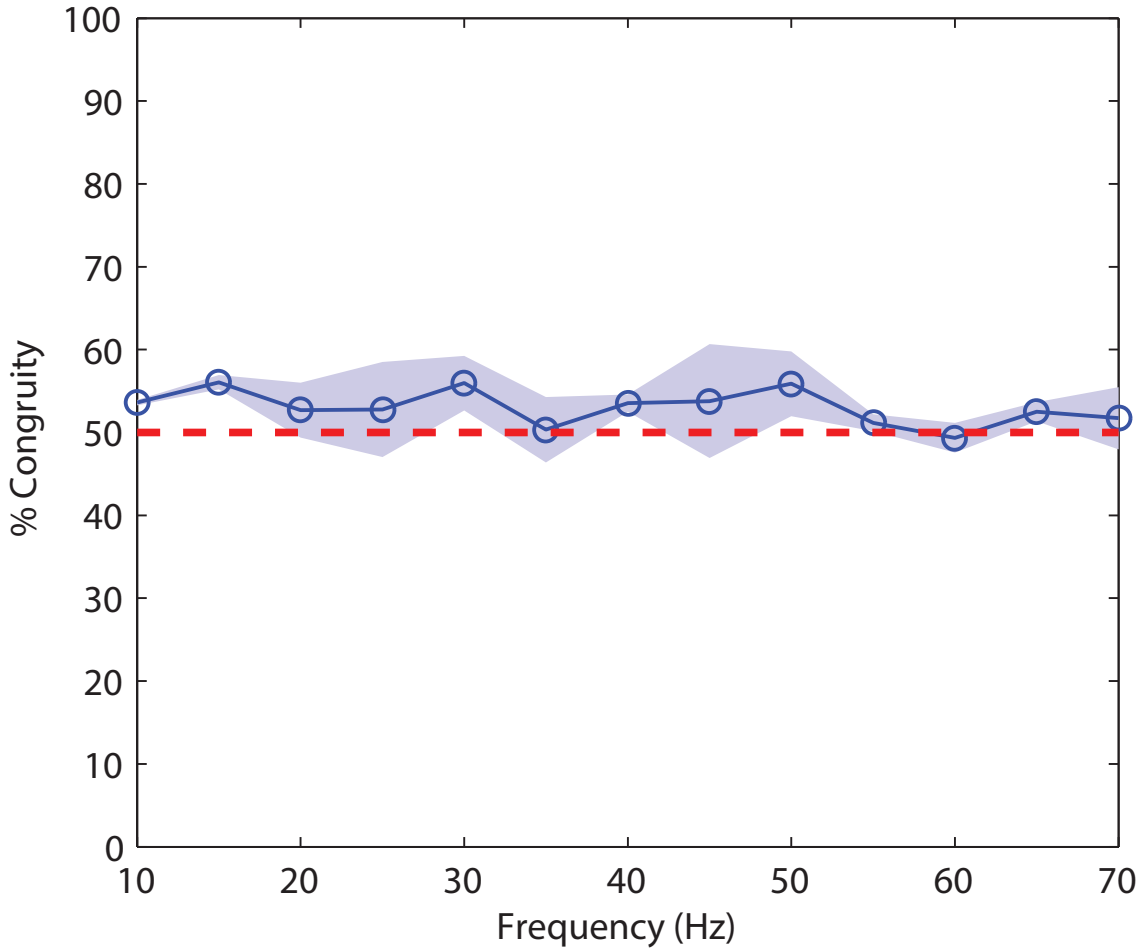

Figure 5.8: Calculated percentage congruity of the robot actuated from 10 Hz to 70 Hz. The marker represents the average value, with the shaded area representing one standard deviation over three trials with one robot

frequency, $r = -0.26$ with a p-value of $p = 0.22$. While congruity percentages are affected by slipped ground contact, the mid-value congruity percentage, calculated from the experimental trials does not clarify the behavior of the system; whether the robot is running, like SLIP, versus walking, like IP.

Recovery defines the amount of energy recovered between the kinetic and po-

tential energies. Recovery is defined as

$$recovery = \frac{\Sigma\Delta E_K + \Sigma\Delta E_P + \Sigma\Delta E_{COM}}{\Sigma\Delta E_K + \Sigma\Delta E_P} \tag{5.12}$$

where $\Sigma\Delta E_K$, $\Sigma\Delta E_P$, and $\Sigma\Delta E_{COM}$ are the sums of the positive changes in the kinetic, potential, and total energy ($E_{COM} = E_K + E_P$) of the center of mass [52]. An ideal inverted pendulum system would have an energy recovery of 100%, where all of the energy is exchanged conservatively between the kinetic energy and gravitational potential energy. While, the SLIP running model with elastic energy exchange, corresponds to a recovery value of 0%.

Figure 5.9 shows recovery percentage as a function of frequency. The robot maintains low recovery percentages, between 10% and 20%, across the frequency range. There is no significant correlation between frequency and the recovery percentage, $r = 0.21$ with a p-value of $p = 0.30$. Low recovery values indicate that the locomotion is not dependent on the exchange between gravitational and kinetic energy.

Considering the percentage values for both congruity and recovery show two competing factors in the locomotion. The low recovery values show that locomotion is not driven by inertial forces, consistent with the low mass of the robot (1 mg). However, the congruity percentage, quantifying the synchronization of the energies, shows that the gravitational and kinetic energies are not always synchronized. While the recovery metric builds towards a SLIP mode, the congruity metric identifies that the locomotion profile is not the same as the classical passive SLIP model as in [6].

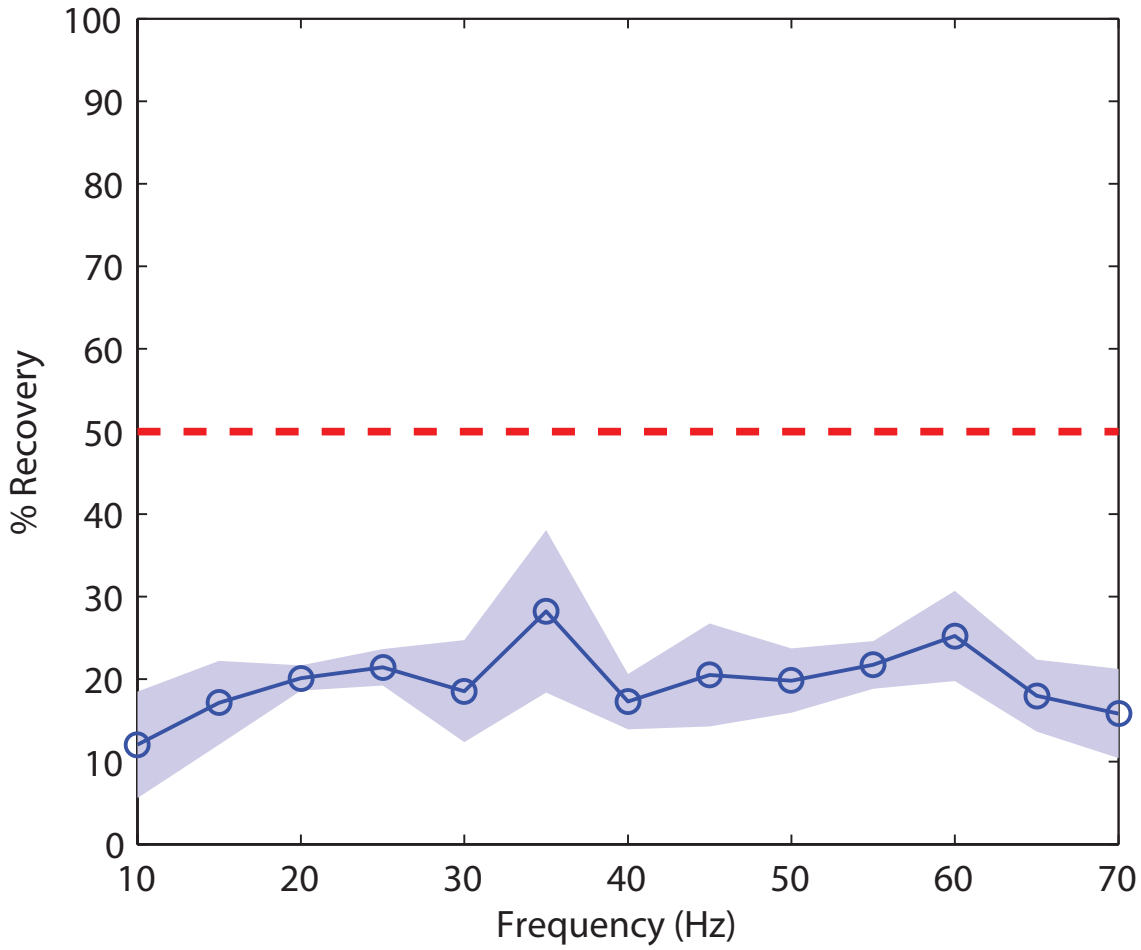

Figure 5.9: Calculated percentage recovery of the robot actuated from 10 Hz to 70 Hz. The marker represents the average value, with the shaded area representing one standard deviation over three trials with one robot.

5.4.4 Ground reaction force

The ground reaction force is calculated by filming the force sensor, described in Section 5.2.1, using the experimental setup described in Section 5.3. The optics used provide a resolution of 0.38 μm/pixel. Using the spring constant calculated through AFM, the vision-based force resolution is 0.96 μN/pixel. The force resolution is ultimately dependent upon the pixel tracking algorithms, which are are capable of sub-pixel resolution, such as tracking fluorescence [121] and cell features [122]. The exact algorithm used in the markerless tracking software (TEMA ImageSystems) is not explicitly known. However, tracking the center of elasticity of the force sensor under normal experimental conditions, but without the robot walking over the sensor, shows a standard deviation in the horizontal and vertical directions of 0.02 pixels and 0.01 pixels, over 200 frames of the sensor at a fixed point.

While the magnitude of force depends upon the tracking algorithm to determine forces below 0.96 μN/pixel, the approximate magnitude and phasing of the forces is informative in understanding the dynamics of the locomotion of the robot. Figure 5.10 shows the average ground reaction force and smoothing spline, averaged over three trials, on a single leg of one step of the robot actuated at 15 Hz. The vertical ground reaction force reaches a peak force of 5.69 μN at 28% of the gait cycle, this is the point where one leg is directly under the body. The robot is walking with a trotting gait, meaning two legs are synchronized, that total ground reaction force on the robot is 11.4 μN (1.16X the body weight). At this point, the horizontal ground reaction force reaches a peak negative force of 2.61 μN, 0.13x

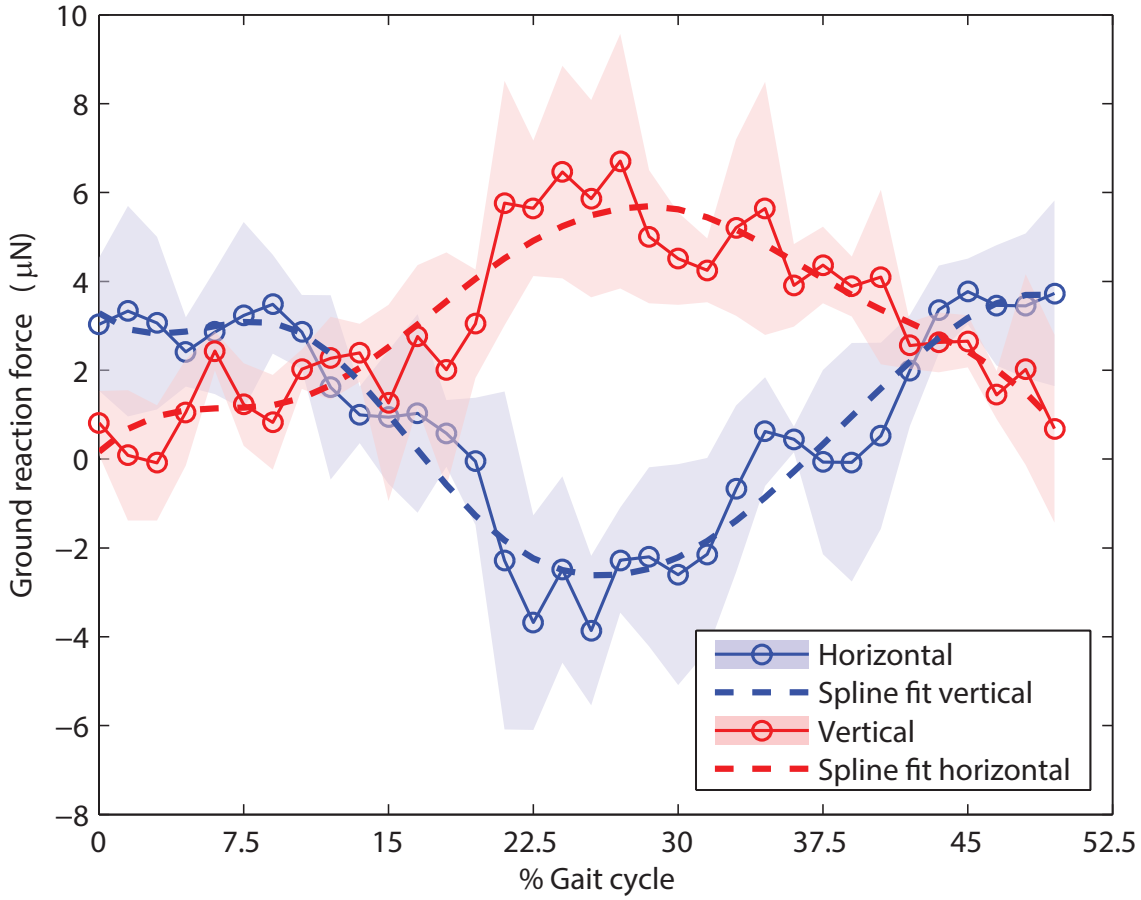

Figure 5.10: Calculated ground reaction force on one leg of one robot actuated at 15 Hz averaged over three trials.

times the maximum torque divided by the leg length. The SLIP template predicts that the vertical force leads the horizontal force by 90° [6]. Using the peaks of the smoothing splines, the Vertical force leads the horizontal by 79°. The foot slipping against the ground contributes both to the noise in the force reading as well as the phasing difference between the vertical and horizontal forces.

Figure 5.11 shows the average ground reaction force on a leg of one step of the robot actuated at 35 Hz. At 14% of the gait cycle, the robot produces a peak vertical ground reaction force around 5.34 μN(1.08X the body weight) and -1.56 μN hori-

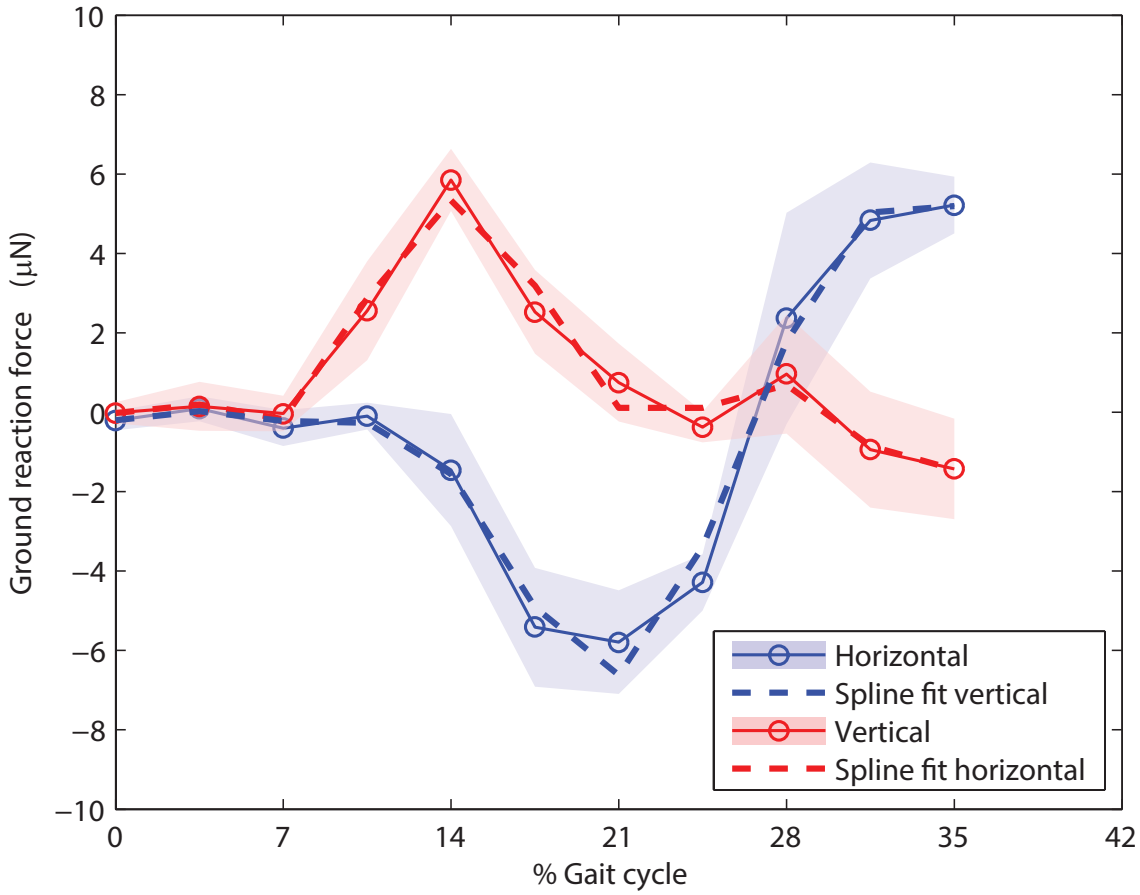

Figure 5.11: Calculated ground reaction force on one leg of one robot actuated at 35 Hz averaged over three trials.

zontally. The peak negative horizontal force of 6.62 μN (0.33X of τ_{max}/l) occurs at 21% of the gait cycle. The peaks of the smoothing spline show a relative phasing of 75° where the vertical force leads the horizontal force. Overall, the noise on the force sensor is decreased in comparison to the 15 Hz data. The data is recorded at the same frame rate of 1,000 fps, therefore the ground reaction force of the robot running at 35 Hz data has 30% of the data points as the 15 Hz data, missing some of the noise generated by the slipped ground contact. Ultimately, the phasing in the two datasets indicate a SLIP-like behavior of the robot locomotion.

5.5 Torque-driven grounded SLIP model

Given the actuation scheme of the robots, their low aerial phases, and insights from biological data in [14, 13] showing a complete absence of an aerial phase in ant, a torque-driven grounded SLIP running model was compared to the experimental kinematic, energy phasing, and ground reaction force data. The torque-driven SLIP model uses the same stance equations as used in Chapter 3, expressed in polar coordinates as

$$\begin{cases} \ddot{\zeta} = \zeta\dot{\psi}^2 - g\sin\psi - \frac{k}{m}(\zeta - l) \\ \ddot{\psi} = -\frac{2\dot{\zeta}\dot{\psi}}{\zeta} - \frac{g\cos\psi}{\zeta} + \frac{\tau}{m\zeta^2} \end{cases} \tag{5.13}$$

where ζ is the length of the spring leg, ψ is the angle that the leg has rotated, g is the acceleration of gravity (9.81 m/s^2), and m is the mass (1 mg). A notable difference between the equations presented here and in Chapter 3 is the absence of a damping term. While damping is beneficial for high-speed running and is dominant at small size scales [98], the main goal of this section is simply to compare the model to experimental behavior.

5.5.1 Simulation motion and energetics of the center of mass

To simplify the simulation environment, the differential equations were integrated numerically using the forward Euler method and a fixed time step of 10 µs. The mechanics of the legs were assumed to be similar to that of a curved beam with a spring constant of $k = \frac{2AEe}{\pi R}$ where $A \propto L^2$, $e \propto L^1$, and $R \propto L^1$, therefore $k \propto L^1$. The spring constant used in the simulation is 7.50 N/m, obtained from the same

spring constant for MRTV as in Chapter 3 scaled down a factor of 8 to account for the isometric scaling of the robot, and multiplied by a factor of 2 to account for trotting gait, which has two legs on the ground.

The motion of the center of mass with a driving frequency of 15 Hz is shown in Figure 5.12. The horizontal and vertical position of the center of mass agree with the experimental values, shown in Figure 5.4, showing a stride length of 2.82 mm and a maximum vertical deflection of 0.71 mm. The simulation showed peak horizontal velocities of 118 mm/s, 2.3 times larger than the experimental values, and peak vertical velocities of 72.9 mm/s, 1.3 times larger than the experimental values. The phasing of the peak velocities is consistent with the experimental results, showing a peak horizontal velocity around 25% and 75% of the gait cycle and peak vertical velocities at 14% and 64% of the gait cycle. The simulated peak horizontal accelerations of 16.5 m/s^2 are 2.3 times larger than experimental values, while the vertical accelerations show only negative accelerations up to 19.8 m/s^2. The higher horizontal velocity and acceleration in simulation can be attributed to the simulation not considering slipping of the foot against the ground, which decreases forward velocity in practice. The absence of distinct positive vertical accelerations and large negative accelerations come from the fact that detachment from the ground is not allowed in this model. The mass is driven to the ground under the influence of the torque as well as gravity after the peak vertical position. In practice, the robot is not stuck to the ground during actuation, and generally falls back to the ground after the peak vertical position.

The simulated energy profiles, the horizontal kinetic energy and gravitational

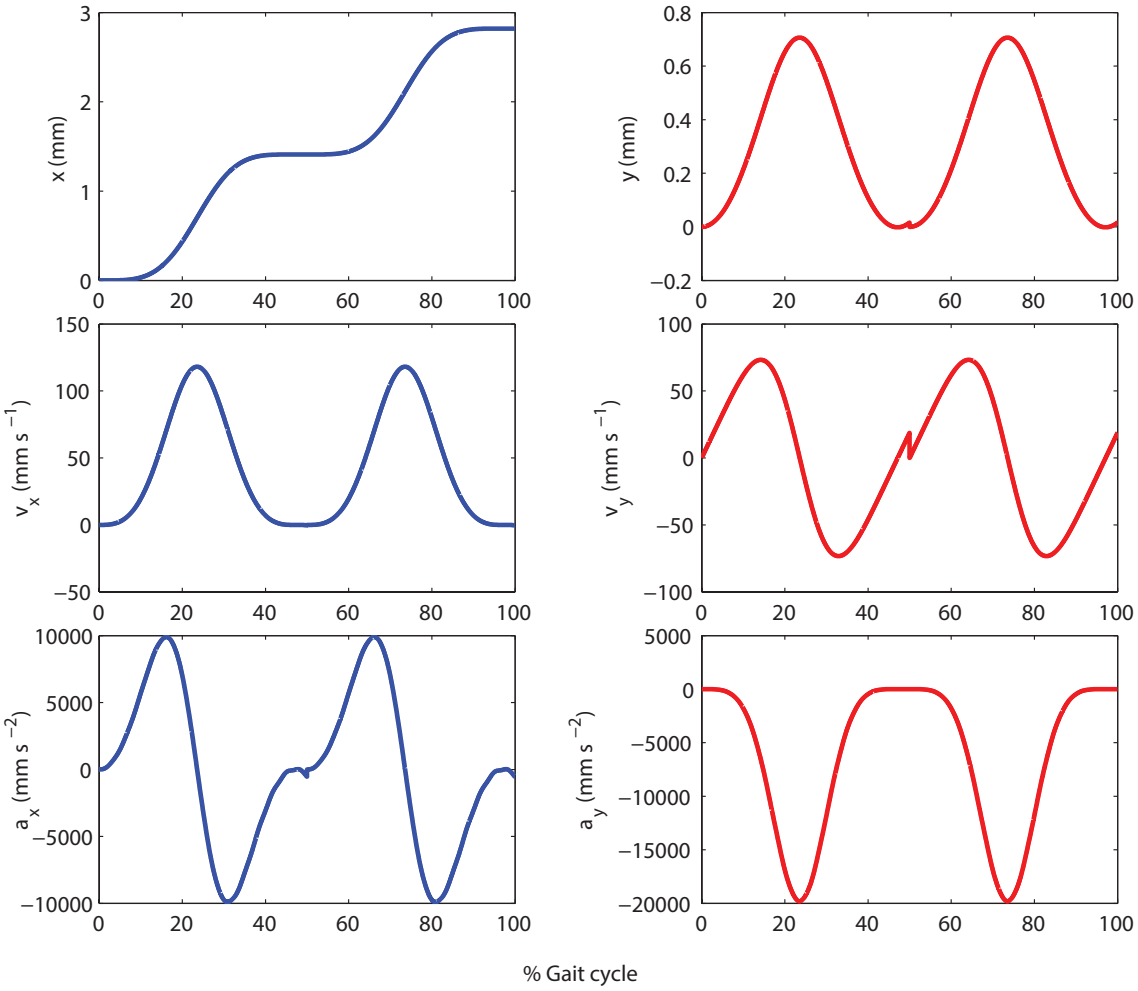

Figure 5.12: Simulated horizontal (blue) and vertical (red) position, velocity, and acceleration of the center of mass of a torque-driven grounded SLIP model driven at 15 Hz.

potential energy, are shown in Figure 5.13. The two energies are distinctly in-phase with one other, showing that a grounded torque-driven system behaves energetically similar to traditional SLIP-like running. The gravitational potential energy reaches similar peak values around 7 nJ, as compared to the experimental plot (Figure 5.6). The simulated horizontal kinetic energy reaches peak values around 7 nJ, 5.3, or roughly 2.3^2, times higher than experimental value. From the energy profile, congruity and recovery are calculated to be 97% and 1.2%, respectively. The congruity and recovery percentage values coincide with the expected values for a SLIP-like running system.

The energy profiles and recovery percentage show locomotion that does not rely on the exchange of gravitational and kinetic energy, consistent with experimental data. However, the congruity percentage is higher than experimentally determined values. This is largely from the simulation condition where the foot is not allowed to slip. If the ground contact could slip, the congruity percentage would decrease. However, when comparing the center of mass profile along with the recovery percentage and energy phase, to the experimental results, the simulated model approximates the behavior of the robot.

5.5.2 Simulation ground reaction force

Figure 5.14 shows the simulated ground reaction force for one leg. The peak vertical ground reaction force of 4.95 μN(9.90 μN or 1.01X BW) occurs at 24% of the gait cycle. The force magnitude and location during the gait cycle is consistent with the

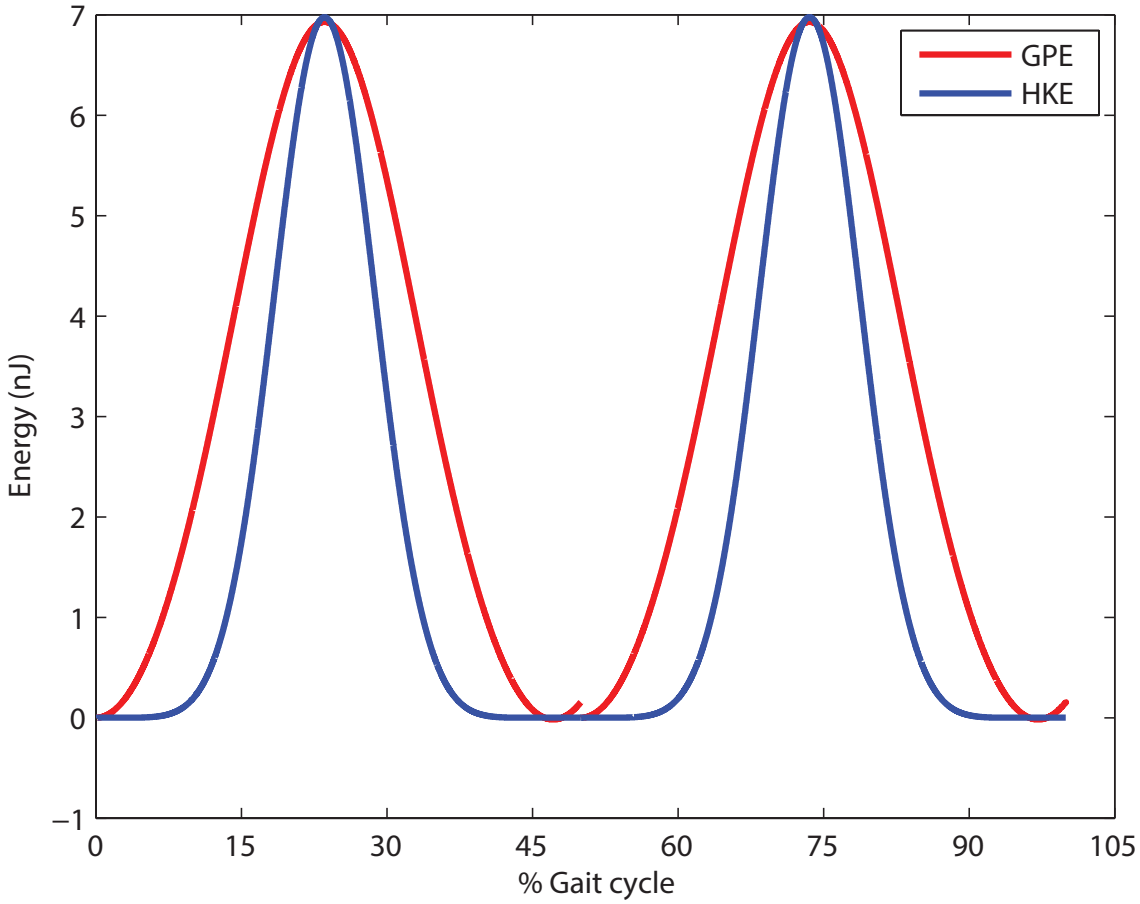

Figure 5.13: Simulated horizontal kinetic energy (blue) and gravitational potential energy (red) of the center of mass of a torque-driven grounded SLIP model driven at 15 Hz.

experimental ground reaction force, shown in Figure 5.10. The magnitude of the simulated horizontal ground reaction force shows a peak of 2.47 μN, compared with a magnitude of 2.61 μN calculated experimentally. The main difference between the simulated and experimentally captured ground reaction force is the location of the peak of the horizontal ground reaction force. In the experimental work, the negative and positive peak occur at 25% and 50% of the gait cycle. While in simulation, the negative and positive peaks occur at 16% and 31%. In simulation, the vertical and horizontal ground reaction forces are out of phase by 29°.

The differences between the leg architecture and ground contact between the experimental system and simulation could explain the difference between the location of the peaks of the experimental and simulated horizontal ground reaction force. Slipping of the foot against the ground would delay the peak of the horizontal force, since force is not being maximally applied during slippage. In simulation, the contact of the foot to the ground is treated as a permanent pin joint during the entire stride cycle. This is not consistent with the experimental setup. In the experiments, the foot loses contact with the ground roughly 10° after the leg is completely under the robot. In simulation, the contact is maintained through the entire stride cycle.

5.5.3 Model-based insights

While a torque-driven grounded SLIP model fits well with the robot data, the real utility of this model comes from insights into design, and ultimately control, of small-scale robots. One notable effect missing in both experimental results and simulation

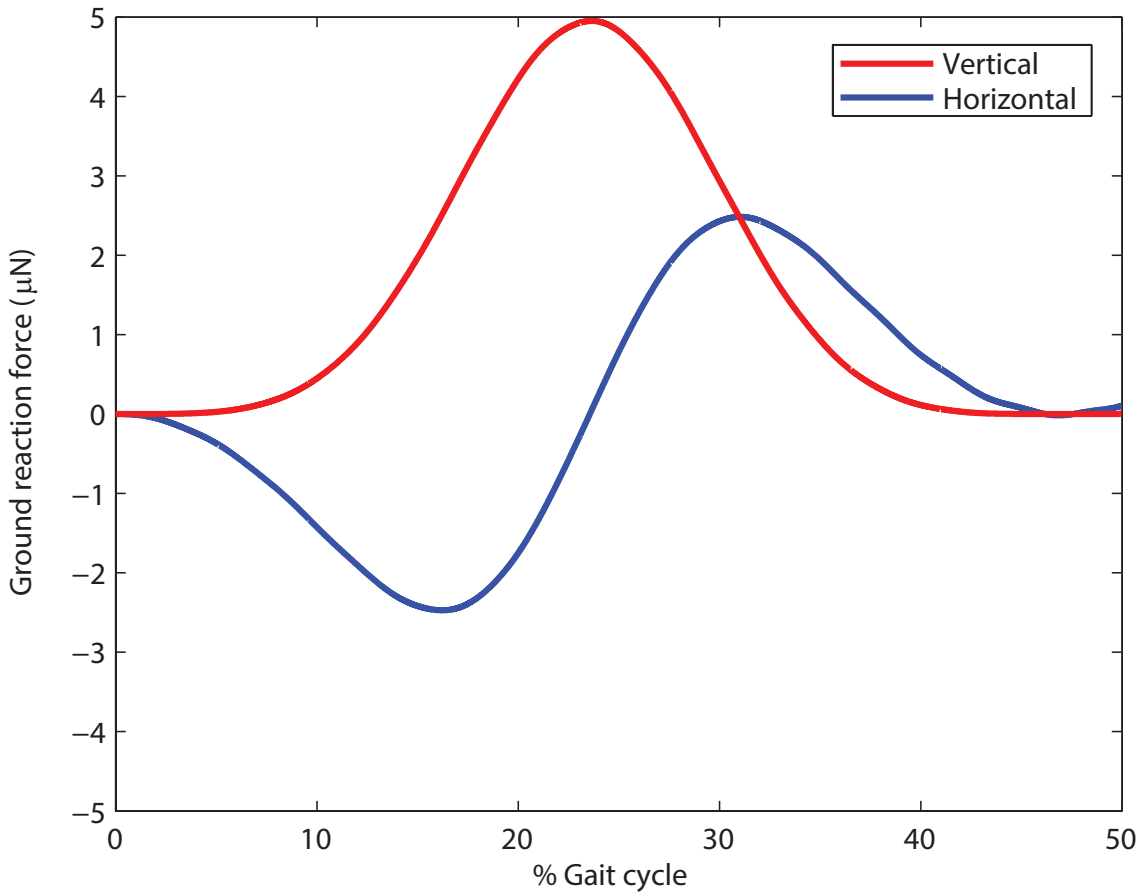

Figure 5.14: Simulated horizontal (blue) and vertical (red) ground reaction forces of a single leg a torque-driven grounded SLIP model driven at 15 Hz.

is the compression of the spring leg. Within the traditional SLIP model, the spring is compressed by both the weight of the mass and the large aerial phase. Without an aerial phase, any compression of the leg would be from either an actuated degree of freedom, which is not explored here, under the influence of gravity alone, or from momentum transfer when switching contacts. Compression from gravity will only occur when the stride frequency is less than $\frac{1}{2\pi}\sqrt{\frac{g}{l}}$, when the centripetal acceleration ($(2\pi f)^2 l$) is less than the acceleration of gravity, or under a particularly weak spring. A faster stride frequency elongates the spring.

To explore the effects of momentum transfer between stance phases for the grounded torque-driven SLIP model, the same stance equations are used, equation 5.13, with the following simplifications for switching between contact phases. The stance phase for a single leg occurs between $\pm 45°$ from the upright vertical position. Each stance phase starts at 45° and carries through to 135 °, where the contact leg is switched. Each stance phase starts with the rest length of the leg length. Contact is maintained throughout the stride, the foot does not slip against the ground. The contact is always switched, and the body does not impact the ground. The momentum is conserved as shown in

$$\begin{bmatrix} \zeta^+ \\ \dot{\zeta}^+ \\ \psi^+ \\ \dot{\psi}^+ \end{bmatrix} = \begin{bmatrix} \zeta_0 \\ \dot{\psi}^- \zeta^- \\ \psi_0 \\ \frac{\dot{\zeta}^-}{\zeta_0} \end{bmatrix} \tag{5.14}$$

where the plus and minus subscripts refer to the next stance and previous one. A schematic is shown in Figure 5.5.3.

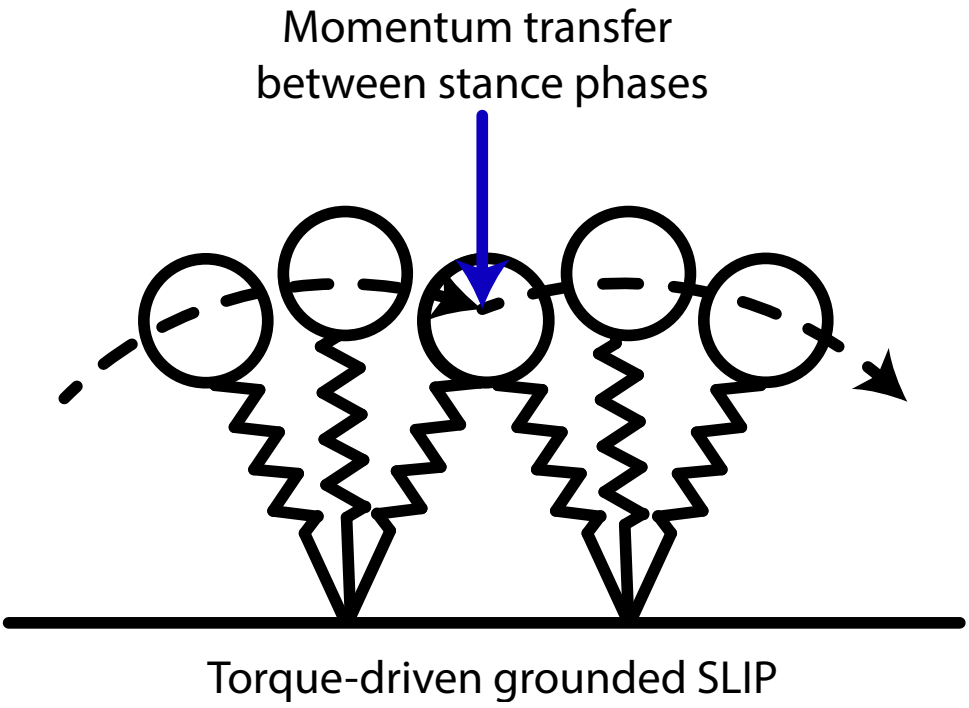

Figure 5.15: A schematic of the torque-driven grounded SLIP model showing the point of momentum transfer between stance phases.

The simulations are solved numerically using the forward Euler method with a time step of 10 µs. The same parameters as before, $m = 1\text{mg}, l = 0.71\text{mm}$, are used with a driving frequency of $\frac{1}{2\pi}\sqrt{\frac{g}{l}} \approx 18$ Hz, however, the relative spring stiffness ($k_{rel} = \frac{kl}{mg}$is changed between 3 and 100. Figure 5.16 shows the deflection of the center of mass of one stride of a the model, plotted in polar coordinates, for $k_{reL} = (3, 10, 100)$. The high stiffness, $k_{reL} = 100$, model shows very little compression or elongation of the spring leg, maintaining the length close to the natural length, while the mid-stiffness, $k_{reL} = 10$, model shows a compression of 0.1 mm, 14% of the natural length, at 60°, 16% of the stride cycle. The leg returns to the rest length at 90°, 50% of the stride cycle, and then continues to elongate, without loss of contact, from the centripetal acceleration. Since the ground contact is maintained throughout, the effect of the spring in this case is not to store elastic energy to propel a ballistic phase, but rather, serves to shorten the leg. A shortened leg decreases the time period of the inverted pendulum, $T \propto L^1$, and within the simulation, the mid-stiffness leg completes the stride 44% faster than the high-stiffness leg. The low-stiffness, $k_{reL} = 3$, shows compression at mid-stance due to the low-stiffness spring under the influence of gravity. The low-stiffness spring takes 8.5% longer to complete the stride as compared to the high-stiffness leg.

While this model, with a low relative stiffness, shows compression of the spring leg, the compression occurs at the beginning of the stride cycle. Data presented in [14] shows compression at 50% of the stride cycle. The authors' theorize that the observed compression, and corresponding acceleration propelling the second half of the cycle, are a result of an actuated, rather than passive, response by the ant. This

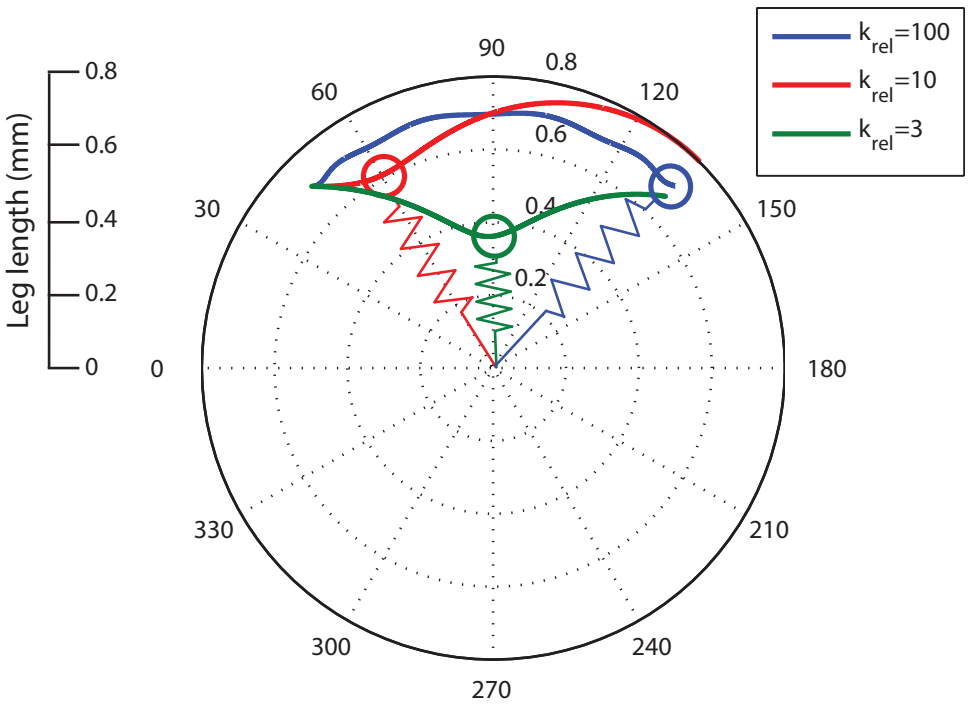

Figure 5.16: Simulated trajectories of the center of mass for $k_{rel} = 100$ (blue), $k_{rel} = 10$ (red), and $k_{rel} = 3$ (green) of a torque-driven grounded SLIP model plotted in polar coordinates.

model does support that mid-stride compression is possible passively, through an extremely low-stiffness leg, $k_{rel} = 3$, however, this is not particularly fast. Using the data available in [14], the relative stiffness for *Formica polyctena* is between 2 and 3. Figure 5.17 shows effect of relative stiffness on the non-dimensional speed, $\frac{v^2}{gl}$. High relative stiffnesses, larger than 20, show no effect on non-dimensional speed. While relative stiffnesses between 5 and 19 show a compression of the leg in the beginning of the stride cycle, with a maximum non-dimensional speed of 0.44 for a relative stiffness of 8. Interestingly, biological runners achieve maximum speeds with similar non-dimensional stiffnesses [6].

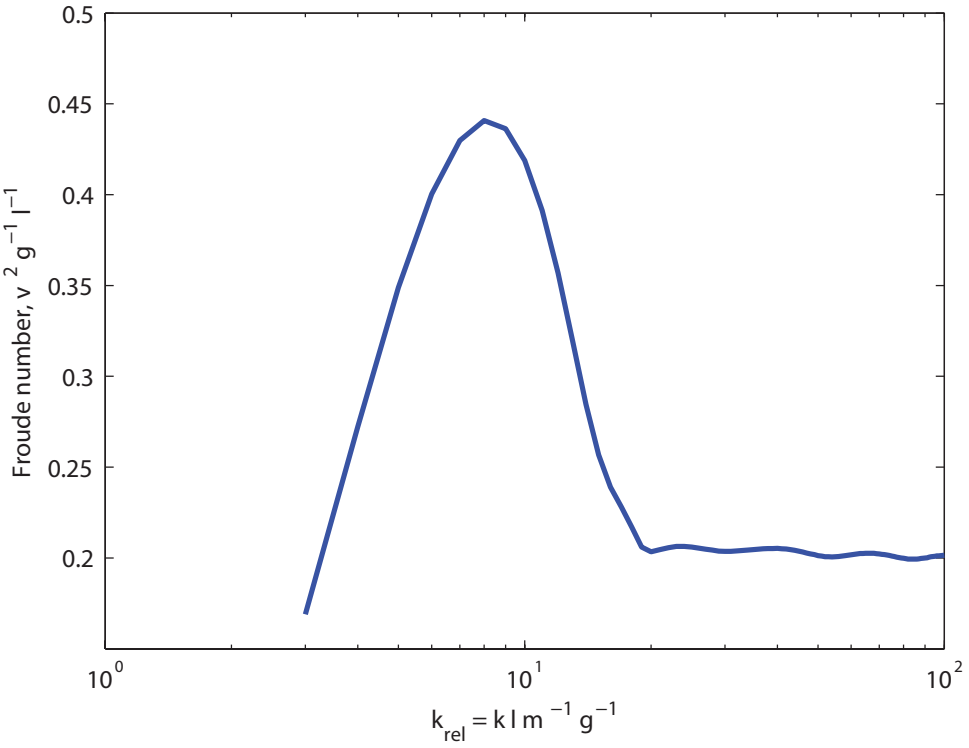

Figure 5.17: Simulated non-dimensional speed ($\frac{v^2}{gl}$) against varying relative stiffnesses $k_{rel} = \frac{kl}{mg}$.

5.6 Conclusions

This chapter presents work towards understanding the mechanics of milligram-scale running. By integrating a custom vision-based force sensor with high speed video capture, the center of mass mechanics and ground reaction forces of a legged robot, weighing 1 mg, were captured. While the kinematics of the center of mass of the robot suggested more of an inverted pendulum profile, lacking a distinct compression phase, the phasing of the kinetic and gravitational energies suggested a SLIP-like model. The captured ground reaction force suggested a SLIP-like behavior as well.

Using the information from the kinematics and ground reaction force, a torque-driven grounded SLIP model was explored. This model fit well with experimental data describing the the motion of the center of mass, as well as the phasing of the energy. However, the predicted ground reaction force phasing differed from experimentally captured data. While there are limitations to the model, such as a perfectly stuck ground contact, it is sufficient to describe the locomotion profile of this robot.

This model is expanded to consider the momentum transfer between changing stance legs in grounded running and examines the effect of compliance for milligram-scale runners. While this model makes simplifications, such as fixing the stride length through and allowing the legs to elongate without detachment, the utility of the model comes from exploring the design space for legged microrobots to enable high speed running through passive degrees of freedom. The effect of the relative stiffness suggests that in designing high-speed legged microrobots, a relative leg

stiffness around 8 would increase running speed by allowing initial compression of the leg. Of course this relies on having a perfectly stuck ground contact that immediately disengages when the contact is switched – no easy feat for microrobots.

Overall, this model explores some of the underlying dynamics in grounded running. However, additional complexities could be added to improve the understanding grounded running with imperfect contact or unreliable actuation. For example, the model could consider frictional contact, allowing slipping between the foot and the ground, and imperfect detachment, either time dependent detachment or a double stance phase. Additionally, adding these uncertainties and complexities, along with analysis techniques, gives insight into stability and the sensitivity of the design space of milligram-scale runners.

Chapter 6

Conclusions

This work brings together insights from experimental studies, modeling, and simulation for gram-scale and milligram-scale legged robots to understand the dynamics of running at various scales. A key component of this work was the experimental methodology that enables the study of locomotion at low mass without the complexities of integrating motors, controllers, and power sources at sub-gram scales. Data collected from these experiments are compared to numerical simulations to better understand how compliant leg design can simplify control requirements in future robots. This data also allows future robot designers to better understand the tradeoffs between speed, stability, and locomotion efficiency in robots at these scales. The primary contributions of this work are summarized as follows.

- An experimental method for creating 3D printed legged robots to understand the mechanical aspects of locomotion at the gram-scale.
- A dynamic stability metric to characterize experimental data of legged locomotion.
- An experimental understanding of the role of viscoelasticity in legs of gram-scale robots, ultimately creating a legged quadruped running at speeds of 11.65 body lengths per second.

- A design map exploring the effects of damping ratio and relative stiffness for gram-scale runners and an understanding of the trade-offs for various performance goals, such as speed, stability, and efficiency.
- An analogous experimental methodology creating and testing milligram scale legged robots towards understanding the mechanical aspects of locomotion.
- Characterization of monolithically printed, fully rotational, friction bearings with a characteristic length around 100 μm.
- The smallest running legged robot, running at speeds over 10 body lengths per second.
- An improved speed, demonstrating speeds for the same size robot running over 45 body lengths per second.
- The measurement of kinematics, energy, and ground reaction forces for a milligram-scale runner, giving insight to locomotion models at that scale.
- An exploration of a torque-driven grounded running model showing a utilization of passive compliance differently than a traditional SLIP-like running model.

6.1 Future work

There are many directions to take this work to further the understanding and utility of robotics with low body mass. Some possible future directions are bulleted as follows.

- Using the design maps discussed in Chapter 3 to build an autonomous robot with passively controlled dynamics through leg material choice. This can be done at any size scale, due to the nondimensionalization of the maps, and with any number of legs.

- Using either small DC motors or piezoelectric ultrasonic motors, like the actuators presented in [123] to demonstrate an autonomous gram-scale robot.

- For milligram-scale robots, ground contact through adhesion is important to locomote over a variety of terrain. Incorporating dry adhesives, such as microfabricated 'gecko skin' as in [124], on the legs of the milligram-scale robot to be able to attach and detach to and from surfaces readily to allow for vertical climbing.

- Using the experimental platforms outlined in Chapters 2 and 4, to better understand the effect of scale on the ability to cross rough terrain, defined as terrain with obstacles larger than the robot itself.

Appendix A

MATLAB code to generate rough terrain

A.1 Rough terrain generation

```
%Terrain block variation
%This is based off of the 2008 JEB paper Neuromechanical
    response of
%musculo-skeletal structures in cockroaches during rapid
    running on
%rough terrain
%All dimensions are in mm, though one can use inches

clear all; close all; clc;

HipHeight=1.5; %mm This is the hip height of the robot
RobotBodyLength=4; %mm This is the body length of the robot
SideLength=RobotBodyLength/4; %Bmm locks are scaled to 1/4
    the length
%of the robot
```

```
13 Ground=0; %This sets the ground plane, one could make a
       solid block base
14 UpperBound=3*HipHeight; %mm This sets the upper bound of the
       distribution
15 Mean=UpperBound/2; %mm
16 StandardDeviation=Mean/3; %mm
17
18 ArenaLength=200; %mm
19 ArenaWidth=100; %mm
20
21 Blocks=abs(normrnd((Mean),(StandardDeviation),...
22       [ArenaLength/SideLength ArenaWidth/SideLength]));
23 Block_vector=reshape(Blocks,numel(Blocks),1);
24
25 figure(1)
26 histfit(Block_vector,7)
27 xlabel('Block elevation (mm)')
28 ylabel('Block count')
29
30 figure(2)
31 bar3(Blocks,1)
32 axis equal
```

```
33
34 X=0:SideLength:SideLength*ArenaWidth-1;
35 Y=0:SideLength:SideLength*ArenaLength-1;
36 loop=1;
37
38 vertices_cell=cell(numel(Blocks),1);
39 faces_cell=cell(numel(Blocks),1);
40
41 for index1=1:length(X);
42     for index2=1:length(Y);
43         x_corner=X(index1);
44         y_corner=Y(index2);
45         height=Blocks(index2,index1);
46         vertices_cell{loop,1}=cube_vertices(x_corner,
               y_corner,SideLength,height,Ground);
47         faces_cell{loop,1}=cube_faces(loop);
48         loop=loop+1;
49     end
50 end
51
52 fv.vertices=cell2mat(vertices_cell);
53 fv.faces=cell2mat(faces_cell);
```

```
54
55 %% Render
56 % The model is rendered with a PATCH graphics object. We
       also add some dynamic
57 % lighting, and adjust the material properties to change the
       specular
58 % highlighting.
59 figure(3)
60 patch(fv,'FaceColor',       [0.8 0.8 1.0], ...
61           'EdgeColor',       'none',        ...
62           'FaceLighting',    'gouraud',     ...
63           'AmbientStrength', 0.15);
64
65 % Add a camera light, and tone down the specular
       highlighting
66 camlight('headlight');
67 material('dull');
68
69 % Fix the axes scaling, and set a nice view angle
70 axis('image');
71 view([-30 30]);
72 xlabel('Width (mm)')
```

```
73 ylabel('Length (mm)')
74 zlabel('Elevation (mm)')
75
76 %% Write file
77 stlwrite('microhex_terrain.stl',fv);
```

Appendix B

MATLAB code for torque-driven grounded running

B.1 Forward Euler simulation for the torque-driven grounded SLIP model

```
clear all; close all;

m=1e-6; %kg
g=9.81; %m/s^2
l0=5.64e-3/8; %m

krel=10;

k=krel*m*g/l0; %N/m
b=2*0.0925*0; %N-s/m
cc=2*sqrt(k*m);

freq=1/(2*pi)*sqrt(g/l0);

zeta0=l0;
```

```
16 tau_max=1.381e-8; %N-m
17
18 dt=.01e-3;
19 t=[0:dt:2*1/freq]';
20 int(1,:)=[zeta0 0 pi/4 0];
21
22 i=1;
23
24 while loopindex<10
25
26 inttemp=int(loopindex,:);
27
28 [zeta, dzeta, psi, dpsi, i, torque] = polarmodel2(t, g, freq
       , dt, tau_max, k, b, m, zeta0, inttemp);
29 zetac{loopindex,1}=zeta;
30 dzetac{loopindex,1}=dzeta;
31 psic{loopindex,1}=psi;
32 dpsic{loopindex,1}=dpsi;
33 torquec{loopindex,1}=torque;
34 timeindexvec(loopindex,1)=i;
35
36 loopindex=loopindex+1;
```

```
37
38 int(loopindex,:)=[zeta0 -1*zeta(end)*dpsi(end)*dt pi/4 -1*dt
       *dzeta(end)/zeta0];
39
40
41 end
42
43
44
45 %%%%%%%
46 function [zeta, dzeta, psi, dpsi, i, torque] = polarmodel2(t
       , g, freq, dt, tau_max, k, b, m, zeta0, int)
47 istart=1;
48 zeta(istart,1)=int(1);
49 dzeta(istart,1)=int(2);
50 psi(istart,1)=int(3);
51 dpsi(istart,1)=int(4);
52
53 for i = 1:length(t)
54     psi_des(i,1)=(i-1)*2*pi*freq*dt+pi/4;
55     torque(i,1)=tau_max*sin(psi_des(i,1)-psi(i,1));
```

```
56      ddzeta(i,1)=zeta(i,1)*dpsi(i,1)^2-g*sin(psi(i,1))-k/m*(
            zeta(i,1)-zeta0)-b/m*dzeta(i,1);
57      dzeta(i+1,1)=dzeta(i,1)+dt*ddzeta(i,1);
58      zeta(i+1,1)=zeta(i,1)+dt*dzeta(i,1);
59      ddpsi(i,1)=2*dzeta(i,1)*dpsi(i,1)/zeta(i,1)+g*cos(psi(i
            ,1))/zeta(i,1)+torque(i,1)/(m*zeta(i,1));
60      dpsi(i+1,1)=dpsi(i,1)+dt*ddpsi(i,1);
61      psi(i+1,1)=psi(i,1)+dt*dpsi(i,1);
62
63
64      ddy(i,1)=zeta(i,1)*-1*sin(psi(i,1))*dpsi(i,1)^2+ddzeta(i
            ,1)*sin(psi(i,1))+2*(dzeta(i,1)*cos(psi(i,1))*dpsi(i
            ,1));
65
66
67
68       if  psi(i,1)>0.75*pi;
69           return
70       end
71      %if leg is too compliant, bottoms out at ground.
72       if  zeta(i,1)<0
73           zeta(i,1)=0;
```

```
74              dzeta(i,1)=0;
75          end
76
77  end
78  end
```

Bibliography

[1] Robert J Full and Michael S Tu. Mechanics of six-legged runners. *Journal of Experimental Biology*, 148(1):129–146, 1990.

[2] Robert J Full and Michael S Tu. Mechanics of a rapid running insect: two-, four-and six-legged locomotion. *Journal of Experimental Biology*, 156(1):215–231, 1991.

[3] Robert J Full, Reinhard Blickhan, and Lena H Ting. Leg design in hexapedal runners. *Journal of Experimental Biology*, 158(1):369–390, 1991.

[4] Robert J Full, Darrell R Stokes, Anna N Ahn, and Robert K Josephson. Energy absorption during running by leg muscles in a cockroach. *Journal of Experimental Biology*, 201(7):997–1012, 1998.

[5] Simon Sponberg and Robert J Full. Neuromechanical response of musculoskeletal structures in cockroaches during rapid running on rough terrain. *Journal of Experimental Biology*, 211(3):433–446, February 2008.

[6] Reinhard Blickhan and Robert J Full. Similarity in multilegged locomotion: bouncing like a monopode. *Journal of Comparative Physiology A*, 173(5):509–517, 1993.

[7] Samuel Rubin, Maria Ho-Yan Young, Jonathan C Wright, Dwight L Whitaker, and Anna N Ahn. Exceptional running and turning performance in a mite. *Journal of Experimental Biology*, 219(5):676–685, 2016.

[8] Norman C Heglund, C Richard Taylor, and Thomas A McMahon. Scaling stride frequency and gait to animal size: mice to horses. *Science*, 186(4169):1112–1113, 1974.

[9] Robert J Full. Invertebrate locomotor systems. *Comprehensive Physiology*, 1997.

[10] Andrew A Biewener. *Animal locomotion*. Oxford University Press, 2003.

[11] Michael Kaspari and Michael D Weiser. The size–grain hypothesis and interspecific scaling in ants. *Functional Ecology*, 13(4):530–538, 1999.

[12] Martin Pfeiffer and K Eduard Linsenmair. Polydomy and the organization of foraging in a colony of the malaysian giant ant camponotus gigas (hym./form.). *Oecologia*, 117(4):579–590, 1998.

[13] Lars Reinhardt, Tom Weihmann, and Reinhard Blickhan. Dynamics and kinematics of ant locomotion: do wood ants climb on level surfaces? *Journal of Experimental Biology*, 212(15):2426–2435, 2009.

[14] Lars Reinhardt and Reinhard Blickhan. Level locomotion in wood ants: evidence for grounded running. *Journal of Experimental Biology*, 217(13):2358–2370, 2014.

[15] Toni Wöhrl, Lars Reinhardt, and Reinhard Blickhan. Propulsion in hexapod locomotion: how do desert ants traverse slopes? *Journal of Experimental Biology*, 220(9):1618–1625, 2017.

[16] Benjamin Goldberg, Neel Doshi, Kaushik Jayaram, and Robert J Wood. Gait studies for a quadrupedal microrobot reveal contrasting running templates in two frequency regimes. *Bioinspiration & Biomimetics*, 12(4):046005, 2017.

[17] Giovanni A Cavagna, H Thys, and A Zamboni. The sources of external work in level walking and running. *The Journal of Physiology*, 262(3):639–657, 1976.

[18] Torkel Weis-Fogh. A rubber-like protein in insect cuticle. *Journal of Experimental Biology*, 37(4):889–907, 1960.

[19] Uluc Saranli and Daniel E Koditschek. Template based control of hexapedal running. In *Proceedings of the International Conference on Robotics and Automation*, volume 1, pages 1374–1379. IEEE, 2003.

[20] Ioannis Poulakakis and Jessy W Grizzle. Formal embedding of the spring loaded inverted pendulum in an asymmetric hopper. In *Proceedings of the European Control Conference*, pages 3159–3166. IEEE, 2007.

[21] ZhuoHua Shen and Justin Seipel. Animals prefer leg stiffness values that may reduce the energetic cost of locomotion. *Journal of Theoretical Biology*, 364:433–438, 2015.

[22] ZhuoHua Shen and Justin Seipel. The leg stiffnesses animals use may improve the stability of locomotion. *Journal of Theoretical Biology*, 377:66–74, 2015.

[23] Paul Birkmeyer, Kevin Peterson, and Ronald S Fearing. Dash: A dynamic 16g hexapedal robot. In *Proceedings of the International Conference on Intelligent Robots and Systems*, pages 2683–2689. IEEE, 2009.

[24] Uluc Saranli, Martin Buehler, and Daniel E Koditschek. Rhex: A simple and highly mobile hexapod robot. *International Journal of Robotics Research*, 20(7):616–631, 2001.

[25] Joel D Weingarten, Martin Buehler, Richard E Groff, and Daniel E Koditschek. Gait generation and optimization for legged robots. In *Proceedings of the International Conference on Robotics and Automation*, 2003.

[26] G. Clark Haynes and Alfred Rizzi. Gaits and gait transitions for legged robots. In *Proceedings of the International Conference on Robotics and Automation*, pages 1117–1122. IEEE, 2006.

[27] Aaron M Hoover, Erik Steltz, and Ronald S Fearing. RoACH: An autonomous 2.4 g crawling hexapod robot. In *Proceedings of the International Conference on Intelligent Robots and Systems*, pages 26–33. IEEE, 2008.

[28] Katie L Hoffman and Robert J Wood. Passive undulatory gaits enhance walking in a myriapod millirobot. In *Proceedings of the International Conference on Intelligent Robots and Systems*, pages 1479–1486. IEEE, 2011.

[29] Andrew T Baisch, Onur Ozcan, Benjamin Goldberg, Daniel Ithier, and Robert J Wood. High speed locomotion for a quadrupedal microrobot. *The International Journal of Robotics Research*, pages 1063–1082, 2014.

[30] Neel Doshi, Kaushik Jayaram, Benjamin Goldberg, and Robert J Wood. Phase control for a legged microrobot operating at resonance. In *Proceedings of the International Conference on Robotics and Automation*, pages 5969–5975. IEEE, 2017.

[31] Benjamin Goldberg, Neel Doshi, and Robert J Wood. High speed trajectory control using an experimental maneuverability model for an insect-scale legged robot. In *Proceedings of the International Conference on Robotics and Automation*, pages 3538–3545. IEEE, 2017.

[32] Andrew T Baisch, Christian Heimlich, Michael Karpelson, and Robert J Wood. HAMR3: An autonomous 1.7 g ambulatory robot. In *Proceedings of the International Conference on Intelligent Robots and Systems*, pages 5073–5079. IEEE, 2011.

[33] Michael Karpelson, Benjamin H Waters, Benjamin Goldberg, Brody Mahoney, Onur Ozcan, Andrew Baisch, Pierre-Marie Meyitang, Joshua R Smith, and Robert J Wood. A wirelessly powered, biologically inspired ambulatory microrobot. In *Proceedings of the International Conference on Robotics and Automation*, pages 2384–2391. IEEE, 2014.

[34] Benjamin Goldberg, Raphael Zufferey, Neel Doshi, Elizabeth Farrell Helbling, Griffin Whittredge, Mirko Kovac, and Robert J Wood. Power and control autonomy for high-speed locomotion with an insect-scale legged robot. *Robotics and Automation Letters*, 3(2):987–993, 2018.

[35] Paul E Kladitis and Victor M Bright. Prototype microrobots for micropositioning and micro-unmanned vehicles. *Sensors and Actuators A: Physical*, 80(2):132–137, 2000.

[36] E Yegan Erdem, Yu-Ming Chen, Matthew Mohebbi, John W Suh, Gregory TA Kovacs, Robert B Darling, and Karl F Bohringer. Thermally actuated omnidirectional walking microrobot. *Journal of Microelectromechanical Systems*, 19(3):433–442, 2010.

[37] Takashi Yasuda, Isao Shimoyama, and Hirofumi Miura. Microrobot locomotion in a mechanical vibration field. *Advanced Robotics*, 9(2):165–176, 1994.

[38] Seth Hollar, Anita Flynn, Colby Bellew, and KSJ Pister. Solar powered 10 mg silicon robot. In *International Conference on Micro Electro Mechanical Systems*, pages 706–711. IEEE, 2003.

[39] Daniel S Contreras, Daniel S Drew, and Kristofer SJ Pister. First steps of a millimeter-scale walking silicon robot. In *Proceedings of the International Conference on Solid State Sensors and Actuators*, pages 910–913. IEEE, 2017.

[40] Daisuke Tanaka, Yuto Uchiumi, Satoshi Kawamura, Minami Takato, Ken Saito, and Fumio Uchikoba. Four-leg independent mechanism for mems microrobot. *Artificial Life and Robotics*, 22(3):380–384, 2017.

[41] Kazuki Sugita, Daisuke Tanaka, Satoko Ono, Satohoro Chiba, Kei Iwata, Yuxuan Han, Minami Takato, Fumio Uchikoba, and Ken Saito. Sma actuator and pulse-type hardware neural networks ic for fast walking motion of insect-type mems microrobot. In *Proceedings of the International Conference on Advanced Intelligent Mechatronics*, pages 431–435. IEEE, 2016.

[42] Jinhong Qu, Clark B Teeple, and Kenn Oldham. Modeling legged micro-robot locomotion based on contact dynamics and vibration in multiple modes and axes. *Journal of Vibration and Acoustics*, 2017.

[43] Jeong Hoon Ryou and Kenn Richard Oldham. Dynamic characterization of contact interactions of micro-robotic leg structures. *Smart Materials and Structures*, 23(5):055014, 2014.

[44] Dana Vogtmann, Ryan St. Pierre, and Sarah Bergbreiter. A 25 mg magnetically actuated microrobot walking at¿ 5 body lengths/sec. In *Proceedings of the International Conference on Micro Electro Mechanical Systems*, pages 179–182. IEEE, 2017.

[45] Thorbjörn Ebefors, Johan Ulfstedt Mattsson, Edvard Kälvesten, and Göran Stemme. A walking silicon micro-robot. In *Proceedings of the International Conference on Solid State Sensors and Actuators*, pages 1202–1205. Citeseer, 1999.

[46] Sang-bae Kim, Jonathan E Clark, and Mark R Cutkosky. iSprawl: Design and Tuning for High-speed Autonomous Open-loop Running. *The International Journal of Robotics Research*, 25(9):903–912, September 2006.

[47] Alexandra Lipp, Harald Wolf, and Fritz-Olaf Lehmann. Walking on inclines: energetics of locomotion in the ant camponotus. *Journal of Experimental Biology*, 208(4):707–719, 2005.

[48] John RB Lighton, George A Bartholomew, and Donald H Feener. Energetics of locomotion and load carriage and a model of the energy cost of foraging in the leaf-cutting ant atta colombica guer. *Physiological Zoology*, 60(5):524–537, 1987.

[49] John AG Breen. *Studies on Formica lugubris Zetterstedt in Ireland (Hymenoptera, Formicidae)*. PhD thesis, University College Cork, 1976.

[50] SJ Holt. On the foraging activity of the wood ant. *The Journal of Animal Ecology*, pages 1–34, 1955.

[51] Gerrit Jan De Bruyn and Martje Kruk-de Bruin. *The diurnal rhythm in a population of Formica polyctena Foerst*. Państwowe Wydawnictwo Naukowe, 1972.

[52] Robert J. Full and Michael S. Tu. Mechanics of six-legged runners. *Journal of Experimental Biology*, 148(1):129–146, 1990.

[53] Ryan St. Pierre and Sarah Bergbreiter. Gait Exploration of Sub-2 g Robots Using Magnetic Actuation. *IEEE Robotics and Automation Letters*, 2(1):34–40, January 2017.

[54] Dominic R Frutiger, Karl Vollmers, Bradley E Kratochvil, and Bradley J Nelson. Small, fast, and under control: wireless resonant magnetic micro-agents. *The International Journal of Robotics Research*, 29(5):613–636, 2010.

[55] Kyle Gilpin and Daniela Rus. Self-disassembling robot pebbles: New results and ideas for self-assembly of 3d structures. In *Proceedings of the International Conference on Robotics and Automation Workshop on Modular Robots: State of the Art*, pages 94–99, 2010.

[56] Masahiko Sendoh, Kazushi Ishiyama, and Ken Ichi Arai. Fabrication of magnetic actuator for use in a capsule endoscope. *IEEE Transactions on Magnetics*, 39(5):3232–3234, 2003.

[57] K Berk Yesin, Philipp Exner, Karl Vollmers, and Bradley J Nelson. Design and control of in-vivo magnetic microrobots. In *Medical Image Computing and Computer-Assisted Intervention*, pages 819–826. Springer, 2005.

[58] Wuming Jing, Nicholas Pagano, and David J Cappelleri. A novel micro-scale magnetic tumbling microrobot. *Journal of Micro-Bio Robotics*, 8(1):1–12, February 2013.

[59] Steven Floyd, Chytra Pawashe, and Metin Sitti. An untethered magnetically actuated micro-robot capable of motion on arbitrary surfaces. In *Proceedings of the International Conference on Robotics and Automation*, pages 419–424. IEEE, 2008.

[60] Tianshuo Zhang, Albert Kim, Manuel Ochoa, and Babak Ziaie. Controllable 'somersault magnetic soft robotics. In *Proceedings of the International Conference on Micro Electro Mechanical Systems*, pages 1044–1047. IEEE, 2015.

[61] Shuhei Miyashita, Steven Guitron, Marvin Ludersdorfer, C. Sung, and Daniela Rus. An Untethered Miniature Origami Robot that Self-folds, Walks, Swims, and Degrades. In *Proceedings of the International Conference on Robotics and Automation*, Seattle, WA USA, May 2015.

[62] Ryan St. Pierre, Dana Vogtmann, and Sarah Bergbreiter. Model-based insights on the design of a hexapod magnetic walker. In *Proceedings of the International Symposium on Experimental Robotics*, Marrakech, Morocco, June 2014.

[63] Arthur W Mahoney and Jake J Abbott. Generating Rotating Magnetic Fields With a Single Permanent Magnet for Propulsion of Untethered Magnetic Devices in a Lumen. *IEEE Transactions on Robotics*, 30(2):411–420, April 2014.

[64] Samuel E Wright, Arthur W Mahoney, Katie M Popek, and Jake J Abbott. A spherical-magnet end-effector for robotic magnetic manipulation. In *Proceedings of the International Conference on Robotics and Automation*, pages 1190–1195. IEEE, 2015.

[65] Reinhard Blickhan, Andre Seyfarth, Hartmut Geyer, Sten Grimmer, Heiko Wagner, and Michael Günther. Intelligence by mechanics. *Philosophical Transactions of the Royal Society of London A: Mathematical, Physical and Engineering Sciences*, 365(1850):199–220, 2007.

[66] Thomas L Daniel. Invertebrate swimming: integrating internal and external mechanics. In *Symposia of the Society for Experimental Biology*, volume 49, pages 61–89, 1994.

[67] M Tu and M Dickinson. Modulation of negative work output from a steering muscle of the blowfly calliphora vicina. *Journal of Experimental Biology*, 192(1):207–224, 1994.

[68] Monica A Daley and Andrew A Biewener. Running over rough terrain reveals limb control for intrinsic stability. *Proceedings of the National Academy of Sciences*, 103(42):15681–15686, 2006.

[69] Anna N Ahn and Robert J Full. A motor and a brake: two leg extensor muscles acting at the same joint manage energy differently in a running insect. *Journal of Experimental Biology*, 205(3):379–389, 2002.

[70] Devin L Jindrich and Robert J Full. Dynamic stabilization of rapid hexapedal locomotion. *Journal of Experimental Biology*, 205(18):2803–2823, 2002.

[71] Daniel M Dudek and Robert J Full. Passive mechanical properties of legs from running insects. *The Journal of Experimental Biology*, 209(8):1502–1515, 2006.

[72] John A Rieffel, Francisco J Valero-Cuevas, and Hod Lipson. Morphological communication: exploiting coupled dynamics in a complex mechanical structure to achieve locomotion. *Journal of the Royal Society Interface*, 7(45):613–621, 2010.

[73] Jae Yun Jun and Jonathan E Clark. Dynamic stability of variable stiffness running. In *Proceedings of the International Conference on Robotics and Automation*, pages 1756–1761. IEEE, 2009.

[74] Kevin C Galloway, Jonathan E Clark, Mark Yim, and Daniel E Koditschek. Experimental investigations into the role of passive variable compliant legs for dynamic robotic locomotion. In *Proceedings of the International Conference on Robotics and Automation*, pages 1243–1249. IEEE, 2011.

[75] Stephen A Wainwright. *Mechanical design in organisms*. Princeton University Press, 1982.

[76] Ian M Ward and John Sweeney. *Mechanical properties of solid polymers*. John Wiley & Sons, 2012.

[77] Francis C Moon. *Chaotic and fractal dynamics: introduction for applied scientists and engineers*. John Wiley & Sons, 2008.

[78] Daniel B Marghitu, Steven A Kincaid, and Paul F Rumph. Nonlinear dynamics stability measurements of locomotion in healthy greyhounds. *American Journal of Veterinary Research*, 57(11):1529–1535, 1996.

[79] Bruce D Miller, Jason M Brown, and Jonathan E Clark. On prismatic and torsional actuation for running legged robots. In *Proceedings of the International Symposium on Experimental Robotics*, pages 17–31. Springer, 2016.

[80] Ben Andrews, Bruce Miller, John Schmitt, and Jonathan E Clark. Running over unknown rough terrain with a one-legged planar robot. *Bioinspiration & Biomimetics*, 6(2):026009, 2011.

[81] Robert McNeill Alexander. The gaits of bipedal and quadrupedal animals. *The International Journal of Robotics Research*, 3(2):49–59, 1984.

[82] Philip Holmes, Robert J Full, Dan Koditschek, and John Guckenheimer. The dynamics of legged locomotion: Models, analyses, and challenges. *Society for the Industrial and Applied Mathematics Review*, 48(2):207–304, 2006.

[83] Thomas Lamb et al. *Ship design and construction*, volume 4. Society of Naval Architects and Marine Engineers, 2003.

[84] Thor I Fossen. *Handbook of marine craft hydrodynamics and motion control*. John Wiley & Sons, 2011.

[85] Jennifer H Fewell, Jon F Harrison, John RB Lighton, and Michael D Breed. Foraging energetics of the ant, paraponera clavata. *Oecologia*, 105(4):419–427, 1996.

[86] Christopher N LaFratta, John T Fourkas, Tommaso Baldacchini, and Richard A Farrer. Multiphoton fabrication. *Angewandte Chemie International Edition*, 46(33):6238–6258, 2007.

[87] K & J Magnetics. K & J Magnetics - Specifications, howpublished = "https://www.kjmagnetics.com/specs.asp", year=2018, urldate=2018-01-22, note = Online: Accessed: 2018-01-22.

[88] Nima Ghalichechian, Alireza Modafe, Mustafa Ilker Beyaz, and Reza Ghodssi. Design, fabrication, and characterization of a rotary micromotor supported on microball bearings. *Journal of Microelectromechanical Systems*, 17(3):632–642, 2008.

[89] Luc G Fréchette, Stuart A Jacobson, Kenneth S Breuer, Fredric F Ehrich, Reza Ghodssi, Ravi Khanna, Chee Wei Wong, Xin Zhang, Martin A Schmidt, and Alan H Epstein. High-speed microfabricated silicon turbomachinery and fluid film bearings. *Journal of Microelectromechanical Systems*, 14(1):141–152, 2005.

[90] Suresh Kumar, Dan Cho, and William N Carr. Experimental study of electric suspension for microbearings. *Journal of Microelectromechanical Systems*, 1(1):23–30, 1992.

[91] X-S Wu, W-Y Chen, X-L Zhao, and W-P Zhang. Micromotor with electromagnetically levitated rotor using separated coils. *Electronics Letters*, 40(16):996–997, 2004.

[92] A Takei, N Binh-Khiem, E Iwase, K Matsumoto, and I Shimoyama. Liquid motor driven by electrowetting. In *Proceedings of the International Conference on Micro Electro Mechanical Systems*, pages 42–45. IEEE, 2008.

[93] Amane Kajiwara, Kenji Suzuki, Hirofumi Miura, and Hideaki Takanobu. Study on micromotor using surface tension of liquid droplets. *Research Reports of Kogakuin University*, pages 25–30, 2006.

[94] Mei Lin Chan, Brian Yoxall, Hyunkyu Park, Zhaoyi Kang, Igor Izyumin, Jeffrey Chou, Mischa M Megens, Ming C Wu, Bernhard E Boser, and David A Horsley. Design and characterization of mems micromotor supported on low friction liquid bearing. *Sensors and Actuators A: Physical*, 177:1–9, 2012.

[95] Robert J Full and Daniel E Koditschek. Templates and anchors: neuromechanical hypotheses of legged locomotion on land. *Journal of Experimental Biology*, 202(23):3325–3332, 1999.

[96] Giovanni A Cavagna, Norman C Heglund, and C Richard Taylor. Mechanical work in terrestrial locomotion: two basic mechanisms for minimizing energy expenditure. *American Journal of Physiology-Regulatory, Integrative and Comparative Physiology*, 233(5):R243–R261, 1977.

[97] Matthias Wittlinger, Rüdiger Wehner, and Harald Wolf. The desert ant odometer: a stride integrator that accounts for stride length and walking speed. *Journal of Experimental Biology*, 210(2):198–207, 2007.

[98] Mariano Garcia, Arthur Kuo, Anne M Peattie, Paul C Wang, and Robert J Full. Damping and size: Insights and biological inspiration. In *Proc. of the Intl. Symp. on Adaptive Motion of Animals and Machines, Montreal, Canada*, 2000.

[99] Isaac W Moran, Dalton F Cheng, Sarav B Jhaveri, and Kenneth R Carter. High-resolution soft lithography of thin film resists enabling nanoscopic pattern transfer. *Soft Matter*, 4(1):168–176, 2008.

[100] Margot Billot, Xin Xu, Joël Agnus, Emmanuel Piat, and Philippe Stempflé. Multi-axis mems force sensor for measuring friction components involved in dexterous micromanipulation: design and optimisation. *International Journal of Nanomanufacturing*, 11(3-4):161–184, 2015.

[101] P Estevez, JM Bank, M Porta, J Wei, PM Sarro, M Tichem, and U Staufer. 6 dof force and torque sensor for micro-manipulation applications. *Sensors and Actuators A: Physical*, 186:86–93, 2012.

[102] Bilal Komati, Joël Agnus, Cédric Clévy, and Philippe Lutz. Prototyping of a highly performant and integrated piezoresistive force sensor for microscale applications. *Journal of Micromechanics and Microengineering*, 24(3):035018, 2014.

[103] Joël Abadie, Emmanuel Piat, Stéphane Oster, and Mehdi Boukallel. Modeling and experimentation of a passive low frequency nanoforce sensor based on diamagnetic levitation. *Sensors and Actuators A: Physical*, 173(1):227–237, 2012.

[104] M Dienwiebel, E De Kuyper, L Crama, JWM Frenken, JA Heimberg, D-J Spaanderman, D Glastra Van Loon, T Zijlstra, and E van der Drift. Design and performance of a high-resolution frictional force microscope with quantitative three-dimensional force sensitivity. *Review of Scientific Instruments*, 76(4):043704, 2005.

[105] XJ Zhang, S Zappe, RW Bernstein, O Sahin, C-C Chen, M Fish, MP Scott, and O Solgaard. Micromachined silicon force sensor based on diffractive optical encoders for characterization of microinjection. *Sensors and Actuators A: Physical*, 114(2-3):197–203, 2004.

[106] Yu Sun, Steven N Fry, DP Potasek, Dominik J Bell, and Brad J Nelson. Characterizing fruit fly flight behavior using a microforce sensor with a new comb-drive configuration. *Journal of Microelectromechanical Systems*, 14(1):4–11, 2005.

[107] Felix Beyeler, Simon Muntwyler, and Bradley J Nelson. A six-axis mems force–torque sensor with micro-newton and nano-newtonmeter resolution. *Journal of Microelectromechanical Systems*, 18(2):433–441, 2009.

[108] Robert J Wood, Kyujin J Cho, and Katie Hoffman. A novel multi-axis force sensor for microrobotics applications. *Smart materials and structures*, 18(12):125002, 2009.

[109] Peter J Berkelman, Louis L Whitcomb, Russell H Taylor, and Patrick Jensen. A miniature microsurgical instrument tip force sensor for enhanced force feedback during robot-assisted manipulation. *IEEE Transactions on Robotics and Automation*, 19(5):917–921, 2003.

[110] Kai Kristiansen, Patricia McGuiggan, Greg Carver, Carl Meinhart, and Jacob Israelachvili. 3d force and displacement sensor for sfa and afm measurements. *Langmuir*, 24(4):1541–1549, 2008.

[111] Lars Reinhardt and Reinhard Blickhan. Ultra-miniature force plate for measuring triaxial forces in the micronewton range. *Journal of Experimental Biology*, 217(5):704–710, 2014.

[112] Ren-Jung Chang, Chih-Cheng Shiu, and Chih-Yi Cheng. Self-biased-sma drive pu microgripper with force sensing in visual servo. *International Journal of Advanced Robotic Systems*, 10(6):280, 2013.

[113] David J Cappelleri, Gianluca Piazza, and Vijay Kumar. A two dimensional vision-based force sensor for microrobotic applications. *Sensors and Actuators A: Physical*, 171(2):340–351, 2011.

[114] Valérian Guelpa, Jean-Sébastien Prax, Youen Vitry, Olivier Lehmann, Sam Dehaeck, Patrick Sandoz, Cédric Clévy, Nadine Le Fort-Piat, Pierre Lambert, and Guillaume J Laurent. 3d-printed vision-based micro-force sensor dedicated to in situ sem measurements. In *Proceedings of the International Conference on Advanced Intelligent Mechatronics*, pages 424–429. IEEE, 2017.

[115] David J Cappelleri, Girish Krishnan, Charles Kim, Vijay Kumar, and Sridhar Kota. Toward the design of a decoupled, two-dimensional, vision-based μn force sensor. *Journal of Mechanisms and Robotics*, 2(2):021010, 2010.

[116] Girish Krishnan, Charles Kim, and Sridhar Kota. An intrinsic geometric framework for the building block synthesis of single point compliant mechanisms. *Journal of Mechanisms and Robotics*, 3(1):011001, 2011.

[117] Namik Ciblak and Harvey Lipkin. Remote center of compliance reconsidered. In *Proceedings of the ASME International Design Engineering Technical Conferences & Computers and Information in Engineering Conference*. Citeseer, 1996.

[118] Jeffrey L Hutter and John Bechhoefer. Calibration of atomic-force microscope tips. *Review of Scientific Instruments*, 64(7):1868–1873, 1993.

[119] Christophe P E Zollikofer. Stepping patterns in ants-influence of body morphology. *Journal of experimental biology*, 192(1):107–118, 1994.

[120] Anna N Ahn, E Furrow, and Andrew A Biewener. Walking and running in the red-legged running frog, kassina maculata. *Journal of Experimental Biology*, 207(3):399–410, 2004.

[121] Michael K Cheezum, William F Walker, and William H Guilford. Quantitative comparison of algorithms for tracking single fluorescent particles. *Biophysical Journal*, 81(4):2378–2388, 2001.

[122] Ivo F Sbalzarini and Petros Koumoutsakos. Feature point tracking and trajectory analysis for video imaging in cell biology. *Journal of Structural Biology*, 151(2):182–195, 2005.

[123] Prakruthi Hareesh and Don L DeVoe. Annular ultrasonic micromotors fabricated from bulk pzt. In *Proceedings of the International Conference on Micro Electro Mechanical Systems*, pages 765–768. IEEE, 2017.

[124] Aaron Parness, Daniel Soto, Noé Esparza, Nick Gravish, Matt Wilkinson, Kellar Autumn, and Mark Cutkosky. A microfabricated wedge-shaped adhesive array displaying gecko-like dynamic adhesion, directionality and long lifetime. *Journal of the Royal Society Interface*, pages rsif–2009, 2009.